

Brain Plasticity, Extracellular Matrix
Molecules, and Advancements in Calcium
Imaging of Neural Activity

Sverre Grødem

© Sverre Grødem, 2023

*Series of dissertations submitted to the
Faculty of Mathematics and Natural Sciences, University of Oslo
No. 2654*

ISSN 1501-7710

All rights reserved. No part of this publication may be
reproduced or transmitted, in any form or by any means, without permission.

Cover: UiO.

Print production: Graphic center, University of Oslo.

Abstract

The brain possesses an astounding ability to acquire new memories and retain these memories throughout our lifespan. Consequently, neuronal networks in the brain must exhibit flexibility, or plasticity, adapting and strengthening neuronal connections in response to new learning. Simultaneously, the brain must maintain sufficient stability to solidify the neural connections that underpin long-term memory. The lattice-like structures known as Perineuronal Nets (PNNs), which mainly surround Parvalbumin-expressing (PV+) interneurons in the cerebral cortex, are believed to dampen brain plasticity, thus facilitating long-term information retention. In this thesis, I apply the most precise perturbation technique for PNNs yet - knocking out aggrecan, a crucial component of PNNs, solely in PV+ neurons. Through electrophysiological and behavioral assays, as well as computational modeling, I investigate potential effects. My findings indicate that transgenic knockout of aggrecan eliminates PNNs reactive to the PNN marker Wisteria Floribunda Lectin (WFA), without affecting PV neuron function or plasticity in the visual cortex. In contrast, the knockout of aggrecan in adults profoundly affects plasticity, suggesting that compensatory mechanisms may mitigate the effect of losing aggrecan in the germline. Finally, I develop soma-targeted, genetically-encoded calcium indicator constructs that exceed the performance of all prior published constructs, enhancing the capability of *in-vivo* neuronal activity measurement.

Sammendrag

Hjernen har ein forbløffande evne til å tileigne seg nye minner og behalde desse minna gjennom heile livet. Følgjeleg må nevronnettverk i hjernen vise fleksibilitet, eller plastisitet; nevronale koblingar må tilpassas i respons til ny læring. Samstundes må hjernen oppretthalde tilstrekkeleg stabilitet for å vedlikehalde dei nevronale koblingane som underbyggjer langtidsminne. Dei nettlignande strukturane, kjende som Perineuronale Nett (PNN), som hovudsakleg omgjev Parvalbuminuttrykkande (PV+) interneuron i hjernebarken, trur ein dempar hjerneplastisitet, noko som tilrettelegg for langtidsminner. I denne avhandlinga brukar eg den mest presise forstyrringsteknikken for PNN så langt - å slå ut genet for *aggrecan*, ein kritisk komponent av PNN, utelukkande i PV+ nevron. Gjennom elektrofysiologiske og atferdsbaserte forsøk, samt datamodellering, undersøker eg potensielle effektar. Funna mine indikerer at transgen eliminering av *aggrecan* fjernar PNN utan å påverke PV-cellefunksjonen eller plastisiteten i synssenteret i mus. Utslåing av *aggrecan* i vaksne mus har derimot ein tydeleg effekt på plastisitet, noko som kan tyde på at det finnes kompensatoriske mekanismar som dempar effekta av å tapa *aggrecan* frå embryo-stadiet. Til slutt utviklar eg genetisk koda kalsiumindikator-konstrukt for måling av nevronaktivitet *in vivo* som overgår alle tidlegare konstrukt.

Contents

Introduction	1
1 Background	3
1.1 Brain Plasticity	4
1.1.1 Synaptic Plasticity	4
1.1.2 Critical Period Plasticity	6
1.1.3 Visual Cortex Plasticity	7
1.2 Parvalbumin Interneurons	9
1.3 Extracellular Matrix Molecules and Perineuronal Nets in Brain Plasticity	11
1.3.1 WFA reactivity	15
1.3.2 The Role of Perineuronal Nets in Neurological and Psychiatric Conditions	16
1.4 Modeling the brain	18
1.5 Calcium imaging	21
2 Objectives	25
2.1 Paper 1	25
2.2 Paper 2	25
2.3 Paper 3	26
Results and Discussion	27
3 Synopsis of Results	29
3.1 Paper 1	29
3.2 Paper 2	30
3.3 Paper 3	31
4 Discussion	33
4.1 Perineuronal net perturbations	33
4.1.1 Endogenous PNN Regulation	36

4.2	Modeling Consequences of PNN Perturbations	38
4.3	Imaging of neuronal activity.	39
4.3.1	PNNs and Calcium Imaging	41
4.4	PNNs and the Engram	42
4.5	Conclusion and Outlook	44
	Bibliography	47

Papers **67**

I	Deciphering the Role of Aggrecan in Parvalbumin Interneurons: Unexpected Outcomes from a Conditional ACAN Knockout That Eliminates WFA+ Perineuronal nets	69
----------	--	-----------

II	Responses in Fast-spiking Interneuron Firing Rates to Parameter Variations Associated with Degradation of Perineuronal Nets	111
-----------	--	------------

III	An Updated Suite of Viral Vectors for <i>in vivo</i> Calcium Imaging Using Intracerebral and Retro-orbital Injections in Male Mice	129
------------	---	------------

Preface

The research presented in this thesis was conducted at the Centre for Integrative Neuroscience (CINPLA) at the Department of Biosciences (Fac. of Mathematics and Natural Sciences) at the University of Oslo, under the supervision of Dr. Marianne Fyhn, Dr. Kristian K. Lensjø, Dr. Kristian Prydz and Dr. Anders Malthe-Sørensen. The work was funded by the Norwegian Research Council (NFR).

This thesis is a collection of three research papers, preceded by chapters on the background and motivation for the work, as well as a discussion of the presented research in the papers in a broad context.

Acknowledgments

First of all, I want to express my sincere gratitude to Marianne and Torkel for welcoming me to CINPLA in 2018, and for giving me so much freedom in the choice of which ideas to pursue. Thank you for providing me with the means to do any experiment I want, travel around the world to attend conferences, and for giving me confidence in my abilities as a scientist. Your unending enthusiasm for neuroscience will forever be an inspiration!

To Kristian, thank you for always being up for a discussion on anything neuroscience, and everything else, and for always being a super nice guy. Without your guidance, this work would not have been possible. And without your willingness to test all the fancy viruses that I scouted at various conferences, there would be no Paper III!

I am grateful to all my colleagues at CINPLA and my current and previous office-mates in the corner office, Kristian, Ingeborg, Malin, Charlotte, Alessio, and Mikkel, for being cool people and always being up for an extra break to shoot the shit. The last few years at IBV have been tumultuous. Together, we have faced a global pandemic, a closed animal facility, piles of asbestos, endless failed experiments, and various other

existential threats. Thank you for sticking it out with me!

Thanks to Ingeborg for always being up for doing extra work to test many of my half-baked ideas. And thank you, Charlotte, for establishing the retro-orbital injection technique with me, when I was fresh to animal experiments and had absolutely no idea what I was doing. Thank you, Malin, for naming your firstborn child after me. Thanks to Tina for hanging out, talking neuro, and climbing rocks in French forests. Thanks to the OG Guro Sandvik for showing me the ropes when I was fresh to molecular cloning and had absolutely no idea what I was doing. Thanks to Clive Bramham and Oleksii Nikolaienko for getting me started in Neuroscience. Thanks to Jonas for helping me make my personal website.

Thanks to all the master students that have contributed throughout my years at CINPLA: Tarjei Madland, Malin Brein, Andrea Hvideberg, Sandra Bryne, Ali Telet, and especially Valgerður Björnsdóttir for your substantial contributions to cloning and virus packaging.

Thank you to Tove Klungervik for keeping the lab at IBV running, without you it would all fall apart. And thank you for introducing me to Vera (the Dwarf Poodle), for much-needed therapy sessions during my final days of writing this thesis. I also want to thank Kristin L. Sand at IMB, who prepared buffers and solutions for my patch clamp experiments, to the great envy of every other patcher at IMB. I want to thank the computationalists at CINPLA and especially Kine, Geir, and Torbjørn for involving me in their world of computational neuroscience, and for a great collaboration that resulted in Paper II.

I am also grateful to Gaute Einevoll for many discussions on many subjects, but especially for allowing me to keep his office chair that I stole during the pandemic. And, I want to thank the intracellular ephys masters Fabian Roth, Hua Hu, and Vidar Jensen for being available to answer all my stupid questions on patch clamping, and especially Fabian for helping me patch my first PV+ cell. Thank you Addgene for distributing my plasmids. Thank you, Steinar, Christopher, and Gro at Innkjøp for helping me get everything I need, and for helping me ship way too many packages across the globe.

Thank you to my family, especially my mother and father, Gro Fatland and Ottar Grødem, my clone Oddbjørn and my older brother Gjermund, for making me dinner and keeping me company, and for supporting me in all my endeavors. Thank you, Pappa, for helping me transport dry ice for

shipping viruses, from IMB to IBV when the university terminated their rental car agreement. Thank you to my nibblings Hanna and Sigurd, you're the coolest Grødemers.

And, finally, I want to thank Guro H. Vatne, my partner in science, life, and so on. For always being around to cheer me up, at work, at home, in the forest, etc. Thank you for improving my cloning efficiency, critiquing my pipetting, and in general; showing me how it's done. And, of course, thank you for your many experimental, intellectual, and artistic contributions to the work presented here.

Introduction

Chapter 1

Background

In 1887, the Norwegian explorer and scientist Fridtjof Nansen completed his Ph.D. thesis, where he posited that nerve cells were individual entities. This idea, termed the Neuron Doctrine, is a milestone in Neuroscience that later earned Ramón Y Cajal the Nobel Prize. 136 years later, we know much more about the inner workings of the brain. We have a good understanding of the basic building blocks, the neurons, and we know that they communicate with each other through excitatory or inhibitory chemical and electrical signals. We have made strides in mapping which areas of the brain are responsible for different functions and behaviors, and advancements in imaging technology have allowed us to visualize the brain in action and observe changes in the brain related to various neurological and psychiatric disorders. However, how these elements combine to produce consciousness, cognition, memory, and behavior is far from understood. The brain contains approximately 86 billion neurons and an estimated 100 trillion synapses, making it an extraordinarily complex system to study. Furthermore, the brain is not static, but rather changes and adapts over time in a process termed brain plasticity, adding another layer of complexity to its study.

In my Ph.D. thesis, I use electrodes to measure electrical activity in a type of inhibitory neuron in the brain of mice. I perturb these cells using genetic techniques and investigate the effects of this perturbation on the plasticity of the brain. I apply computational models of neurons to study the effects of this perturbation in detail. And finally, I study excitatory neurons in the brain using a jellyfish protein that has been engineered to fluoresce in response to neuronal activity; I introduce the gene for this protein to the brain via a recombinant virus that was designed to cross the blood-brain barrier.

1.1 Brain Plasticity

Brain plasticity refers to the remarkable ability of the brain to change and adapt throughout an individual's life in response to experiences and environmental influences. The brain is born immature and then adapts to sensory inputs after birth. Brain plasticity enables learning, memory formation, and retention; our ability to adapt to the world around us. The term brain plasticity envelops all mechanisms that contribute to plasticity in the brain. In this thesis, I will focus on synaptic plasticity and particularly its relation to perineuronal nets.

1.1.1 Synaptic Plasticity

Synaptic plasticity broadly refers to the ability of synaptic connections between neurons to undergo changes in their strength or efficacy based on activity. The primary forms of synaptic plasticity are Hebbian plasticity and homeostatic plasticity. Hebbian plasticity, which gets its name from Donald O. Hebb who proposed it in 1949 (Hebb 1949), postulates that if activity in a presynaptic neuron repeatedly drives firing in a postsynaptic neuron, their connection will be enhanced. This mechanism is often summarized with the phrase "neurons that fire together, wire together". Existing synapses can be potentiated, i.e., their activation has a greater effect on the postsynaptic cell, or depressed; their activation has a reduced effect on the postsynaptic cell for an extended time. The biochemical basis of these changes involves complex processes that lead to changes in the number or responsiveness of synaptic receptors, the synthesis and release of neurotransmitters, and structural changes to the synapse. Crucially, these changes can be bidirectional, i.e., they can either strengthen or weaken synaptic connections, and this flexibility allows for the fine-tuning of neural circuits that underlies our ability to learn and adapt to our environment.

Long-term potentiation (LTP) refers to the persistent, activity-dependent enhancement of synaptic transmission. This process typically involves an increase in the number or sensitivity of postsynaptic AMPA-type glutamate receptors in the postsynaptic membrane, which results in a stronger response to a given presynaptic stimulus. LTP can be triggered by high-frequency stimulation of the synapse, leading to a long-lasting increase

in synaptic strength. Conversely, long-term depression (LTD) is a process by which synaptic strength is reduced over the long term and is typically associated with low-frequency stimulation. The process of LTD usually involves a reduction in the number or sensitivity of postsynaptic AMPA receptors, thereby diminishing the synapse's response to a given presynaptic stimulus.

To summarize, Hebbian plasticity states that if neuron A consistently contributes to the firing of neuron B, the synapse from A to B is strengthened. However, without a counterbalancing mechanism, Hebbian plasticity can lead to a positive feedback loop, where strong synapses become stronger and weak synapses become weaker, potentially leading to overly active or inactive neurons. This is where homeostatic mechanisms of plasticity come in.

Homeostatic plasticity adjusts the overall excitability of neurons to keep their activity within a functional range (Keck et al. 2017; Zenke, Hennequin and Gerstner 2013). It acts as a balancing mechanism to prevent the network from becoming too excitable (leading to issues like seizures) or too inhibited (resulting in reduced responsiveness). It also ensures that neurons maintain their ability to modify the strength of their synapses in both directions, which is necessary for ongoing learning and adaptation. While Hebbian plasticity could lead to a runaway process where strong synapses keep getting stronger, homeostatic plasticity prevents this by weakening all of a neuron's synapses when the neuron is overly active and strengthening them when the neuron is not active enough. Therefore, Hebbian and homeostatic plasticity work together to enable the brain to form memories and learn from new experiences while maintaining stable network activity.

In summary, synaptic plasticity is a fundamental property of the brain that allows it to adapt to new information, experiences, and environments. Understanding these processes in greater detail can provide valuable insight into how learning and memory occur, and how certain diseases and conditions might affect these processes. Notably, many unanswered questions remain at the center of our theories of synaptic plasticity, for example, how plasticity is facilitated over longer time scales (Bittner et al. 2017). Moreover, while it is widely believed that synaptic plasticity is the facilitator of memory in the brain; what actually constitutes a physical memory in the brain is not known. A leading theory of memory storage

states that distinct pieces of information, or memory traces, are stored in assemblies of connected neurons, termed "engrams". An engram is a hypothetical permanent change in the brain that results from a stimulus and forms the basis of memory (Josselyn, Köhler and Frankland 2015; Josselyn and Tonegawa 2020). Although, what specifically constitutes an engram, or memory trace, in the brain, remains a topic of debate in neuroscience. In this thesis, I focus mainly on the role of an extracellular matrix structure, the perineuronal net (PNN), in plasticity, rather than its proposed role as a substrate for engrams (Lev-Ram et al. 2023; Roger Y. Tsien 2013); particularly during a period of heightened plasticity in juvenile animals, the critical period.

1.1.2 Critical Period Plasticity

Critical period plasticity (or critical phase plasticity) refers to a specific period in early postnatal development when the brain exhibits heightened plasticity and is particularly sensitive to specific environmental inputs and experiences. During this critical period, the brain can undergo significant changes in structure and function (Levelt and Hübener 2012). One of the first studies of a critical period of learning in animals was on the imprinting of nidifugous birds, which leave the nest shortly after hatching, on any nearby moving object. When the researcher interacted with the birds in a critical window of 13-16 hours after hatching, the geese subjects would treat the researcher as a substitute mother (Levelt and Hübener 2012; Lorenz 1935).

Alterations in the brain during the critical period can be detected at various levels, from sensory learning in humans to individual neuron responses and changes in dendritic spines in the rodent visual cortex (Elbert et al. 1995; Hofer et al. 2009; WIESEL and HUBEL 1963). Most of our understanding of the mechanisms responsible for activity-dependent plasticity during development comes from studying sensory systems in animal models, including song-learning birds, primates, rodents, and owls (Levelt and Hübener 2012). The timing of the critical period is directed by a sequence of genetic mechanisms influenced by activity (Katz and C. J. Shatz 1996). Typically, sensory systems take the lead, while more advanced cognitive functions, such as math skills and critical thinking, are believed to have similar windows of flexibility later in development. The onset of

critical period plasticity in diverse fields such as bird song learning and mouse vision is in part regulated by circadian rhythms, activating specific genetic pathways controlling neuronal development (Kobayashi, Z. Ye and Hensch 2015; Nordby, Campbell and Beecher 2001).

After the period of heightened plasticity in juvenile animals, the brain's capacity for large-scale reorganization diminishes. Entering adulthood, neuronal circuits, particularly inhibitory elements, mature and dampen plasticity, likely improving the ability to retain acquired skills and memories at the cost of reduced plasticity.

1.1.3 Visual Cortex Plasticity

Information from the visual field from both eyes is conveyed in parallel routes through the dorsal lateral geniculate nucleus (dLGN) to the binocular region of the primary visual cortex (V1). This is where inputs from both eyes merge, forming a coherent representation. In V1, a synaptic-level competition for target cells occurs between inputs from both eyes, with the outcomes determined during the critical period. Following normal development, V1 excitatory neurons are more responsive to stimulation of the contralateral eye relative to stimulation of the ipsilateral eye (Dräger 1978; D. H. Hubel and T. N. Wiesel 1962). If one eye is vision-deprived during the critical period, cortical neurons alter their preference and become more responsive to the open eye (Figure 1.2). Prolonged deprivation leads to substantial structural changes in the thalamocortical pathway and can eventually result in functional blindness (Antonini and Stryker 1996; Headon and Powell 1973), a condition known as amblyopia in humans.

In the visual cortex of some animals, such as cats, ferrets, and primates; neurons with similar ocular dominance (OD) properties are arranged into cortical columns (David Hunter Hubel and Torsten Nils Wiesel 1997; Levay, Stryker and Carla J. Shatz 1978). This organization can be influenced by interference with GABAergic development within V1 (Hensch and Stryker 2004). Notably, the V1 of rodents such as mice lack this columnar organization and neurons with varying OD properties are mixed together, but they also depend on GABA and binocular (OD) responses to mature (Antonini, Fagiolini and Stryker 1999).

After the critical phase, LTP in thalamocortical connections diminishes, but it persists within the visual cortex and can be significantly potentiated

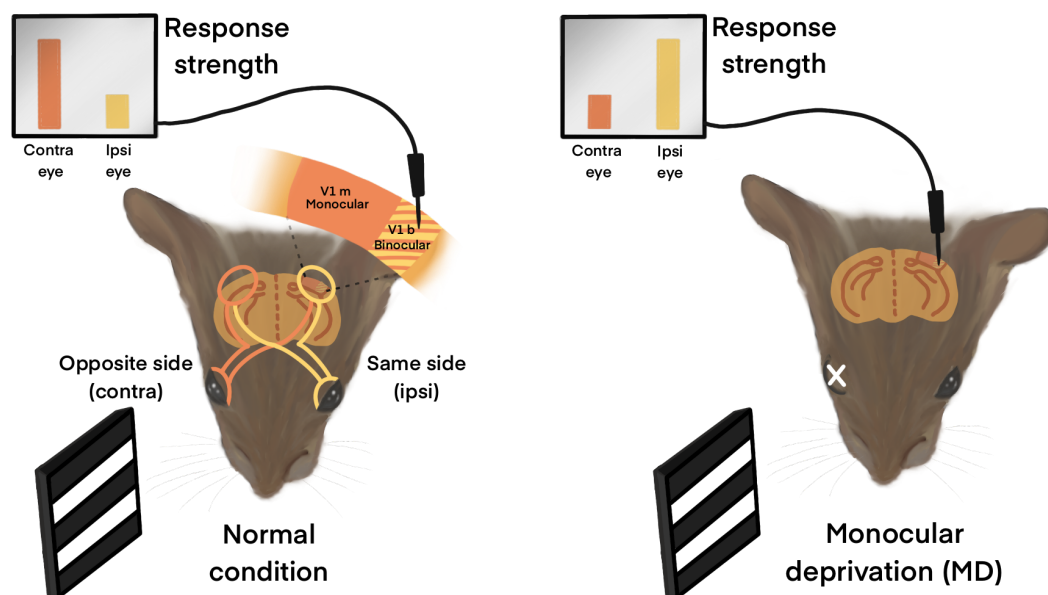


Figure 1.1: Monocular deprivation during the critical period causes a shift in ocular dominance. When one eye is closed for several days during the critical period, and then re-opened, the response strength in the binocular zone is altered in favor of the non-deprived eye. Artwork contributed by Guro and Associates.

by experimentally applied theta-burst stimulation (Crair and Malenka 1995). This indicates that although ocular dominance input-matching is decided during the critical period, intracortical connections can still be adapted later in life. On the other hand, LTD is enhanced during the critical period but cannot be initiated later. This implies that LTD may be responsible for the functional changes observed in juvenile animals after monocular deprivation (Kirkwood, Silva and Bear 1997). Such observations point to possible mechanistic differences in plasticity between the juvenile and adult brains, where LTD drives OD plasticity in juveniles.

However, studies have shown that with certain treatments, juvenile-like plasticity can be reinstated in the visual cortex of adult rodents. An example of this is the digestion of chondroitin sulfate proteoglycans (CSPG) in the extracellular matrix by a bacterial enzyme, Chondroitinase-ABC (Pizzorusso, Medini, Berardi et al. 2002). This effect is frequently attributed to the degradation of the perineuronal nets surrounding Parvalbumin-expressing interneurons, a type of GABAergic (inhibitory) interneuron.

1.2 Parvalbumin Interneurons

Parvalbumin-expressing (PV+) interneurons are a subclass of inhibitory (GABAergic) neurons found abundantly in the brain (Figure 1.2). These neurons are characterized by their fast-spiking activity and the expression of the calcium-binding protein parvalbumin (H. Hu, Gan and P. Jonas 2014). Parvalbumin acts as a slow calcium buffer and appears to function as an anti-facilitation factor in presynaptic terminals (Caillard et al. 2000; Eggermann and Peter Jonas 2012). Synaptic facilitation, a short-term increase in synaptic strength, can be mediated by increased post-synaptic calcium-ion concentration. When Ca^{2+} ions bind to parvalbumin, the concentration of free Ca^{2+} ions is reduced, thus preventing facilitation.

Parvalbumin+ neurons play a crucial role in the generation of rhythmic brain activity, particularly gamma oscillations (30-80 Hz), which are believed to be essential for various cognitive processes such as attention, perception, and memory (Cardin et al. 2009; Sohal et al. 2009). PV+ interneurons predominantly connect with cell bodies and axon initial segments of pyramidal neurons, which are the primary excitatory neurons in the cerebral cortex. This close proximity of PV+ inhibitory synapses to the site of axon potential initiation allows them to tightly regulate the activity of the post-synaptic cell (H. Hu, Gan and P. Jonas 2014). By controlling the output of pyramidal neurons, PV+ interneurons play a key role in synchronizing local network activity and the brain's excitatory-inhibitory balance.

PV+ interneurons mature late in postnatal development. They integrate into V1 at the onset of critical period plasticity (Alcántara, Ferrer and Soriano 1993; Sugiyama et al. 2008). During this time, they undergo significant changes, including increased expression of Parvalbumin, formation of synaptic connections, and development of their characteristic fast-spiking properties (H. Hu, Gan and P. Jonas 2014). The maturation process is influenced by neuronal activity and sensory experiences, indicating a close interplay between the development of PV+ interneurons and the environment (Miller et al. 2011). PV+ interneurons play a crucial role in regulating the onset and closure of critical periods of plasticity in the primary visual cortex (Kuhlman et al. 2013; Yazaki-Sugiyama et al. 2009). The maturation of these neurons, specifically their increasing inhibition of pyramidal neurons, is believed to trigger the start of the critical period

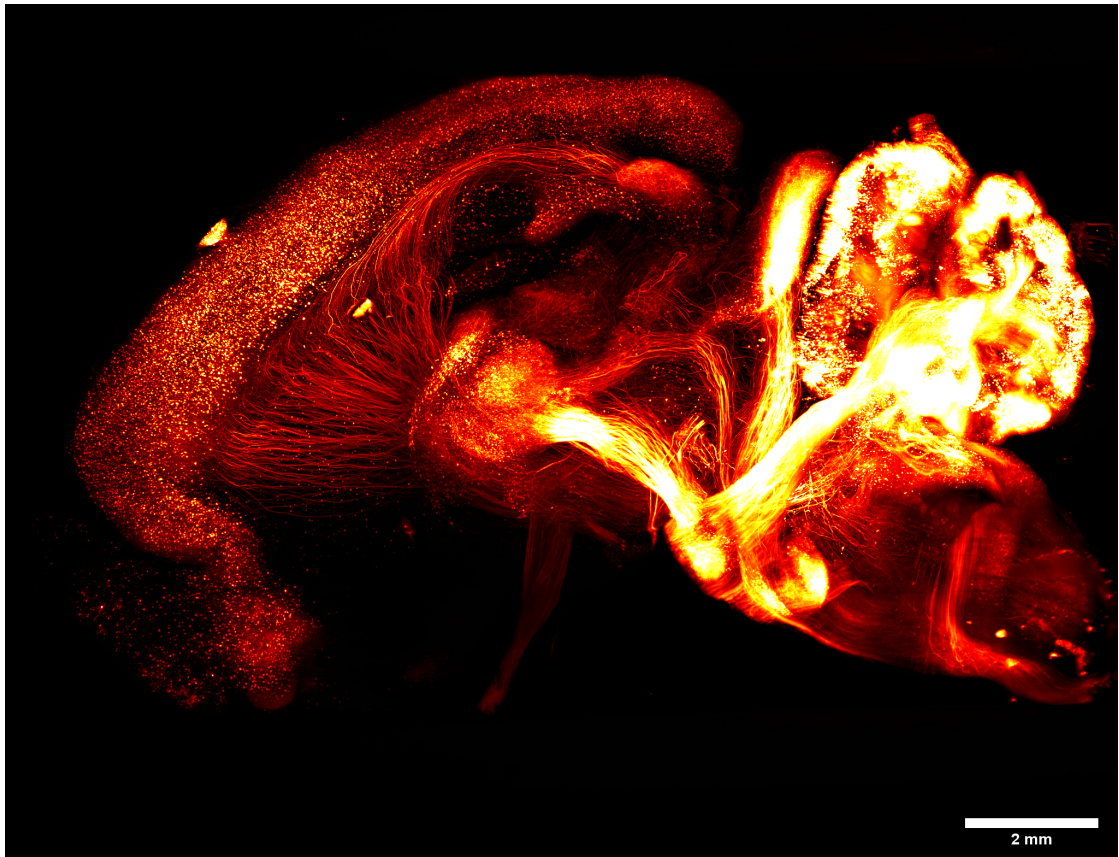


Figure 1.2: Parvalbumin neurons across the mouse brain. Visualized with a systemic FLEX-tdTomato PHP.eB AAV virus, in a PVcre mouse line, which produces red fluorescence in PV+ neurons. The mouse brain was made transparent with the tissue-clearing method CLARITY and imaged on a light-sheet microscope. S. Grødem, Unpublished results.

(Kuhlman et al. 2013). Once the critical period opens, sensory experience drives the strengthening or weakening of synapses on the pyramidal neurons, allowing functional refinement of the cortical network.

Toward the end of the critical period, perineuronal nets (PNNs) condense on the membrane of PV+ interneurons. The formation of PNNs is thought to contribute to the closure of the critical period through contributions to PV+ neuron maturation, and to their fast-firing properties (Carulli, Pizzorusso et al. 2010; Pizzorusso, Medini, Berardi et al. 2002; Rowlands et al. 2018).

1.3 Extracellular Matrix Molecules and Perineuronal Nets in Brain Plasticity

A significant proportion of the brain is extracellular space, up to 10 to 20%. This space is in part inhabited by the extracellular matrix (ECM); structures composed of sugars and peptides that play essential roles in brain development, axon guidance, plasticity, and tissue coherence (Kwok et al. 2011; R. K. Margolis, R. U. Margolis et al. 1975; Nicholson and Syková 1998; Wang and J. Fawcett 2012).

Perineuronal nets (PNNs) are condensed, reticular structures of the extracellular matrix that mainly forms around PV+ interneurons in the cerebral cortex (Figure 1.3). Because PNNs are highly stable structures, and the holes in the net-like structure are filled by synapses, some have theorized that PNNs stabilize synapses long-term, and more specifically that they stabilize engrams (Lev-Ram et al. 2023; Roger Y. Tsien 2013). I discuss this hypothesis further in section 4.4 of the discussion chapter.

Perineuronal nets are comprised of a specific family of chondroitin-sulfate proteoglycans (CSPGs), known as lecticans, which are large structural proteins with an extended peptide core that is extensively glycosylated with chondroitin sulfate chains. Aggrecan, the largest lectican, can be equipped with approximately 100 molecules of chondroitin sulfate chains, of 20kDa each, which adds up to about ten times the weight of the polypeptide chain (Hardingham and Fosang 1992). The CSPGs in PNNs are bound to hyaluronic acid (HA) chains attached to cells in the hyaluronan synthase from which the HA chains are produced. Lectican binding to HA is stabilized by the link protein HAPLN1 (or Ctrl1), and extracellular CSPGs

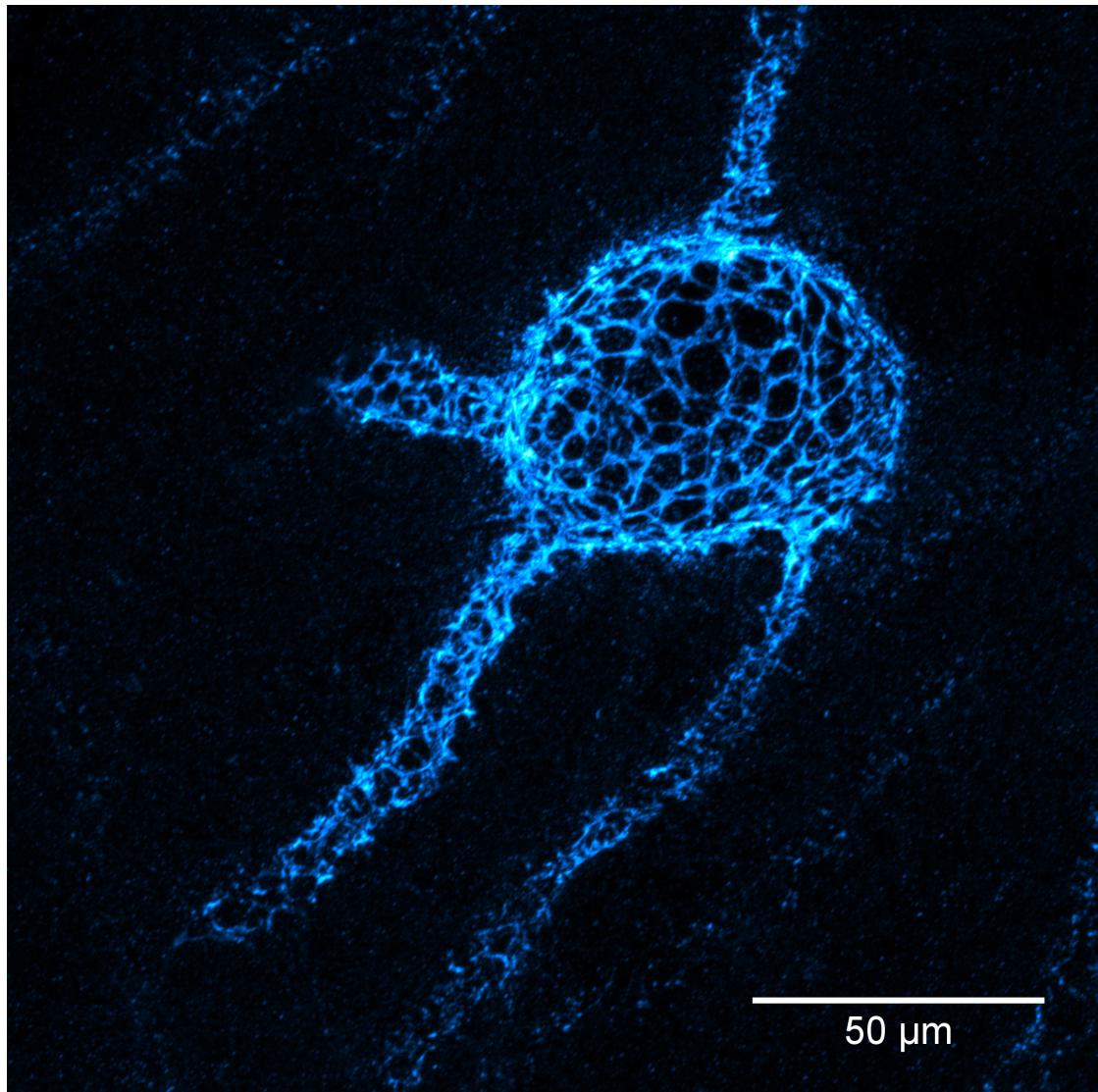


Figure 1.3: Wisteria Floribunda Agglutinin (WFA) labeled Perineuronal net in mouse entorhinal cortex. Imaged by expansion microscopy (unpublished results). The scale bar is post 4.5x expansion.

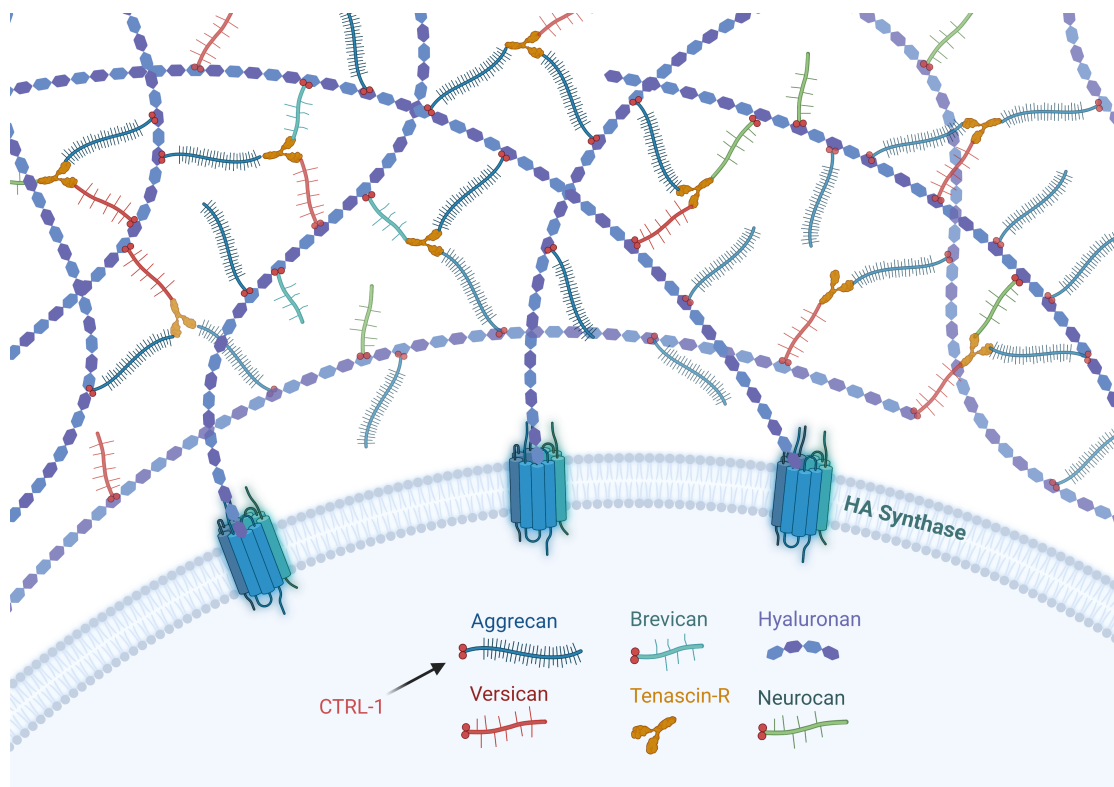


Figure 1.4: Primary structural components of Perineuronal Nets. Hyaluronan (HA) is extruded from and attached to HA synthase in the plasma membrane. The lecticans aggrecan, brevican, neurocan, and versican bind the HA chains. This binding is stabilized by CTRL-1 (HAPLN-1). Tenascin-R cross-links the lecticans to form the final ternary structure.

are cross-linked by Tenascin-R, forming the final ternary structure (1.4). These components are also prevalent in ECM outside of PNNs, although Aggrecan and Ctrl1 are up-regulated at the start of the critical phase and are more specific to PNNs (Matthews et al. 2002; Markus Morawski et al. 2012; Q. Ye and Miao 2013). PNNs may be detected by immunostaining for any of these proteins, but more commonly, they are detected and defined by Wisteria Floribunda Agglutinin (WFA) lectin staining in a condensed, reticular pattern on somata and perisomatic dendrites. I will elaborate on the use of WFA in PNN research in the next section.

The assembly of PNNs in the cortex occurs mainly on PV+ interneurons, with some exceptions. In the CA2 area of the hippocampus, for instance, PNNs also envelop excitatory pyramidal neurons (Carstens et al. 2016). Interestingly, the condensation of PNNs coincides with the maturation of PV+ cells and the closure of the critical period of heightened plasticity in e.g., V1 (Pizzorusso, Medini, Berardi et al. 2002). Like PV+ neuron maturation, PNN development is activity-dependent and will be postponed by a lack

of stimulus, for example by dark rearing (Dityatev et al. 2007; Pizzorusso, Medini, Landi et al. 2006). In several areas of the brain, removal of PNN by enzymatic digestion has been shown to increase plasticity, including the V1 (Pizzorusso, Medini, Berardi et al. 2002; Pizzorusso, Medini, Landi et al. 2006), auditory cortex (Happel et al. 2014), amygdala (Gogolla et al. 2009) and perirhinal cortex (Romberg et al. 2013).

In the adult brain, PNNs are posited to regulate the function of PV+ interneurons, potentially limiting plasticity while enhancing PV+ neuron firing rates (Favuzzi et al. 2017; Lensjø, Lepperød et al. 2017; Marín 2016; Tewari et al. 2018). However, the exact mechanism and magnitude of the influence PNNs may exert on the high-frequency firing phenotype of PV+ neurons is not known. Using the patch clamp method, where an electrode submerged in a salt solution mimicking the composition of the cytosol is connected to the intracellular space, an electrical current can be injected to drive action potential firing. As the magnitude of the injected current is gradually increased, the maximum firing frequency of action potentials can be determined. A series of patch clamp investigations have reported mixed results of PNN perturbation, with some identifying no significant influence on firing frequency (Chu et al. 2018; Faini et al. 2018; Hayani, Song and Dityatev 2018), while others record marked reductions (Balmer 2016; Favuzzi et al. 2017; Liu, Yujie Zhang and Ju 2022; Liu, Yujie Zhang, Men et al. 2023; Tewari et al. 2018).

A recent literature review highlighted that among the studies that examined PV+ cell firing rates after PNN perturbation, seven out of twelve studies identified a decrease in firing rate, five reported no change, while none noted an increase (Wingert and B A Sorg 2021). However, comparing these studies is not necessarily straightforward, as there are variations in PNN perturbation methods, targeted brain regions, and mice of different ages are used. Moreover, the review groups extracellular and intracellular electrophysiology papers from *in vivo* or *in vitro* studies. These investigations predominantly used the bacterial enzyme Chondroitinase-ABC (chABC) for enzymatic digestion of chondroitin sulfate glycosaminoglycans on CSPGs. However, this approach is not specific to CSPGs within PNNs, which comprise only 2-5% of the total amount of CSPGs in the brain (Deepa et al. 2006). Moreover, variability in the enzyme's source (Sigma or AMSBIO/Seikagaku), concentration, volume, and incubation period further compounds this complexity. Notably, a study

that observed a reduction in the firing rate of PV+ interneurons after enzyme treatment theorizes that this change may be attributed to an increase in effective capacitance in PV+ cells treated with chABC (Tewari et al. 2018). In Paper 2, we tested this hypothesis using computational modeling.

1.3.1 WFA reactivity

Wisteria Floribunda Agglutinin (WFA) lectin reactivity is commonly used to define PNNs in the literature (J. W. Fawcett, Oohashi and Pizzorusso 2019)(Figure 1.5). While the exact binding site of WFA lectin is not known, it is believed to be on chondroitin-sulfate chains, which are lost along with WFA reactivity when PNNs are treated with the chondroitin-sulfate digesting enzyme chABC and by pan-neuronal knockout of Aggrecan (Rowlands et al. 2018), indicating that the binding site might be on the CS chains of ACAN. Notably, not all WFA staining correlates to aggrecan staining, and not all aggrecan staining correlates to WFA staining (Galtrey et al. 2008). Nevertheless, WFA is generally considered a marker of PNNs in the literature (J. W. Fawcett, Oohashi and Pizzorusso 2019; Lupori et al. 2023).

Relying on WFA or other lectins and antibodies that target chondroitin sulfate chains can, potentially, determine if a perturbation removed CS chains, but not necessarily the core proteins of CSPGs. Although, studies have suggested that sulfotransferase modification of sulfation patterns on CS chains affects WFA reactivity (Shinji Miyata and Kitagawa 2016). One study found that WFA reactivity varies across a mouse's circadian rhythm, and suggests that this could be due to changes in sulfation patterns (Pantazopoulos et al. 2020). Unfortunately, this study did not include staining for aggrecan peptide. As WFA reactivity may be less stable than the PNN superstructure, one should always include secondary detection methods for PNNs, for example, antibody staining for aggrecan or other PNN CSPGs. Notably, one study found that up to two-thirds of PNNs are lost in post-mortem brain sections of Alzheimer's patients (Baig, Wilcock and Love 2005), based on WFA reactivity. However, a later study failed to replicate these findings and, in fact, found no change in PNNs in Alzheimer's patients based on both WFA reactivity and Aggrecan immunostaining. They attribute earlier results to post-mortem decay of WFA reactivity, which can occur within 4-8 hours after death (Markus

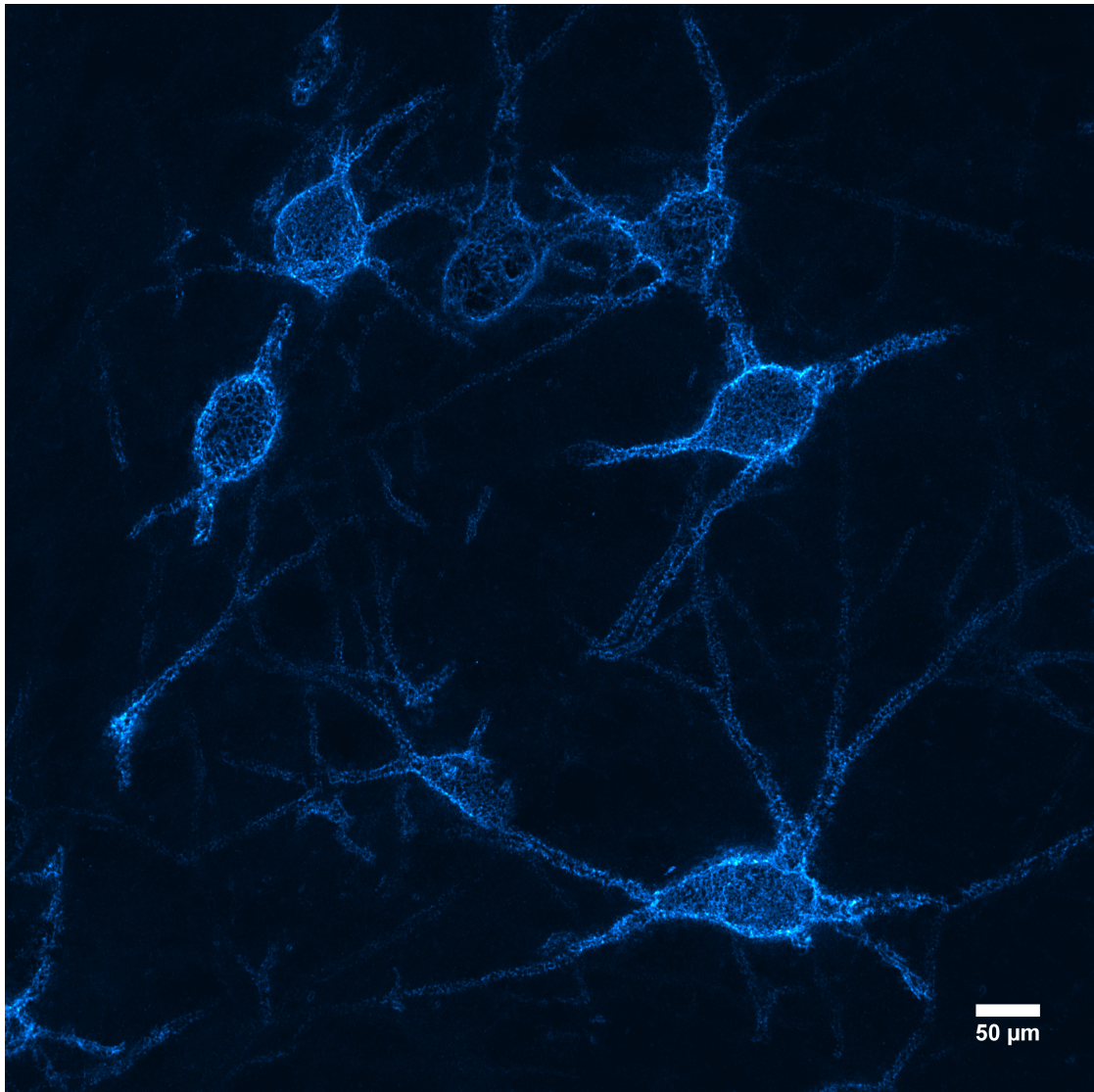


Figure 1.5: WFA labeled perineuronal nets in the entorhinal cortex. Imaged with expansion microscopy. Scale bar post 4.5x expansion. Unpublished results.

Morawski et al. 2012).

1.3.2 The Role of Perineuronal Nets in Neurological and Psychiatric Conditions

Perineuronal nets (PNNs) are increasingly recognized for their role in various brain diseases (Wen et al. 2018). PNN deficits are correlated with several neurological and psychiatric conditions, including Alzheimer's disease, schizophrenia, epilepsy, and fragile-x syndrome (Wen et al. 2018). Alzheimer's disease (AD) is a neurodegenerative condition characterized by the progressive loss of cognitive functions, often attributed to intra-

cellular neurofibrillary tangles and extracellular deposits of amyloid-beta (Alzheimer et al. 1995; Berchtold and Cotman 1998). While some studies report increased degradation of PNN components in the brains of Alzheimer's patients (Baig, Wilcock and Love 2005), others indicate that cells enveloped by PNNs were less likely to exhibit Tau and neurofibrillary tangle accumulation, suggesting that the PNNs have a neuroprotective effect (M. Morawski et al. 2010; Markus Morawski et al. 2012; Scarlett, S. J. Hu and Alonge 2022). PNN-bearing neurons were more resistant to the effects of exogenous amyloid-beta, but this resistance was lost after treatment with chABC (Seiji Miyata, Nishimura and Nakashima 2007), a treatment that removes the CS chains on CSPGs in PNNs. PNNs may provide neuroprotection by shielding against oxidative stress-inducing molecules like metal ions, which can amplify free radical production, leading to cell death (Stohs and Bagchi 1995). Studies also reveal higher survival rates of PNN-clad neurons in Alzheimer's rodent models, where oxidative stress is simulated by injecting iron chloride (A. Suttikus et al. 2014; Anne Suttikus et al. 2012). The reduction of aggrecan, the major carrier of negatively charged CS-side chains in PNNs, correspondingly lessens these neuroprotective effects (A. Suttikus et al. 2014). This evidence strengthens the hypothesis that PNNs' CS-side chains play a pivotal role in neuroprotection.

Schizophrenia, a severe psychiatric disorder marked by symptoms such as hallucinations, delusions, and cognitive challenges, is another condition in which PNN abnormalities have been noted (Berretta et al. 2015). Dysfunctional PNNs in schizophrenia might induce changes in GABAergic cell function leading to network dysfunction, as normal PNN expression is believed to regulate the excitability of PV+ neurons (Balmer 2016; Tewari et al. 2018). Furthermore, as for AD, PNNs appear to protect PV+ neurons from oxidative stress in Schizophrenia (Cabungcal et al. 2013). Several studies have found reduced PNN levels in post-mortem brain tissues from schizophrenia patients (Enwright et al. 2016; Mauney et al. 2013), as well as in mouse models of the disease (Cabungcal et al. 2013). Further studies are needed to validate these findings and understand the links between ECM abnormalities, GABAergic signaling changes, and redox dysregulation in schizophrenia.

Epilepsy, a neurological disorder characterized by recurrent, unprovoked seizures, is also associated with changes in PNNs. Several studies on drug-induced seizures have found alterations in PNN integrity in epilepsy,

including an increase in aggrecan cleavage products, a reduction in PNN components, and elevated unbound CSPG levels (McRae and Porter 2012; Rankin-Gee et al. 2015; Yutsudo and Kitagawa 2015). This PNN breakdown following seizure induction is partly facilitated by increased enzymatic activity of metalloproteases (MMPs) (Rankin-Gee et al. 2015; Wilczynski et al. 2008). Seizure susceptibility was reduced in MMP-9 KO mice, implying that PNN breakdown via MMP-9 contributes to pathological hyperexcitability (Wilczynski et al. 2008). I will elaborate on the role of proteases in PNN regulation in the discussion, section 4.1.1.

In conclusion, emerging evidence points to PNN significantly impacting neurological and psychiatric disorders. Gaining a better understanding of the specific role of PNNs in these conditions may lead to new opportunities for treatment. Further research is required to elucidate the complex correlation between PNNs and various pathological processes occurring in the brain.

1.4 Modeling the brain

The human brain, and even the brains of very small animals such as mice or fruit flies, are incomprehensibly complex. Indeed, a single neuron, with its thousands of synapses and intricate branching structures of both dendrites and axons, with a rich diversity of ion channels and dynamic membrane properties, presents a puzzle of profound complexity. Consider then, that the human brain comprises an estimated 86 billion neurons (Herculano-Houzel 2009)! Given this complexity, we depend on tools that can help us unravel how the brain and its neurons function: computational (or mathematical) models.

Computational models of neurons and networks of neurons allow us to simulate the interplay of many components simultaneously. We can generate complex models of single neurons based on electrophysiological recordings and structural data, or simulate how tens to thousands of excitatory and inhibitory neurons would respond to, for example, increased inhibitory activity (Sterratt et al. 2023). The field of neuroscience has a wealth of experimental data, from molecular to behavioral levels. Computational models can help integrate these data into coherent frameworks, providing a way to understand how phenomena at different scales relate to one another. Models can help us understand how molecular changes,

for instance, in the extracellular matrix, can affect single neurons and neuronal network function. Researchers can vary parameters and test different conditions *in silico*, and make predictions about the outcome. These predictions can be tested experimentally, providing a powerful method for advancing our understanding of brain function.

The Hodgkin-Huxley model of the squid giant axon, named after Alan Hodgkin and Andrew Huxley, who developed it in 1952, is a model that describes how action potentials and synaptic potentials in neurons are initiated and propagated (Hodgkin and Huxley 1952). Their pioneering work, which laid the foundation for biophysics-based neural modeling and won them the Nobel Prize in Physiology or Medicine in 1963, was primarily based on experimental studies of the squid's giant axon, which is unusually large and thus easier to study (Figure 1.6A). The basis of the model is a set of four differential equations describing the flow of sodium and potassium ions through voltage-gated ion channels in the axonal membrane. These ion flows are responsible for the action potential's characteristic shape and the refractory period that follows the action potential. The Hodgkin-Huxley model was groundbreaking because it provided a quantitative description of the electrical behavior of neurons and allowed predictions about how neurons would respond under different conditions or to changes in the conductance of specific ion channels.

However, it is worth noting that while the Hodgkin-Huxley model accurately describes the action potential, it simplifies or ignores many aspects of neuronal function. For example, it does not account for the varying properties of different types of neurons, the great diversity of ion channels, or the complex structure of neurons with their intricate dendrites and axons. While core properties of neurons are shared across all animals, the most accurate model for a given animal and cell type would be one generated from data from a similar animal and cell type. The complexity of neuron models can vary greatly; the simplest models, the "point-neuron" or "single-compartment" models, treat the neuron as a single, homogeneous, equipotential compartment. These models ignore the spatial structure of the neuron and assume that the electrical potential is the same at every point in the neuron. Single-compartment models can be very useful for studying phenomena where the precise structure of the neuron is not crucial. They allow researchers

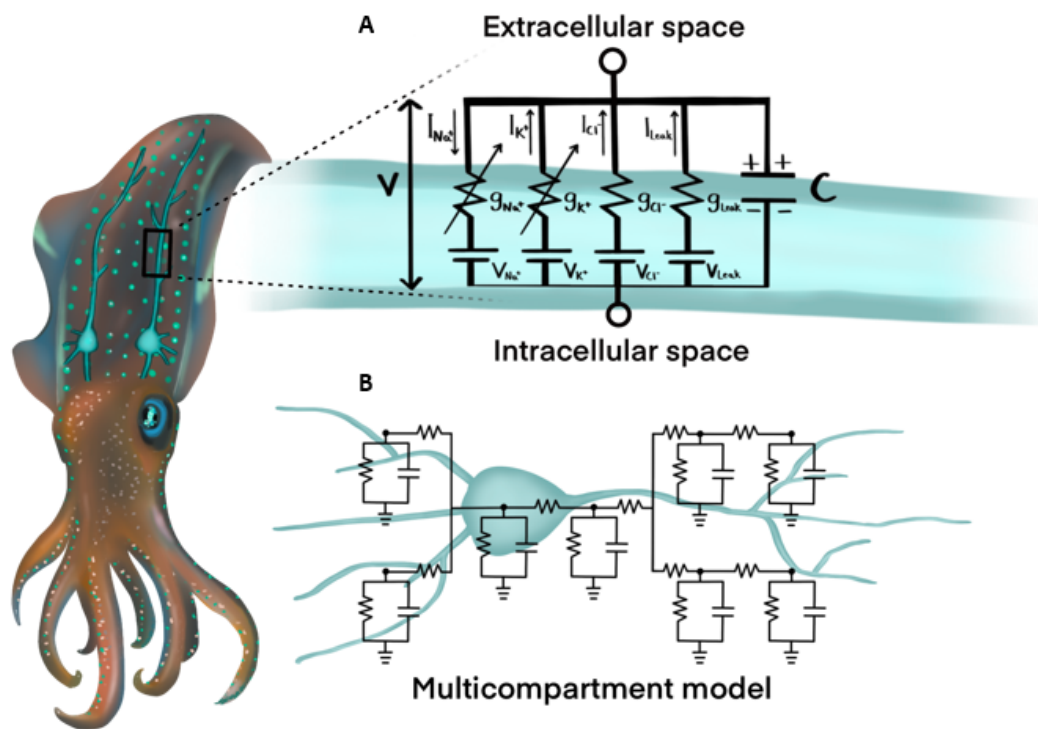


Figure 1.6: Computational models of neuron electrophysiology. A) Hodgkin-Huxley model of the squid's giant axon. **B)** Multicompartment model. Artwork by Guro and Associates.

to focus on the essential features of neuronal function and to simulate networks of many neurons without requiring excessive computational resources and complexity. However, physical neurons have complex spatial structures, with branching dendrites and axons that greatly affect their electrical properties. To account for this complexity, multi-compartment models divide the neuron into several compartments or sections, each treated as a separate but connected electrical circuit (Figure 1.6B). These compartments are typically connected in a tree-shaped structure that reflects the morphology of the neuron. The voltage and current can then vary in different parts of the neuron, and the model can account for the propagation of signals along dendrites and axons. Multi-compartment models can provide a more accurate representation of the electrical behavior of neurons, particularly for phenomena that depend on the spatial structure of the neuron, such as the integration of synaptic inputs along dendrites (Sterratt et al. 2023).

In conclusion, computational modeling is an essential tool in neuroscience that complements traditional experimental methods. By providing a way to integrate data, test hypotheses, and understand complex systems, it contributes significantly to our understanding of the brain and the development of effective treatments for neurological disorders. In this thesis, computational modeling is applied to probe the effects of PNN perturbation on PV+ neurons.

1.5 Calcium imaging

In order to comprehend the interaction between PNNs, plasticity, and neural activity, it's crucial to possess tools that enable the monitoring of these contributing factors in vivo. Calcium imaging is a powerful tool used in neuroscience to visualize the activity of neurons, which allows researchers to observe and measure the behavior of large populations of neurons in real-time. When a post-synaptic neuron receives an excitatory input, and during an action potential, free calcium ions enter the neuron, effectively increasing intracellular Ca^{2+} concentration. This can be used as a proxy for synaptic or action potentials, as a measure of neuronal activity. Although, one should keep in mind that the time scales of calcium ion flow are significantly delayed relative to rates of membrane potential change. Calcium imaging has been widely used for studying functional

connectivity in neuronal networks, understanding brain plasticity, and exploring the mechanisms of various neurological diseases.

Two main types of calcium indicators let us measure intracellular calcium dynamics: synthetic dyes such as Fura-2 (Grynkiewicz, Poenie and R Y Tsien 1985) and genetically encoded calcium indicators (GECI) such as the GCaMP6 indicators (T.-W. Chen et al. 2013). Synthetic dyes are usually loaded into cells through microinjection, while GECIs are introduced into neurons by viral vectors or transgenic techniques. Each type of indicator has its pros and cons, with synthetic dyes generally offering higher signal intensity and fast kinetics but lower specificity, while GECIs offer cell-type specificity and chronic imaging capabilities but may have lower signal-to-noise ratios. Notably, it was recently discovered that BAPTA-derived calcium dyes, such as Fura-2, inhibit actomyosin ATPase (Robinson et al. 2023), which may compromise experimental results.

Calcium imaging, mainly through GECIs, has transformed neuroscience research, providing a high-resolution, noninvasive means to study the activity of neurons in living tissues (Grienberger and Konnerth 2012; Lin and Schnitzer 2016). GECI imaging allows scientists to simultaneously record the activity of thousands of neurons in real time, providing a much more detailed picture of neuronal network dynamics than traditional single-cell electrophysiological methods. Moreover, as GECIs are genetically encoded, they permit selective monitoring of specific subsets of neurons, including those defined genetically, or connected anatomically. This allows for longitudinal studies of neuronal dynamics across various life experiences, developmental stages, or disease progression (Luo, Callaway and Karel Svoboda 2018). Importantly, optical imaging minimizes neuronal damage. It only requires optical access. This can be achieved with minimally invasive methods, like cranial windows, which are less disruptive than electrodes that need to be positioned within close proximity of the cells under study. Nevertheless, imaging deeper brain structures is still hard to achieve non-invasively, as it would typically require the implantation of optical lenses. The capacity to avoid local perturbation also enhances long-term imaging feasibility, although over-expression of GECIs over extended periods has been reported to cause seizure-like activity (Steinmetz et al. 2017). GECI imaging has greatly contributed to our understanding of how networks of neurons process information and generate behavior. As technology advances, this technique continues to be refined,

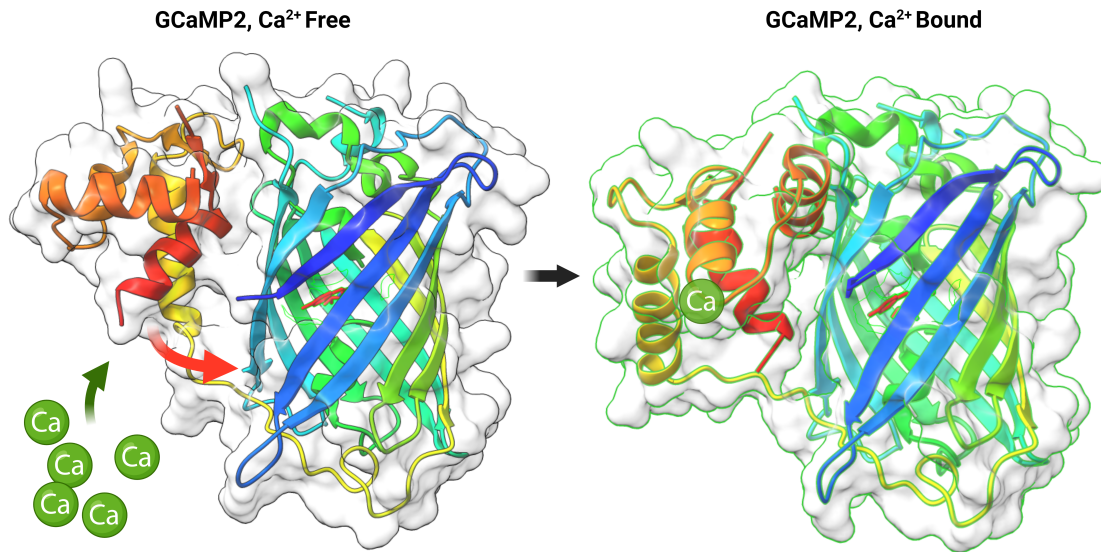


Figure 1.7: Structure of the GCaMP calcium indicator. GCaMP undergoes a conformational change in response to calcium binding that shields the chromophore located inside the beta-barrel structure, enabling its fluorescence. Partial GCaMP2 structures from PDB 3EKJ, 3EKH (Akerboom et al. 2009), morphed and rendered in ChimeraX (Goddard et al. 2018).

offering even more detailed views of neuronal activity and increasingly sophisticated means of studying the brain.

The first non-FRET GECI, G-CaMP was a seminal feat of protein engineering but displayed relatively slow kinetics, and low signal-to-noise (Nakai, Ohkura and Imoto 2001). In brief, the jellyfish gene for green fluorescent protein (GFP) was modified so that an internal chromophore was exposed to water and inactivated in the absence of Ca^{2+} ions. When Ca^{2+} binds to a calcium-binding domain that is fused to the modified GFP, a conformational change is induced, resulting in the chromophore being shielded from water, enabling its fluorescence (Figure 1.7).

Modern GECI iterations improve these properties, making them more useful for studying neuronal activity in the brain. GCaMP6s, perhaps the most widely used GECI to this day, has sufficient sensitivity to detect individual action potentials in-vivo (T.-W. Chen et al. 2013). The jGCaMP8 GECI series is a new development with a higher signal-to-noise ratio and almost ten times faster kinetics than all previous iterations of GCaMP (Yan

Zhang et al. 2023). Furthermore, strategies that do not directly involve the engineering of GECIs, such as soma targeting, have also provided significant improvements to GECI imaging (Y. Chen et al. 2020; Shemesh et al. 2020). Soma-targeting peptides restrict GECI localization to the cell body, or soma, of the neuron. When studying the activity of large populations of neurons using GECI imaging, the somata are usually the main focus of analysis. Restricting GECI localization to just the somata effectively eliminates signal from neuropil, increasing the signal-to-noise ratio and facilitating more efficient segmentation. In addition, targeting the soma can prevent the confusion of neuropil signals from unidentified cells with signals from a segmented cell's soma. Ultimately, a combination of protein engineering faster GECIs and strategies such as soma-targeting is likely to produce the optimal GECI construct.

GECIs, being genetically encoded, are typically expressed in the brain either in transgenic lines, or via delivery of a genetic payload in a virus, or by other means. In a transgenic GECI line, the GECI is typically expressed under a neuronal promoter that limits expression to CNS neurons. This provides widespread and dense labeling of neurons across the brain, allowing researchers to record neural activity from thousands of cells. However, studies have suggested that the calcium-binding of GECIs could serve as a calcium buffer, which could cause issues during development or in adults (Steinmetz et al. 2017). Furthermore, acquiring transgenic lines is expensive and time-consuming. On the other hand, achieving brain-wide GECI expression without using a transgenic line can be challenging. Intracerebral virus injections only produce GECI expression in a limited area. In Paper 3, we explore the use of an engineered adeno-associated virus (AAV) serotype that can be injected intravenously, cross the blood-brain barrier and transduce neurons across the brain (Chan et al. 2017). We combine this with a new version of a soma-targeted GECI construct that we engineered for increased expression rate, RiboL1-jGCaMP8.

Chapter 2

Objectives

The main objective of this thesis was to take advantage of genetic methods to investigate the mechanisms by which perineuronal nets may regulate neuronal function and cortical plasticity and to refine methods for imaging neural activity *in vivo*.

2.1 Paper 1

The objective of Paper 1 was to generate and characterize a specific knockout of ACAN, and thus PNNs, in Parvalbumin-positive interneurons.

- What are the effects of a PV+ ACAN KO on individual PV+ neurons and the network in which they operate relative to the effects of PNN perturbation by pan-neuronal knockouts and enzymatic digestion by Chondroitinase-ABC?

2.2 Paper 2

The objective of Paper 2 was to model the potential effects of PNN perturbation on the excitability and firing properties of the enwrapped PV+ neurons.

- If PNNs contribute to the low capacitance of PV+ neuron membranes, how would the removal of PNNs affect the electrophysiological profile of these cells?
- What other properties of PV+ neurons contribute to the electrophysiological phenotypes observed in PNN perturbation experiments?

2.3 Paper 3

The objective of Paper 3, was to improve existing genetically encoded calcium indicator (GECI) constructs to achieve more effective calcium imaging, particularly for systemic viral expression in the brain.

- The first objective of this paper was to establish the use of GECI imaging in the brain through intravenous viral transduction.
- A secondary objective was to screen and adapt soma-targeted GECI constructs.
- Ultimately, the goal is to use the methods developed in Paper 3 alongside *in vivo* PNN labeling for detailed investigations into the effects of PNNs on cortical network dynamics.

Results and Discussion

Chapter 3

Synopsis of Results

3.1 Paper 1

While the enzymatic degradation of PNNs in adult animals has shown dramatic effects on plasticity and the electrophysiological properties of PV+ neurons, it remains unclear if this is due to the lack of PNNs or the indirect effects of enzymatic treatment. The widely used enzyme chABC targets CSPGs in general, not CSPGs in PNNs specifically, and cleavage products of chABC digestion may remain in the extracellular space for months (Brückner, Bringmann et al. 1998) and affect neuronal function (Hrabětová et al. 2009; Snow et al. 1994). Here, we developed a mouse model (PVcre/ACANflox) in which ACAN is selectively knocked out in PV+ neurons. We show that PV+ neurons lacking ACAN do not produce WFA+ PNNs. Surprisingly, in the absence of WFA+ PNNs, *in vivo* electrophysiological recordings revealed similar responses of PV+ interneurons in the visual cortex (V1) of adult PV+ ACAN knockout (KO) mice and controls. WFA+ PNNs are still found on the smaller population of other neuron types that express PNNs.

Furthermore, visual cortex plasticity, studied using monocular deprivation, was unaffected in KO mice. Similarly, no changes in intrinsic electrophysiological properties were found in *in vitro* patch-clamp experiments in cortical slices from adult KO mice. However, AAV-mediated ACAN knockout in PV+ neurons of adult mice caused a shift in ocular dominance after monocular deprivation, suggesting that compensatory mechanisms might be in play in the germline KO. Intriguingly, *in vivo*, chABC treatment of KO mice resulted in a reduced firing rate of PV+ cells, and increased frequency of spontaneous excitatory postsynaptic currents (sEPSC); a phenotype associated with chABC treatment of WT animals. Furthermore, al-

though we did not find any effects on network plasticity in the visual cortex or electrophysiology; the PV+ ACAN KO mice displayed lower anxiety-like behavior than controls in standardized anxiety tests. In the Morris Water Maze task, this confidence led to an early exploratory swimming behavior where the mice quickly bumped into the submerged platform explaining the fast learning curve in this memory task.

In summary, our data could put into question the proposed role of PNNs in memory and their role in facilitating the fast-firing phenotype of PV+ interneurons, but the effects in adult aggrecan knockout animals hint at compensatory mechanisms in the germline knockout.

3.2 Paper 2

As PNNs are theorized to act as a barrier to ion transport, they may effectively increase the membrane charge-separation distance, thereby reducing membrane capacitance. Tewari et al. (2018) found that the degradation of PNNs induced a 25%-50% increase in membrane capacitance and a reduction in the firing rates of PV+ neurons. In Paper 2, we explore how changes in capacitance affect the firing rate in a selection of computational neuron models, ranging in complexity from a single-compartment Hodgkin-Huxley model to morphologically detailed PV-neuron models. In all models, increased capacitance led to reduced firing rates, but the experimentally reported increase in capacitance was insufficient to explain the experimentally reported reduction in firing rates. We, therefore, hypothesized that PNN degradation in the experiments affected not only capacitance but also other factors, such as ionic reversal potentials and ion channel conductances. In simulations, we explored how various model parameters affected the firing rate of the model neurons and identified which parameter variations, in addition to capacitance, are the most likely candidates for explaining the experimentally reported reduction in firing rate. We propose that the effect observed when PNNs are removed by chABC could be correlated not only with changes in capacitance but also with the up-regulation of potassium channel conductances and upward shifts in Ca^{2+} and Na^{+} reversal potentials.

3.3 Paper 3

Genetically encoded calcium indicators (GECI) are typically expressed in neuronal populations of transgenic mice, or via viral transduction using locally administered adeno-associated viruses (AAV). In paper 3 we explore the use of systemically administered GECIs using the recently developed PHP.eB AAV serotype to provide relatively uniform expression throughout the brain. This bypasses the need for transgenic mice with lifelong GECI expression, which has been shown to cause seizure activity. Systemic administration also avoids the issue of uneven or excessive expression associated with local injections, and no surgery is required for virus administration. The most commonly used GECIs, GCaMP6f and GCaMP6s have been used extensively with local AAV injections but are, in our hands, not sufficiently bright for use with systemic administration of PHP.eB AAVs. To identify suitable GECIs for use with systemic viral vectors, we screened 14 calcium indicators expressed under the Synapsin promoter. The majority of these did not yield reliable results, but signals from systemic administration of the recently developed jGCaMP7s, jGCaMP8s, and jGCaMP8m were sufficiently bright for *in vivo* two-photon imaging. To further improve the viability of these sensors for *in vivo* recordings, we combined the most promising jGCaMPs with recently developed soma-targeting approaches. We establish the use of soma-targeting peptides EE-RR- (soma) and RPL10a (Ribo) combined with the latest jGCaMP, jGCaMP8. We show that EE-RR-tagged jGCaMP8 gives rise to strong expression but limited soma targeting. In contrast, Ribo-tagged jGCaMP8 lacks neuropil signal, but the expression rate is reduced. To combat this, we modified the linker region of the Ribo tag (RiboL1-) and combined this with jGCaMP8. RiboL1-jGCaMP8 expresses faster than Ribo-jGCaMP8 but remains too dim for reliable use with systemic virus administration. However, intracerebral injections of RiboL1-tagged jGCaMP8 constructs provide strong Ca²⁺ signals devoid of neuropil contamination, with remarkable labeling density. In summary, we show that our soma-targeted jGCaMP8 outperforms all previously published indicator constructs regardless of the administration route, and we demonstrate that systemic injection of PHP.eB virus to express newer iterations of GECIs is a highly promising technique for imaging neural activity *in vivo*.

Chapter 4

Discussion

4.1 Perineuronal net perturbations

In this thesis, I introduce a new PNN perturbation, the specific knock-out of Aggrecan in PV+ neurons, potentially the most precise PNN perturbation to date. The PNNs are thought to play a dual role in the brain, having both restrictive properties that impede memory formation (Blacktop, Todd and Barbara A. Sorg 2017; Carulli, Broersen et al. 2020; Slaker et al. 2015), and supportive properties contributing to the stability of long-term memories (Happel et al. 2014; Rowlands et al. 2018; Thompson et al. 2018). However, in ACANflox/PVcre mice featuring a brain-wide depletion of PNNs on PV+ cells, we found that memory retrieval was comparable to controls for recent (24 hours) and remote (three weeks) memory tests in the Morris' Water Maze task (Paper 1). The knockouts displayed slightly superior training performance, but this was attributed to reduced anxiety-related behavior leading to more active exploration rather than memory improvements, as previously reported (Darcet et al. 2014; Higaki et al. 2018; Pritchett et al. 2016). Indeed, the ACANflox/PVcre mice exhibited reduced risk assessment and exploration in the open field and elevated plus maze, possibly reflecting an imbalance in excitatory and inhibitory activity during development (Sohal et al. 2009).

Notably, we found no abnormalities in the electrophysiological properties of PV+ neurons or recorded circuit activity, despite evidence from our own and others' studies finding that chondroitinase treatment typically results in changes in local field potential power and significant effects on plasticity (Lensjø, Lepperød et al. 2017; Pizzorusso, Medini, Berardi et al. 2002). Furthermore, we could not induce an ocular dominance shift in the adult ACANflox/PVcre line, even though such a shift was observed when

ACAN was knocked out in adult mice, and previously in the pan-neuronal ACAN KO (Rowlands et al. 2018.) In Paper 1, we show that eliminating aggrecan from PV+ neurons eradicates WFA+ PNNs. Accordingly, the results in Paper 1, with no effects on plasticity or the fast-firing properties of PV neurons in the germline KO of ACAN in PV+ cells, could raise concerns about interpretations of PNN studies with less specific perturbation.

Indeed, one should consider the actual ramifications of different methods for PNN perturbation or PNN knockout. It could be argued that PNN KO is the complete removal of all PNN components, although the loss of WFA reactivity alone is often considered a PNN knockout. In the case of Paper 1, aggrecan and WFA staining are eliminated, but other components, such as neurocan and tenascin-R remain. In previous studies, different PNN components have been targeted for genetic KO, including Brevican (Brakebusch et al. 2002; Favuzzi et al. 2017), pan-neuronal aggrecan (Rowlands et al. 2018), tenascin-R (Brückner, Grosche et al. 2000) and HAPLN-1 (or CTRL-1)(Carulli, Pizzorusso et al. 2010; Czipri et al. 2003; Romberg et al. 2013); but only the pan-neuronal Aggrecan KO appears to erode PNNs completely. One study targeted four PNN components for simultaneous KO: tenascin-C, tenascin-R, neurocan, and brevican (Gottschling et al. 2019), but it focuses on primary cultures derived from KO mice, and immunostaining reveals that some PNNs are still present *in vivo*.

Accordingly, one should consider if the perturbation of individual PNN components, all of which have distinct properties, probes the function of PNNs as a whole or the contribution of that particular component. Pan-neuronal Aggrecan knockout appears to completely abolish the PNNs. In contrast, in other genetic knockouts, and to some extent in chABC-treated animals, the PNNs remain partially intact, albeit with one or more components missing. In the case of digestion with chABC, chondroitin sulfate chains are lost, but the immunoreactivity of the CSPG core peptide remains for aggrecan (Matthews et al. 2002), phosphacan, and tenascin-R; while treatment with the HA cleaving hyaluronidase enzyme abolishes all PNN component immunoreactivity (Deepa et al. 2006). One should take care not to conflate the effect of a single perturbation or the function of a specific ECM component with the function of the PNN as a whole. Individual components may be responsible for many of the features we attribute to the PNN superstructure. While the conditional knockout

of aggrecan in PV+ cells that is introduced in Paper 1 eliminates WFA reactivity, this may not be the deciding factor in PNNs' contribution to plasticity regulation. Moreover, WFA+ PNNs remain intact in a smaller population of non-PV+ neurons, in contrast to the previously published pan-neuronal ACAN knockout, where all WFA+ PNNs were lost (Rowlands et al. 2018). These PNNs on non-PV+ neurons could play a significant part in PNN function that has so far been overlooked in PNN research.

Previous genetic knockouts have, unlike the PV+ aggrecan KO, produced the effects that we expected from enzymatic digestion experiments. For instance, the knock-out of Brevican produced reduced excitability that is, in several studies, associated with degradation of PNNs by chABC (Brakebusch et al. 2002; Favuzzi et al. 2017). WFA reactivity remains positive in this KO, and expression of another lectican, neurocan, is increased. In tenascin-R knockout mice (Brückner, Grosche et al. 2000), WFA reactivity is largely intact, arguably with some increase in granularity (a less reticular structure). Knockout of HAPLN1 (or CTRL1) attenuates PNNs, but some WFA reactivity remains (Carulli, Pizzorusso et al. 2010; Romberg et al. 2013), and long-term object recognition ability (24-48 h) and LTD is enhanced. These effects were also prominent, or identical, in WT animals treated with chABC, but the chABC treatment of CTRL1 KO animals did not further improve long-term object recognition or enhance LTD, indicating that the effects of a CTRL1 KO are equal to the complete removal of WFA+ PNNs by chABC.

In contrast, we found no effect on plasticity or PV+ intrinsic properties in the transgenic KO of ACAN in Paper 1, but when the same KO mice are treated with chABC, we see an apparent effect on the excitability of PV+ cells and excitatory network activity. This could indicate that aggrecan alone is not required for normal PNN-bearing PV+ cell function. However, the elimination of ACAN in PV+ cells in adult animals elevates plasticity in the visual cortex, producing an ocular dominance shift; indicating that aggrecan is in fact required for normal function. These findings suggest that some compensatory mechanism reduces the impact of aggrecan KO when it is eliminated in the germline, and one could further speculate that these compensatory mechanisms that rescue PV+ neuron function are disturbed when chABC is applied. One potential compensatory mechanism could be the up-regulation of other CSPGs in PV+ and other cell types. In Paper 1, we found that gene expression of

Neurocan and Tenascin-R is increased, and Semaphorin-3a is reduced in germline ACAN PV+ KO mice. It is also possible that non-PV+ cells could produce enough aggrecan to support a sufficient PNN structure, without being detectable over the diffuse staining of general ECM. More work is needed to understand these mechanisms, which could provide important insights into the role of PNNs and their components in the brain.

In conclusion, our findings suggest that germline knockout of ACAN in PV+ neurons effectively disrupts PNN development around these neurons, but appears to have little to no impact on memory processing or the intrinsic physiological properties of the neurons. Our results could challenge the accepted roles of PNNs and their impact on PV+ neuron function. However, the differences observed between the ACAN^{flox}/PV^{cre} mice and adult mice with acutely knocked-out ACAN in PV+ cells indicate the potential for compensatory mechanisms in the absence of PNNs from birth. As such, further research is needed to fully understand the effects of genetic PNN perturbations, and how they relate to enzymatic treatments.

4.1.1 Endogenous PNN Regulation

While artificial methods for PNN perturbation, like chABC digestion or complete genetic knockouts of PNN components, can produce loss-of-function phenotypes that could provide insights into the broad role of PNNs in the brain; it is unlikely that these all-or-nothing perturbations reflect the actual PNN dynamics, or regulation, that occurs in a normal animal. Extracellular matrix components like CSPGs have long turnover rates in the brain (Dankovich and Rizzoli 2022; Fornasiero et al. 2018; R. K. Margolis, Preti et al. 1975; Roger Y. Tsien 2013), and there would be a significant delay in changes to extracellular levels of Aggrecan or other lecticans in response to genetic up- or down-regulation. This time scale may not be relevant for behavior-induced effects on plasticity.

Furthermore, several secreted metalloproteases are known to digest PNN components, including MMP-9 and several members of the ADAMTS family. These proteases could act on PNNs at time scales more relevant to brain activity patterns and plasticity mechanisms. And, their expression and secretion could be strictly regulated by either post or pre-synaptic neurons, and, importantly, their activity may be regulated by PNN modifying enzymes, which may enhance protease efficiency (Shinji

Miyata and Kitagawa 2016). Secretion of proteases could serve as a precise method for regulating plasticity at the level of individual synapses rather than at all synapses on the neuron. A post-synaptic cell could, for instance, increase the rate of 6-sulfation of PNN chondroitin-sulfate chains, rendering the PNNs less resistant to protease digestion. A pre-synaptic cell could then increase protease secretion to digest PNNs, to form a synapse, or increase the surface area of an existing synapse. Or, in a different scenario, a pre-synaptic cell could reduce the secretion of TIMP-3, an inhibitor of metalloproteases, while the post-synaptic cell could increase the production of MMP-9 or other proteases to regulate the pericellular environment. MMP-9 has previously been shown to be required for LTP maintenance (Bozdagi et al. 2007), and one study found that MMP-9 mRNA is transported to dendrites and translated locally in dendrites in response to activity (Dziembowska et al. 2012). However, another study found that PV+ neurons in the cerebral cortex primarily express the proteases ADAMTS8, ADAMTS15, and Mmp, not MMP9 (Levy et al. 2015; Rossier et al. 2015).

While these proteases appear to be enriched in PV+ cells, a wide variety of metalloproteases in the brain may regulate PNNs via expression in different types of neurons or glial cells. The various metalloproteases that cleave lecticans have different specificities (and products): Aggrecan appears to mainly be cleaved by ADAMTS-4 and ADAMTS-5 (Verma and Dalal 2011; Westling et al. 2002), but also, to some extent, by ADAMTS-8, 15 and 1 (Collins-Racie et al. 2004; Kelwick et al. 2015; Kuno et al. 2000). Versican is cleaved by ADAMTS-1, 4, 5, 9, and 20 (Stanton et al. 2011). Brevican is cleaved by ADAMTS-1, 4 and 5 (Nakada et al. 2005; Yuan et al. 2002), whereas Neurocan appears to only be cleaved by ADAMTS-12 and ADAMTS-4 (Cua et al. 2013; Fontanil et al. 2019). Notably, several studies have found that the application of ADAMTS-4 in the brain and in cell cultures can efficiently digest PNNs (Benbenishty et al. 2023; Cua et al. 2013). And yet, the bacterial enzyme chABC remains the default method for acute PNN disruption.

In summary, these proteases, which are differentially expressed in the brain, present a toolbox for highly precise modification of PNNs, and their specific roles in neuroplasticity should be investigated further, as should their potential experimental use in plasticity modulation via selective over-expression or knock-out in various cell types.

4.2 Modeling Consequences of PNN Perturbations

The idea that the bulk structure of PNNs contributes to the capacitance of a neuron's membrane is intuitive. PNNs form a sheath on the membrane that may increase the thickness of the membrane, effectively reducing capacitance, and allowing the membrane to charge faster, thus facilitating faster firing. This was the proposed mechanism behind the effect seen both on peritumoral PNNs and PNNs treated with chABC in Tewari et al. (2018). Their chABC experiments were also some of the most rigorous to date. They were able to measure electrophysiological properties by patch clamp before and after chABC treatment in the same cell, avoiding the large variability seen in cortical PV+ cells. Although, their findings were not reproduced in a limited sample size in Paper 1 Fig. S1, where we observed a general decrease in capacitance over time in both control and chABC-treated cells. Yet, these are intricate experiments where cells must be perfused with an unusually small volume of ACSF (with chABC), as the concentration of chABC needed for rapid digestion (50 min) of PNN is as high as 10U / ml, making the experiments prohibitively costly, even in small volumes (up to 1000\$ per cell, 10ml volume). The low volume also increases the risk of evaporation, affecting ion concentrations and osmolarity, which could cause cells to shrink and in turn, cause a reduction of capacitance. Potential changes in cell size are not accounted for in these experiments, which could occur if, for example, the chABC solution has an osmolarity different from that of the regular recording solution.

We applied more detailed multicompartment models to test the idea that PNNs allow PV+ cells to fire at high frequencies through reduced membrane capacitance. Multicompartment models are more relevant than the Hodgkin-Huxley model used in Tewari 2018. Our simulations revealed that even a 50% change in capacitance would not cause large enough effects to explain the large change in firing frequency reported in their study. Accordingly, we set out to model the effects of other changes associated with PNN perturbation from the literature, such as the effect of altered potassium channel conductance, as a reduction in Kv3.1b and Kv1.1 channel clustering was found in a Brevican KO (Favuzzi et al. 2017). Here, we found that changing Kv3 conductance primarily affected the firing threshold, in contrast to the mild effects on the firing threshold

found in Tewari 2018. Ultimately, we find that a combination of several factors, including the capacitance, must be significantly changed to affect the firing rate to a similar extent as seen in Tewari et al. 2018 and other studies on PNN perturbation. Combined changes to E_{Na} , E_{Ca} , and the conductances of SK and KV2like produce large shifts in firing frequency, without altering the firing threshold. The extensive changes required, like shifting E_{Ca} and E_{Na} by 30 and 10 mV, respectively, indicate just how dramatic the effects of chABC (and tumoral protease secretion) must be to elicit such a drastic effect on firing rates in PV+ neurons. In summary, the models applied in Paper 2 provide insights into how PNNs affect the fast-firing phenotype of PV+ cells, which may then be probed experimentally; and provides an example of how computational models can supplement experimental work to investigate the consequences of PNN perturbation.

4.3 Imaging of neuronal activity

The introduction of engineered adeno-associated virus (AAV) serotypes that exhibit high affinity for the central nervous system and can be delivered intravenously has presented a minimally invasive and cost-effective method of introducing genetic payloads into the brain (Chan et al. 2017). Notably, these new serotypes, particularly PHP.eB, have not been extensively utilized for the delivery of genetically encoded calcium indicators (GECIs), despite their clear advantages in terms of animal welfare, cost efficiency, productivity, and experimental flexibility. Past research has demonstrated that wide-field imaging with systemically administered GCaMP6f, a widely used GECI, is feasible with promoters other than synapsin (Allen et al. 2017; Michelson, Vanni and Murphy 2019). However, our preliminary experiments revealed that GCaMP6f was not sufficiently bright for compatibility with systemic administration for two-photon imaging. Such a reduction in brightness with systemic administration is anticipated due to a lower multiplicity of infection as compared to an intracerebral injection, i.e., each cell is transduced by fewer viral particles.

In response to these observations, we screened 14 GECIs, revealing that newer iterations of jGCaMPs, specifically jGCaMP7s, jGCaMP8s, and jGCaMP8m, were adequately bright for two-photon *in vivo* Ca²⁺ imaging following systemic administration in PHP.eB AAVs.

Intravenous AAV injections in the retro-orbital sinus can be carried out rapidly, demand minimal training, and are significantly less invasive than stereotaxic or intracerebral injections. Moreover, this intravenous injection yields largely consistent expression throughout the mouse brain, remaining stable over extended durations. In contrast, intracerebral virus injections may result in excessive expression leading to unhealthy cells or cell death.

While intravenous administration of viruses for GECI delivery holds many advantages, it requires a large virus dose per animal, which could be prohibitively expensive if all viruses are procured from commercial vendors. However, if viruses are produced in-house or by a local virus core, scaling up production to suitable levels is relatively inexpensive.

We identified a clear bias in the expression for cortical layer 5, striatum, CA2, and subiculum regions with the PHP.eB and AAV9 serotype AAVs. Although the bias towards cortical layer 5 could be attributed to the large cell volumes and higher capacity for transgene production, this does not appear to be a common feature for the preferred brain areas. If the mechanisms behind these expression differences are understood and reduced in future versions of synthetic AAV serotypes, fewer virus copies may be required for sufficient expression.

Concerning the high brightness required for the GECI with systemic administration, we noted substantial neuropil contamination of the signals. We countered this by using two soma-targeting strategies to restrict expression to cell somata, showing that EE-RR soma-targeting resulted in stable expression visible after two weeks while ribosome-tethering reduced brightness to an extent that cells were not observable until 4–6 weeks post-injection. To address this issue, we introduced a modified version of the construct where we modified the linker region, termed RiboL1-jGCaMP8. This adjustment resulted in significant improvements, allowing us to commence imaging as soon as one week after intracerebral virus injection. Remarkably, this method exhibited no apparent drawbacks such as overexpression over extended periods.

Broadly, ribosome-tethered GECI expression improves the signal-to-noise ratio and permits the detection of activity from a larger number of cells, as their activity is no longer obscured by neuropil activity. Further, we observed that the process of automatic cell detection in Suite2p was more accurate and required smaller data sets from recordings made with

the ribosome-tethered GECIs.

In summary, we have developed a suite of viral vectors for both systemic and intracerebral administration that demonstrate high performance and sustained expression over extended periods. We believe these GECI constructs hold promise for replacing, or supplementing, transgenic animal models for GECI expression. Our results show that jGCaMP8 and EE-RR-jGCaMP8 are highly suitable for systemic delivery, exhibiting brain-wide expression within two weeks that remains stable over months. Finally, the ribosome-tethered jGCaMP8 offers unprecedented labeling density and signal-to-noise ratio, proving highly suitable for intracerebral virus injections.

4.3.1 PNNs and Calcium Imaging

The effects of PNN perturbation have mainly been measured by electrophysiology, either *in vivo* or *in vitro*. PNN perturbation could also be studied optically using calcium imaging, but *in vivo* labeling of PNNs has proved challenging, limiting the use of optical studies as PNN-bearing cells could not be distinguished. A recent paper reports on a method for *in vivo* labeling of PNNs using intracerebrally injected, fluorescently labeled WFA, and combines this with calcium imaging using the GECI GCaMP6f (Benbenishty et al. 2023). They show that *in vivo* labeling is stable over multiple weeks and does not appear to interfere with protease (ADAMTS-4) or chABC activity. Alternatively, PNNs could be labeled by genetic methods, such as knock-in of fluorescent proteins on PNN components, or over-expression of PNN components bearing fluorescent protein tags (Calugi et al. 2022). Although, one should consider, and control for, potential effects that over-expression of PNN components may have on PNN function. Both options offer exciting opportunities for studying the effects of PNN perturbation, or the differences between PNN+ and PNN- PV+ neurons in cortical circuits. The latter option could also be applied to brain-wide labeling of PNNs, using PHP.eB viruses and intravenous virus injections, as we did for GECIs in paper 3.

In Paper 3, we developed soma-targeted GECI constructs that achieve remarkable labeling density and signal-to-noise (Figure 4.8). Combined with genetic or WFA-based PNN labeling, these viral constructs open the door for detailed interrogation of PNN+ and PNN- PV+ cells *in vivo*, and the

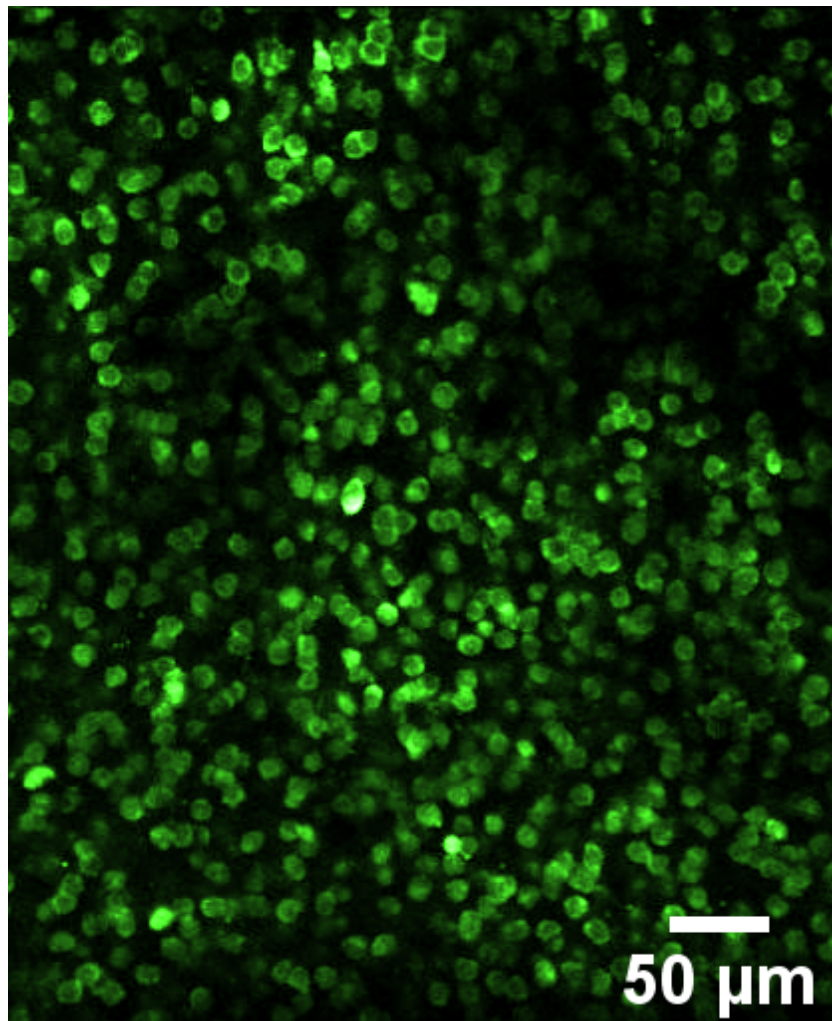


Figure 4.8: *In vivo* calcium imaging using RiboL1-jGCaMP8s in primary visual cortex (V1).

networks they operate in.

4.4 PNNs and the Engram

In this thesis, I chose to focus mainly on the role of PNNs in synaptic plasticity, rather than the role of PNNs in memory or engrams specifically. However, much of the recent interest in PNNs can be attributed to the hypotheses put forth by the late Nobel Laureate Roger Tsien in 2013, where he suggested that the holes in PNNs could be the physical substrate of memories (Roger Y. Tsien 2013). This is an appealing idea; perineuronal net maturation coincides with dampened plasticity at the end of the critical period, and perturbation of PNNs appears to restore plasticity to

critical period levels. The holes in PNNs are indeed filled by synapses, and they appear to be highly stable structures (Benbenishty et al. 2023; Dankovich and Rizzoli 2022). Perineuronal net perturbation does not appear to simply erase existing memories but allows for the overwriting of existing memories (Gogolla et al. 2009). Still, we cannot say if this is due to the impaired stability of distinct engrams or changes in parvalbumin interneuron excitability and the downstream effects of this on neuronal networks. Thompson et al. found that removal of PNNs in the secondary visual cortex impaired recall of a remote fear memory (Thompson et al. 2018). This seemed associated with an impaired synchronization of activity between the secondary visual cortex and amygdala. Moreover, Christensen et al., 2021, found an impaired temporal coherency in the firing activity between grid cells after chABC treatment in the medial entorhinal cortex (Christensen et al. 2021). Both these investigations point to chABC treatment affecting the preciseness in PV+ neuron network activity. To my knowledge, no studies of PNN perturbation's effect on distinct engrams have been conducted. These are highly challenging experiments, ideally performed in-vivo, that would require consistent monitoring of engram cells over extended time via holographic 2-photon imaging, along with PNN labeling and perturbation.

While I focused mainly on canonical synaptic plasticity in this thesis, one form of plasticity that could be relevant to PNN function that is not often mentioned explicitly is synaptic rewiring. What is typically discussed under the term synaptic plasticity are Hebbian mechanisms, LTP and LTD, and homeostatic mechanisms. Synaptic rewiring is the formation of new synapses, or elimination of existing synapses, which also occurs in the adult brain (Chklovskii, Mel and K. Svoboda 2004). In addition, silent synapses could be activated, effectively producing new connections without forming a completely new synapse. Silenced synapses only contain NMDA receptors and do not contribute to the excitation state of the post-synaptic cell. Recent research suggests that silent synapses are abundant in the adult brain and can be activated by Hebbian stimulation protocols, i.e., timed stimulation of pre-synaptic neurotransmitter release and action potential stimulation in the post-synaptic cell (Vardalaki, Chung and Harnett 2022). Perhaps the role of PNNs is to restrict the formation or re-activation of synapses, ultimately affecting the connectivity pattern of neuronal networks. This may provide

additional memory storage capabilities in addition to that provided by strengthening and weakening of existing, active synapses (Chklovskii, Mel and K. Svoboda 2004). It has been demonstrated that the proportion of excitatory to inhibitory synapses on PV+ neurons changes after PNN perturbation, suggesting that some rewiring occurs when PNNs are perturbed (Donato, Rompani and Caroni 2013; Favuzzi et al. 2017; Lensjø, Christensen et al. 2017; Pyka et al. 2011).

Along with engram monitoring and PNN labeling, an in-vivo investigation of whether PNN perturbation could influence the stimulus-driven activation of silent synapses or even instigate the formation of entirely new synapses in adult animals would be immensely interesting.

4.5 Conclusion and Outlook

The plasticity of the brain, its ability to change, remains active throughout life, and is especially pronounced during early post-natal development in critical periods. A condensed extracellular matrix structure, the perineuronal net, that completes at the end of the critical period, appears to tightly regulate plasticity in the adult brain. As noted in the background chapter, our definition of perineuronal nets (PNNs) is somewhat imprecise, relying largely on the reactivity of Wisteria Floribunda Agglutinin (WFA) lectin. This uncertainty also extends to our definition of various PNN perturbations that target individual, a set of, or all components of the PNNs and the broader brain extracellular matrix (ECM).

In Paper 1, I presented a perturbation method designed to completely dismantle PNNs, yet this did not inhibit normal plasticity or the function of parvalbumin-positive (PV+) neurons. This raises questions about the interpretation of previous, less precise PNN perturbations. However, despite the loss of WFA and aggrecan antibody reactivity, other PNN components persisted and the expression of some components was increased. This could indicate that compensatory mechanisms are initiated when aggrecan is lost in the germline, preserving normal brain function.

Indeed, when we induced the knockout in adult mice using adeno-associated viruses (AAVs) expressing PV-specific Cre in aggrecan-floxed mice, we observed an ocular dominance shift, indicative of increased plas-

ticity. Furthermore, while the germline knockout had no discernible effect on intrinsic electrophysiological properties, treatment of the adult germline knockout with chondroitinase ABC (chABC) resulted in a phenotype consistent with the chABC treatment of wild-type animals. This could suggest that the presumed compensatory mechanism, possibly related to ECM component expression, is disrupted by chABC treatment.

In light of these findings, there is a pressing need to develop experimental methodologies that leverage our understanding of extracellular proteases targeting PNN components, to enable more accurate PNN perturbation. We are currently investigating this through an intersectional approach utilizing both CRISPR knockout and CRISPR activation for simultaneous control of multiple PNN regulator genes, such as proteases and sulfotransferases.

The ECM, and perhaps particularly the PNNs distinctly influence brain plasticity and the excitability of parvalbumin-positive (PV+) neurons. However, the exact mechanisms through which these effects are facilitated remain elusive. PNNs might act to stabilize synapses over the long term, thereby securing engram circuits to preserve memory. Alternatively, the bulk structure of PNNs could function as an added dielectric plate in the plasma membrane capacitor, effectively lowering capacitance to facilitate fast-firing properties and high excitability. In paper 2, we put this hypothesis to the test using advanced computational models. We found that reduced capacitance can facilitate fast-firing rates, but capacitance alone cannot explain the reduction in firing rates found in PNN perturbation experiments. Additional effects on ion channel conductance and equilibrium potentials are needed to explain the drastic effects on firing rates reported in experiments. While these findings illuminate one facet of PNN functionality, numerous questions persist that could be explored using computational models; such as the network effects of PNN perturbation. However, to facilitate the modeling of PNN perturbation effects, we must first understand the actual outcomes of PNN perturbations, which may vary depending on the specific type of perturbation applied.

As we strive to comprehend the intricate operations of the brain, the capacity to monitor individual neuronal activity is indispensable. Calcium imaging using genetically encoded calcium sensors allows researchers to measure the activity of selected populations of neurons over extended

time periods. This methodology has predominantly relied on transgenic mice, especially for whole-brain calcium imaging. In Paper 3, we leverage an engineered AAV serotype to deliver GECI to the whole brain. Furthermore, we enhance existing GECI constructs by engineering an optimal soma-targeting construct for accelerated expression rate. This results in GECI constructs that surpass all presently available constructs for in vivo calcium imaging.

Since the completion of Paper 3, new GECIs that report higher SNR and faster kinetics have been reported (Li et al. 2023; Wait et al. 2023), but they did not apply soma-targeting. In pursuit of the ultimate GECI construct, we are currently experimenting with soma-targeted versions of these new GECIs - and we are confident that the future is bright, and targeted to the soma.

Bibliography

- Akerboom, Jasper et al. (6th Mar. 2009). ‘Crystal Structures of the GCaMP Calcium Sensor Reveal the Mechanism of Fluorescence Signal Change and Aid Rational Design*’. In: *Journal of Biological Chemistry* 284.10, pp. 6455–6464. ISSN: 0021-9258. DOI: 10.1074/jbc.M807657200. URL: <https://www.sciencedirect.com/science/article/pii/S0021925820326739> (visited on 30/06/2023).
- Alcántara, S., I. Ferrer and E. Soriano (1st July 1993). ‘Postnatal development of parvalbumin and calbindin D28K immunoreactivities in the cerebral cortex of the rat’. In: *Anatomy and Embryology* 188.1, pp. 63–73. ISSN: 1432-0568. DOI: 10.1007/BF00191452. URL: <https://doi.org/10.1007/BF00191452> (visited on 28/06/2023).
- Allen, William E. et al. (17th May 2017). ‘Global Representations of Goal-Directed Behavior in Distinct Cell Types of Mouse Neocortex’. In: *Neuron* 94.4, 891–907.e6. ISSN: 0896-6273. DOI: 10.1016/j.neuron.2017.04.017. URL: <https://www.sciencedirect.com/science/article/pii/S0896627317303434> (visited on 03/07/2023).
- Alzheimer, A. et al. (1995). ‘An English translation of Alzheimer’s 1907 paper, "Über eine eigenartige Erkrankung der Hirnrinde"’. In: *Clinical Anatomy (New York, N.Y.)* 8.6, pp. 429–431. ISSN: 0897-3806. DOI: 10.1002/ca.980080612.
- Antonini, Antonella, Michela Fagiolini and Michael P. Stryker (1st June 1999). ‘Anatomical Correlates of Functional Plasticity in Mouse Visual Cortex’. In: *Journal of Neuroscience* 19.11. Publisher: Society for Neuroscience Section: ARTICLE, pp. 4388–4406. ISSN: 0270-6474, 1529-2401. DOI: 10.1523/JNEUROSCI.19-11-04388.1999. URL: <https://www.jneurosci.org/content/19/11/4388> (visited on 28/06/2023).
- Antonini, Antonella and Michael P. Stryker (1996). ‘Plasticity of geniculocortical afferents following brief or prolonged monocular occlusion in the cat’. In: *Journal of Comparative Neurology* 369.1, pp. 64–82. ISSN: 1096-9861. DOI: 10.1002/(SICI)1096-9861(19960520)369:1<64::AID-

- CNE5>3.0.CO;2-I. URL: <https://onlinelibrary.wiley.com/doi/abs/10.1002/%28SICI%291096-9861%2819960520%29369%3A1%3C64%3A%3AAID-CNE5%3E3.0.CO%3B2-I> (visited on 29/06/2023).
- Baig, Shabnam, Gordon K. Wilcock and Seth Love (Oct. 2005). 'Loss of perineuronal net N-acetylgalactosamine in Alzheimer's disease'. In: *Acta Neuropathologica* 110.4, pp. 393–401. ISSN: 0001-6322. DOI: 10.1007/s00401-005-1060-2.
- Balmer, Timothy S. (1st Jan. 2016). 'Perineuronal Nets Enhance the Excitability of Fast-Spiking Neurons'. In: *eNeuro* 3.4. Publisher: Society for Neuroscience, pp. 745–751. ISSN: 23732822. DOI: 10.1523/ENEURO.0112-16.2016. URL: </pmc/articles/PMC4987413/> (visited on 09/06/2023).
- Benbenishty, Amit et al. (Jan. 2023). 'Longitudinal in vivo imaging of perineuronal nets'. In: *Neurophotonics* 10.1, p. 015008. ISSN: 2329-423X. DOI: 10.1117/1.NPh.10.1.015008. URL: <https://www.ncbi.nlm.nih.gov/pmc/articles/PMC10037344/> (visited on 19/06/2023).
- Berchtold, N. C. and C. W. Cotman (1st May 1998). 'Evolution in the Conceptualization of Dementia and Alzheimer's Disease: Greco-Roman Period to the 1960s'. In: *Neurobiology of Aging* 19.3, pp. 173–189. ISSN: 0197-4580. DOI: 10.1016/S0197-4580(98)00052-9. URL: <https://www.sciencedirect.com/science/article/pii/S0197458098000529> (visited on 26/06/2023).
- Berretta, Sabina et al. (1st Sept. 2015). 'Losing the sugar coating: Potential impact of perineuronal net abnormalities on interneurons in schizophrenia'. In: *Schizophrenia Research. The GABA System in Schizophrenia: Cells, Molecules and Microcircuitry* 167.1, pp. 18–27. ISSN: 0920-9964. DOI: 10.1016/j.schres.2014.12.040. URL: <https://www.sciencedirect.com/science/article/pii/S092099641500002X> (visited on 26/06/2023).
- Bittner, Katie C. et al. (8th Sept. 2017). 'Behavioral time scale synaptic plasticity underlies CA1 place fields'. In: *Science* 357.6355. Publisher: American Association for the Advancement of Science, pp. 1033–1036. DOI: 10.1126/science.aan3846. URL: <https://www.science.org/doi/full/10.1126/science.aan3846> (visited on 16/06/2023).
- Blacktop, Jordan M., Ryan P. Todd and Barbara A. Sorg (May 2017). 'Role of perineuronal nets in the anterior dorsal lateral hypothalamic area in the acquisition of cocaine-induced conditioned place preference and self-administration'. In: *Neuropharmacology* 118. Publisher:

- Neuropharmacology, pp. 124–136. ISSN: 1873-7064. DOI: 10.1016/J.NEUROPHARM.2017.03.018.
- Bozdagi, Ozlem et al. (July 2007). ‘In Vivo Roles for Matrix Metalloproteinase 9 in Mature Hippocampal Synaptic Physiology and Plasticity’. In: *Journal of Neurophysiology* 98.1. Publisher: American Physiological Society, pp. 334–344. ISSN: 0022-3077. DOI: 10.1152/jn.00202.2007. URL: <https://journals.physiology.org/doi/full/10.1152/jn.00202.2007> (visited on 17/06/2023).
- Brakebusch, Cord et al. (Nov. 2002). ‘Brevican-deficient mice display impaired hippocampal CA1 long-term potentiation but show no obvious deficits in learning and memory’. In: *Molecular and Cellular Biology* 22.21, pp. 7417–7427. ISSN: 0270-7306. DOI: 10.1128/MCB.22.21.7417-7427.2002.
- Brückner, G., Andreas Bringmann et al. (1st Aug. 1998). ‘Acute and long-lasting changes in extracellular-matrix chondroitin-sulphate proteoglycans induced by injection of chondroitinase ABC in the adult rat brain’. In: *Experimental Brain Research* 121.3, pp. 300–310. ISSN: 1432-1106. DOI: 10.1007/s002210050463. URL: <https://doi.org/10.1007/s002210050463> (visited on 23/06/2023).
- Brückner, G., J. Grosche et al. (25th Dec. 2000). ‘Postnatal development of perineuronal nets in wild-type mice and in a mutant deficient in tenascin-R’. In: *The Journal of Comparative Neurology* 428.4, pp. 616–629. ISSN: 0021-9967. DOI: 10.1002/1096-9861(20001225)428:4<616::aid-cne3>3.0.co;2-k.
- Cabungcal, Jan-Harry et al. (28th May 2013). ‘Perineuronal nets protect fast-spiking interneurons against oxidative stress’. In: *Proceedings of the National Academy of Sciences* 110.22. Publisher: Proceedings of the National Academy of Sciences, pp. 9130–9135. DOI: 10.1073/pnas.1300454110. URL: <https://www.pnas.org/doi/full/10.1073/pnas.1300454110> (visited on 24/06/2023).
- Caillard, Olivier et al. (21st Nov. 2000). ‘Role of the calcium-binding protein parvalbumin in short-term synaptic plasticity’. In: *Proceedings of the National Academy of Sciences* 97.24. Publisher: Proceedings of the National Academy of Sciences, pp. 13372–13377. DOI: 10.1073/pnas.230362997. URL: <https://www.pnas.org/doi/full/10.1073/pnas.230362997> (visited on 13/06/2023).

- Calugi et al. (14th Nov. 2022). *Visualization of perineuronal nets for in vivo imaging applications*. URL: <https://www.abstractsonline.com/pp8/#!/10619/presentation/75210> (visited on 19/06/2023).
- Cardin, Jessica A. et al. (4th June 2009). 'Driving fast-spiking cells induces gamma rhythm and controls sensory responses'. In: *Nature* 459.7247, pp. 663–667. ISSN: 1476-4687. DOI: 10.1038/nature08002.
- Carstens, Kelly E et al. (2016). 'Perineuronal Nets Suppress Plasticity of Excitatory Synapses on CA2 Pyramidal Neurons.' In: *The Journal of neuroscience : the official journal of the Society for Neuroscience* 36.23. Publisher: Society for Neuroscience, pp. 6312–20. ISSN: 1529-2401. DOI: 10.1523/JNEUROSCI.0245-16.2016.
- Carulli, Daniela, Robin Broersen et al. (Mar. 2020). 'Cerebellar plasticity and associative memories are controlled by perineuronal nets'. In: *Proceedings of the National Academy of Sciences of the United States of America* 117.12. Publisher: National Academy of Sciences, pp. 6855–6865. ISSN: 10916490. DOI: 10.1073/PNAS.1916163117/-DCSUPPLEMENTAL.
- Carulli, Daniela, Tommaso Pizzorusso et al. (Aug. 2010). 'Animals lacking link protein have attenuated perineuronal nets and persistent plasticity'. In: *Brain: A Journal of Neurology* 133 (Pt 8), pp. 2331–2347. ISSN: 1460-2156. DOI: 10.1093/brain/awq145.
- Chan, Ken Y et al. (Aug. 2017). 'Engineered AAVs for efficient noninvasive gene delivery to the central and peripheral nervous systems'. In: *Nature neuroscience* 20.8, pp. 1172–1179. ISSN: 1097-6256. DOI: 10.1038/nn.4593. URL: <https://www.ncbi.nlm.nih.gov/pmc/articles/PMC5529245/> (visited on 28/06/2023).
- Chen, Tsai-Wen et al. (18th July 2013). 'Ultra-sensitive fluorescent proteins for imaging neuronal activity'. In: *Nature* 499.7458, pp. 295–300. ISSN: 0028-0836. DOI: 10.1038/nature12354. URL: <https://www.ncbi.nlm.nih.gov/pmc/articles/PMC3777791/> (visited on 14/06/2023).
- Chen, Yiming et al. (5th Aug. 2020). 'Soma-Targeted Imaging of Neural Circuits by Ribosome Tethering'. In: *Neuron* 107.3, 454–469.e6. ISSN: 0896-6273. DOI: 10.1016/j.neuron.2020.05.005. URL: <https://www.sciencedirect.com/science/article/pii/S0896627320303512> (visited on 25/06/2023).
- Chklovskii, D. B., B. W. Mel and K. Svoboda (Oct. 2004). 'Cortical rewiring and information storage'. In: *Nature* 431.7010. Number: 7010 Publisher:

- Nature Publishing Group, pp. 782–788. ISSN: 1476-4687. DOI: 10.1038/nature03012. URL: <https://www.nature.com/articles/nature03012> (visited on 25/06/2023).
- Christensen, Ane Charlotte et al. (11th Jan. 2021). ‘Perineuronal nets stabilize the grid cell network’. In: *Nature Communications* 12.1. Number: 1 Publisher: Nature Publishing Group, p. 253. ISSN: 2041-1723. DOI: 10.1038/s41467-020-20241-w. URL: <https://www.nature.com/articles/s41467-020-20241-w> (visited on 03/07/2023).
- Chu, Philip et al. (2018). ‘The Impact of Perineuronal Net Digestion Using Chondroitinase ABC on the Intrinsic Physiology of Cortical Neurons HHS Public Access’. In: *Neuroscience* 388, pp. 23–35. DOI: 10.1016/j.neuroscience.2018.07.004. (Visited on 09/06/2023).
- Collins-Racie, Lisa A. et al. (July 2004). ‘ADAMTS-8 exhibits aggrecanase activity and is expressed in human articular cartilage’. In: *Matrix Biology: Journal of the International Society for Matrix Biology* 23.4, pp. 219–230. ISSN: 0945-053X. DOI: 10.1016/j.matbio.2004.05.004.
- Crair, Michael C. and Robert C. Malenka (May 1995). ‘A critical period for long-term potentiation at thalamocortical synapses’. In: *Nature* 375.6529. Number: 6529 Publisher: Nature Publishing Group, pp. 325–328. ISSN: 1476-4687. DOI: 10.1038/375325a0. URL: <https://www.nature.com/articles/375325a0> (visited on 28/06/2023).
- Cua, Rowena C. et al. (June 2013). ‘Overcoming neurite inhibitory chondroitin sulfate proteoglycans in the astrocyte matrix’. In: *Glia* 61.6, pp. 972–984. ISSN: 1098-1136. DOI: 10.1002/glia.22489.
- Czipri, Mátyás et al. (3rd Oct. 2003). ‘Genetic rescue of chondrodysplasia and the perinatal lethal effect of cartilage link protein deficiency’. In: *The Journal of Biological Chemistry* 278.40, pp. 39214–39223. ISSN: 0021-9258. DOI: 10.1074/jbc.M303329200.
- Dankovich, Tal M. and Silvio O. Rizzoli (8th Mar. 2022). ‘The Synaptic Extracellular Matrix: Long-Lived, Stable, and Still Remarkably Dynamic’. In: *Frontiers in Synaptic Neuroscience* 14, p. 854956. ISSN: 1663-3563. DOI: 10.3389/fnsyn.2022.854956. URL: <https://www.ncbi.nlm.nih.gov/pmc/articles/PMC8957932/> (visited on 03/07/2023).
- Darcet, Flavie et al. (May 2014). ‘Learning and memory impairments in a neuroendocrine mouse model of anxiety/depression’. In: *Frontiers in Behavioral Neuroscience* 8 (MAY). Publisher: Frontiers Research Foundation. ISSN: 16625153. DOI: 10.3389/fnbeh.2014.00136.

- Deepa, Sarama Sathyaseelan et al. (June 2006). 'Composition of perineuronal net extracellular matrix in rat brain: a different disaccharide composition for the net-associated proteoglycans.' In: *The Journal of biological chemistry* 281.26, pp. 17789–800. ISSN: 0021-9258. DOI: 10.1074/jbc.M600544200.
- Dityatev, Alexander et al. (Apr. 2007). 'Activity-dependent formation and functions of chondroitin sulfate-rich extracellular matrix of perineuronal nets.' In: *Developmental neurobiology* 67.5, pp. 570–88. ISSN: 1932-8451. DOI: 10.1002/dneu.20361.
- Donato, Flavio, Santiago Belluco Rompani and Pico Caroni (Dec. 2013). 'Parvalbumin-expressing basket-cell network plasticity induced by experience regulates adult learning'. In: *Nature* 504.7479. Number: 7479 Publisher: Nature Publishing Group, pp. 272–276. ISSN: 1476-4687. DOI: 10.1038/nature12866. URL: <https://www.nature.com/articles/nature12866> (visited on 13/06/2023).
- Dräger, U. C. (Jan. 1978). 'Observations on monocular deprivation in mice'. In: *Journal of Neurophysiology* 41.1, pp. 28–42. ISSN: 0022-3077. DOI: 10.1152/jn.1978.41.1.28.
- Dziembowska, Magdalena et al. (17th Oct. 2012). 'Activity-dependent local translation of matrix metalloproteinase-9'. In: *The Journal of Neuroscience: The Official Journal of the Society for Neuroscience* 32.42, pp. 14538–14547. ISSN: 1529-2401. DOI: 10.1523/JNEUROSCI.6028-11.2012.
- Eggermann, Emmanuel and Peter Jonas (Jan. 2012). 'How the 'slow' Ca²⁺ buffer parvalbumin affects transmitter release in nanodomain-coupling regimes'. In: *Nature Neuroscience* 15.1. Number: 1 Publisher: Nature Publishing Group, pp. 20–22. ISSN: 1546-1726. DOI: 10.1038/nn.3002. URL: <https://www.nature.com/articles/nn.3002> (visited on 13/06/2023).
- Elbert, T. et al. (13th Oct. 1995). 'Increased cortical representation of the fingers of the left hand in string players'. In: *Science (New York, N.Y.)* 270.5234, pp. 305–307. ISSN: 0036-8075. DOI: 10.1126/science.270.5234.305.
- Enwright, John F. et al. (Aug. 2016). 'Reduced Labeling of Parvalbumin Neurons and Perineuronal Nets in the Dorsolateral Prefrontal Cortex of Subjects with Schizophrenia'. In: *Neuropsychopharmacology* 41.9. Number: 9 Publisher: Nature Publishing Group, pp. 2206–2214. ISSN:

- 1740-634X. DOI: 10.1038/npp.2016.24. URL: <https://www.nature.com/articles/npp201624> (visited on 24/06/2023).
- Faini, Giulia et al. (Dec. 2018). 'Perineuronal nets control visual input via thalamic recruitment of cortical PV interneurons'. In: *eLife* 7. Publisher: eLife Sciences Publications Ltd. ISSN: 2050084X. DOI: 10.7554/eLife.41520.
- Favuzzi, Emilia et al. (Aug. 2017). 'Activity-Dependent Gating of Parvalbumin Interneuron Function by the Perineuronal Net Protein Brevican'. In: *Neuron* 95.3. Publisher: Cell Press, 639–655.e10. ISSN: 0896-6273. DOI: 10.1016/j.NEURON.2017.06.028.
- Fawcett, James W., Toshitaka Oohashi and Tommaso Pizzorusso (Aug. 2019). 'The roles of perineuronal nets and the perinodal extracellular matrix in neuronal function'. In: *Nature Reviews. Neuroscience* 20.8, pp. 451–465. ISSN: 1471-0048. DOI: 10.1038/s41583-019-0196-3.
- Fontanil, Tania et al. (2019). 'Neurocan is a New Substrate for the ADAMTS12 Metalloprotease: Potential Implications in Neuropathies'. In: *Cellular Physiology and Biochemistry: International Journal of Experimental Cellular Physiology, Biochemistry, and Pharmacology* 52.5, pp. 1003–1016. ISSN: 1421-9778. DOI: 10.33594/000000069.
- Fornasiero, Eugenio F. et al. (2018). 'Precisely measured protein lifetimes in the mouse brain reveal differences across tissues and subcellular fractions'. In: *Nature Communications* 9. Publisher: Nature Publishing Group. DOI: 10.1038/s41467-018-06519-0. URL: <https://www.ncbi.nlm.nih.gov/pmc/articles/PMC6185916/> (visited on 03/07/2023).
- Galtrey, Clare M. et al. (2008). 'Distribution and synthesis of extracellular matrix proteoglycans, hyaluronan, link proteins and tenascin-R in the rat spinal cord'. In: *European Journal of Neuroscience* 27.6, pp. 1373–1390. ISSN: 1460-9568. DOI: 10.1111/j.1460-9568.2008.06108.x. URL: <https://onlinelibrary.wiley.com/doi/abs/10.1111/j.1460-9568.2008.06108.x> (visited on 21/06/2023).
- Goddard, Thomas D. et al. (Jan. 2018). 'UCSF ChimeraX: Meeting modern challenges in visualization and analysis'. In: *Protein Science: A Publication of the Protein Society* 27.1, pp. 14–25. ISSN: 1469-896X. DOI: 10.1002/pro.3235.
- Gogolla, Nadine et al. (4th Sept. 2009). 'Perineuronal nets protect fear memories from erasure'. In: *Science (New York, N.Y.)* 325.5945, pp. 1258–1261. ISSN: 1095-9203. DOI: 10.1126/science.1174146.

- Gottschling, Christine et al. (Dec. 2019). 'Elimination of the four extracellular matrix molecules tenascin-C, tenascin-R, brevican and neurocan alters the ratio of excitatory and inhibitory synapses'. In: *Scientific Reports* 9.1. Publisher: Nature Publishing Group, pp. 1–17. ISSN: 20452322. DOI: 10.1038/s41598-019-50404-9.
- Grienberger, Christine and Arthur Konnerth (8th Mar. 2012). 'Imaging Calcium in Neurons'. In: *Neuron* 73.5, pp. 862–885. ISSN: 0896-6273. DOI: 10.1016/j.neuron.2012.02.011. URL: <https://www.sciencedirect.com/science/article/pii/S0896627312001729> (visited on 25/06/2023).
- Grynkiewicz, G, M Poenie and R Y Tsien (25th Mar. 1985). 'A new generation of Ca²⁺ indicators with greatly improved fluorescence properties.' In: *Journal of Biological Chemistry* 260.6, pp. 3440–3450. ISSN: 0021-9258. DOI: 10.1016/S0021-9258(19)83641-4. URL: <https://www.sciencedirect.com/science/article/pii/S0021925819836414> (visited on 14/06/2023).
- Happel, Max F K et al. (Feb. 2014). 'Enhanced cognitive flexibility in reversal learning induced by removal of the extracellular matrix in auditory cortex.' In: *Proceedings of the National Academy of Sciences of the United States of America* 111.7, pp. 2800–5. ISSN: 1091-6490. DOI: 10.1073/pnas.1310272111.
- Hardingham, Timothy E. and Amanda J. Fosang (1992). 'Proteoglycans: many forms and many functions'. In: *The FASEB Journal* 6.3, pp. 861–870. ISSN: 1530-6860. DOI: 10.1096/fasebj.6.3.1740236. URL: <https://onlinelibrary.wiley.com/doi/abs/10.1096/fasebj.6.3.1740236> (visited on 13/06/2023).
- Hayani, Hussam, Inseon Song and Alexander Dityatev (30th May 2018). 'Increased excitability and reduced excitatory synaptic input into fast-spiking CA2 interneurons after enzymatic attenuation of extracellular matrix'. In: *Frontiers in Cellular Neuroscience* 12. Publisher: Frontiers Media S.A., p. 149. ISSN: 16625102. DOI: 10.3389/FNCEL.2018.00149/FULL. URL: </pmc/articles/PMC5988902/> (visited on 09/06/2023).
- Headon, M P and T P Powell (Oct. 1973). 'Cellular changes in the lateral geniculate nucleus of infant monkeys after suture of the eyelids.' In: *Journal of Anatomy* 116 (Pt 1), pp. 135–145. ISSN: 0021-8782. URL: <https://www.ncbi.nlm.nih.gov/pmc/articles/PMC1271555/> (visited on 29/06/2023).

- Hebb, D. O. (1949). *The organization of behavior; a neuropsychological theory*. The organization of behavior; a neuropsychological theory. Pages: xix, 335. Oxford, England: Wiley. xix, 335.
- Hensch, Takao K. and Michael P. Stryker (12th Mar. 2004). 'Columnar architecture sculpted by GABA circuits in developing cat visual cortex'. In: *Science (New York, N.Y.)* 303.5664, pp. 1678–1681. ISSN: 1095-9203. DOI: 10.1126/science.1091031.
- Herculano-Houzel, Suzana (9th Nov. 2009). 'The Human Brain in Numbers: A Linearly Scaled-up Primate Brain'. In: *Frontiers in Human Neuroscience* 3, p. 31. ISSN: 1662-5161. DOI: 10.3389/neuro.09.031.2009. URL: <https://www.ncbi.nlm.nih.gov/pmc/articles/PMC2776484/> (visited on 26/06/2023).
- Higaki, Akinori et al. (May 2018). 'Recognition of early stage thigmotaxis in morris water maze test with convolutional neural network'. In: *PLoS ONE* 13.5. Publisher: Public Library of Science. ISSN: 19326203. DOI: 10.1371/journal.pone.0197003.
- Hodgkin, A. L. and A. F. Huxley (28th Aug. 1952). 'A quantitative description of membrane current and its application to conduction and excitation in nerve'. In: *The Journal of Physiology* 117.4, pp. 500–544. ISSN: 0022-3751. URL: <https://www.ncbi.nlm.nih.gov/pmc/articles/PMC1392413/> (visited on 14/06/2023).
- Hofer, Sonja B. et al. (15th Jan. 2009). 'Experience leaves a lasting structural trace in cortical circuits'. In: *Nature* 457.7227, pp. 313–317. ISSN: 1476-4687. DOI: 10.1038/nature07487.
- Hrabětová, Sabina et al. (15th Aug. 2009). 'Calcium diffusion enhanced after cleavage of negatively charged components of brain extracellular matrix by chondroitinase ABC'. In: *The Journal of Physiology* 587 (Pt 16), pp. 4029–4049. ISSN: 0022-3751. DOI: 10.1113/jphysiol.2009.170092. URL: <https://www.ncbi.nlm.nih.gov/pmc/articles/PMC2756436/> (visited on 23/06/2023).
- Hu, H., J. Gan and P. Jonas (Aug. 2014). 'Fast-spiking, parvalbumin+ GABAergic interneurons: From cellular design to microcircuit function'. In: *Science* 345.6196. Publisher: American Association for the Advancement of Science, pp. 1255263–1255263. ISSN: 0036-8075. DOI: 10.1126/science.1255263.
- Hubel, D. H. and T. N. Wiesel (Jan. 1962). 'Receptive fields, binocular interaction and functional architecture in the cat's visual cortex'. In:

- The Journal of Physiology* 160.1, pp. 106–154.2. ISSN: 0022-3751. URL: <https://www.ncbi.nlm.nih.gov/pmc/articles/PMC1359523/> (visited on 28/06/2023).
- Hubel, David Hunter and Torsten Nils Wiesel (Jan. 1997). ‘Ferrier lecture - Functional architecture of macaque monkey visual cortex’. In: *Proceedings of the Royal Society of London. Series B. Biological Sciences* 198.1130. Publisher: Royal Society, pp. 1–59. DOI: 10.1098/rspb.1977.0085. URL: <https://royalsocietypublishing.org/doi/10.1098/rspb.1977.0085> (visited on 28/06/2023).
- Josselyn, Sheena A., Stefan Köhler and Paul W. Frankland (Sept. 2015). ‘Finding the engram’. In: *Nature Reviews Neuroscience* 16.9. Number: 9. Publisher: Nature Publishing Group, pp. 521–534. ISSN: 1471-0048. DOI: 10.1038/nrn4000. URL: <https://www.nature.com/articles/nrn4000> (visited on 03/07/2023).
- Josselyn, Sheena A. and Susumu Tonegawa (3rd Jan. 2020). ‘Memory engrams: Recalling the past and imagining the future’. In: *Science* 367.6473. Publisher: American Association for the Advancement of Science, eaaw4325. DOI: 10.1126/science.aaw4325. URL: <https://www.science.org/doi/10.1126/science.aaw4325> (visited on 03/07/2023).
- Katz, L. C. and C. J. Shatz (15th Nov. 1996). ‘Synaptic activity and the construction of cortical circuits’. In: *Science (New York, N.Y.)* 274.5290, pp. 1133–1138. ISSN: 0036-8075. DOI: 10.1126/science.274.5290.1133.
- Keck, Tara et al. (5th Mar. 2017). ‘Integrating Hebbian and homeostatic plasticity: the current state of the field and future research directions’. In: *Philosophical Transactions of the Royal Society B: Biological Sciences* 372.1715. Publisher: Royal Society, p. 20160158. DOI: 10.1098/rstb.2016.0158. URL: <https://royalsocietypublishing.org/doi/full/10.1098/rstb.2016.0158> (visited on 29/06/2023).
- Kelwick, Richard et al. (2015). ‘Metalloproteinase dependent and independent processes contribute to inhibition of breast cancer cell migration, angiogenesis and liver metastasis by a disintegrin and metalloproteinase with thrombospondin motifs-15’. In: *International Journal of Cancer* 136.4, E14–E26. ISSN: 1097-0215. DOI: 10.1002/ijc.29129. URL: <https://onlinelibrary.wiley.com/doi/abs/10.1002/ijc.29129> (visited on 17/06/2023).
- Kirkwood, Alfredo, Alcino Silva and Mark F. Bear (Apr. 1997). ‘Age-dependent decrease of synaptic plasticity in the neocortex of aCaMKII

- mutant mice'. In: *Proceedings of the National Academy of Sciences* 94.7. Publisher: Proceedings of the National Academy of Sciences, pp. 3380–3383. DOI: 10.1073/pnas.94.7.3380. URL: <https://www.pnas.org/doi/full/10.1073/pnas.94.7.3380> (visited on 28/06/2023).
- Kobayashi, Yohei, Zhanlei Ye and Takao K. Hensch (8th Apr. 2015). 'Clock genes control cortical critical period timing'. In: *Neuron* 86.1, pp. 264–275. ISSN: 1097-4199. DOI: 10.1016/j.neuron.2015.02.036.
- Kuhlman, Sandra J. et al. (Sept. 2013). 'A disinhibitory microcircuit initiates critical-period plasticity in the visual cortex'. In: *Nature* 501.7468. Number: 7468 Publisher: Nature Publishing Group, pp. 543–546. ISSN: 1476-4687. DOI: 10.1038/nature12485. URL: <https://www.nature.com/articles/nature12485> (visited on 12/06/2023).
- Kuno, Kouji et al. (4th Aug. 2000). 'ADAMTS-1 cleaves a cartilage proteoglycan, aggrecan'. In: *FEBS Letters* 478.3, pp. 241–245. ISSN: 0014-5793. DOI: 10.1016/S0014-5793(00)01854-8. URL: <https://www.sciencedirect.com/science/article/pii/S0014579300018548> (visited on 17/06/2023).
- Kwok, Jessica C F et al. (Nov. 2011). 'Extracellular matrix and perineuronal nets in CNS repair.' In: *Developmental neurobiology* 71.11, pp. 1073–89. ISSN: 1932-846X. DOI: 10.1002/dneu.20974.
- Lensjø, Kristian Kinden, Ane Charlotte Christensen et al. (2017). 'Differential Expression and Cell-Type Specificity of Perineuronal Nets in Hippocampus, Medial Entorhinal Cortex, and Visual Cortex Examined in the Rat and Mouse'. In: *eneuro* 4.3, ENEURO.0379–16.2017. ISSN: 2373-2822. DOI: 10.1523/ENEURO.0379-16.2017.
- Lensjø, Kristian Kinden, Mikkel Elle Lepperød et al. (Feb. 2017). 'Removal of perineuronal nets unlocks juvenile plasticity through network mechanisms of decreased inhibition and increased gamma activity'. In: *Journal of Neuroscience* 37.5, pp. 1269–1283. ISSN: 15292401. DOI: 10.1523/JNEUROSCI.2504-16.2016.
- Lev-Ram, Varda et al. (9th Apr. 2023). *Do perineuronal nets stabilize the engram of a synaptic circuit?* Pages: 2023.04.09.536164 Section: New Results. DOI: 10.1101/2023.04.09.536164. URL: <https://www.biorxiv.org/content/10.1101/2023.04.09.536164v1> (visited on 29/06/2023).
- Levay, Simon, Michael P. Stryker and Carla J. Shatz (1978). 'Ocular dominance columns and their development in layer IV of the cat's visual cortex: A quantitative study'. In: *Journal of Comparative Neurology* 179.1.

- _eprint: <https://onlinelibrary.wiley.com/doi/pdf/10.1002/cne.901790113>, pp. 223–244. ISSN: 1096-9861. DOI: 10.1002/cne.901790113. URL: <https://onlinelibrary.wiley.com/doi/abs/10.1002/cne.901790113> (visited on 28/06/2023).
- Levelt, Christiaan N. and Mark Hübener (2012). ‘Critical-Period Plasticity in the Visual Cortex’. In: *Annual Review of Neuroscience* 35.1. _eprint: <https://doi.org/10.1146/annurev-neuro-061010-113813>, pp. 309–330. DOI: 10.1146/annurev-neuro-061010-113813. URL: <https://doi.org/10.1146/annurev-neuro-061010-113813> (visited on 11/06/2023).
- Levy, C. et al. (1st Mar. 2015). ‘Cell-specific and developmental expression of lectican-cleaving proteases in mouse hippocampus and neocortex’. In: *The Journal of comparative neurology* 523.4, pp. 629–648. ISSN: 0021-9967. DOI: 10.1002/cne.23701. URL: <https://www.ncbi.nlm.nih.gov/pmc/articles/PMC4304879/> (visited on 17/06/2023).
- Li, Jia et al. (June 2023). ‘Engineering of NEMO as calcium indicators with large dynamics and high sensitivity’. In: *Nature Methods* 20.6. Number: 6 Publisher: Nature Publishing Group, pp. 918–924. ISSN: 1548-7105. DOI: 10.1038/s41592-023-01852-9. URL: <https://www.nature.com/articles/s41592-023-01852-9> (visited on 03/07/2023).
- Lin, Michael Z. and Mark J. Schnitzer (Sept. 2016). ‘Genetically encoded indicators of neuronal activity’. In: *Nature Neuroscience* 19.9. Number: 9 Publisher: Nature Publishing Group, pp. 1142–1153. ISSN: 1546-1726. DOI: 10.1038/nn.4359. URL: <https://www.nature.com/articles/nn.4359> (visited on 25/06/2023).
- Liu, Luping, Yujie Zhang and Jun Ju (10th Aug. 2022). ‘Removal of perineuronal nets leads to altered neuronal excitability and synaptic transmission in the visual cortex with distinct time courses’. In: *Neuroscience Letters* 785, p. 136763. ISSN: 0304-3940. DOI: 10.1016/j.neulet.2022.136763. URL: <https://www.sciencedirect.com/science/article/pii/S030439402200324X> (visited on 27/06/2023).
- Liu, Luping, Yujie Zhang, Siqi Men et al. (2023). ‘Elimination of perineuronal nets in CA1 disrupts GABA release and long-term contextual fear memory retention’. In: *Hippocampus* n/a (n/a). ISSN: 1098-1063. DOI: 10.1002/hipo.23503. URL: <https://onlinelibrary.wiley.com/doi/abs/10.1002/hipo.23503> (visited on 20/06/2023).
- Lorenz, Konrad (1st Apr. 1935). ‘Der Kumpan in der Umwelt des Vogels’. In: *Journal für Ornithologie* 83.2, pp. 137–213. ISSN: 1439-0361. DOI: 10.

- 1007/BF01905355. URL: <https://doi.org/10.1007/BF01905355> (visited on 11/06/2023).
- Luo, Liqun, Edward M. Callaway and Karel Svoboda (18th Apr. 2018). 'Genetic Dissection of Neural Circuits: A Decade of Progress'. In: *Neuron* 98.2, pp. 256–281. ISSN: 0896-6273. DOI: 10.1016/j.neuron.2018.03.040. URL: <https://www.sciencedirect.com/science/article/pii/S0896627318302460> (visited on 25/06/2023).
- Lupori, Leonardo et al. (25th Jan. 2023). 'A Comprehensive Atlas of Perineuronal Net Distribution and Colocalization with Parvalbumin in the Adult Mouse Brain'. In: *bioRxiv*. Publisher: Cold Spring Harbor Laboratory, p. 2023.01.24.525313. DOI: 10.1101/2023.01.24.525313. URL: <https://www.biorxiv.org/content/10.1101/2023.01.24.525313v1> (visited on 10/06/2023).
- Margolis, R. K., R. U. Margolis et al. (4th Nov. 1975). 'Distribution and metabolism of glycoproteins and glycosaminoglycans in subcellular fractions of brain'. In: *Biochemistry* 14.22, pp. 4797–4804. ISSN: 0006-2960. DOI: 10.1021/bi00693a004.
- Margolis, R. K., C. Preti et al. (Nov. 1975). 'Metabolism of the protein moiety of brain glycoproteins'. In: *Journal of Neurochemistry* 25.5, pp. 707–709. ISSN: 0022-3042. DOI: 10.1111/j.1471-4159.1975.tb04392.x.
- Marín, Oscar (Nov. 2016). 'Developmental timing and critical windows for the treatment of psychiatric disorders'. In: *Nature Medicine* 22.11. Publisher: Nature Publishing Group, pp. 1229–1238. ISSN: 1546170X. DOI: 10.1038/nm.4225.
- Matthews, Russell T. et al. (1st Sept. 2002). 'Aggrecan Glycoforms Contribute to the Molecular Heterogeneity of Perineuronal Nets'. In: *The Journal of Neuroscience* 22.17, pp. 7536–7547. ISSN: 0270-6474. DOI: 10.1523/JNEUROSCI.22-17-07536.2002. URL: <https://www.ncbi.nlm.nih.gov/pmc/articles/PMC6757962/> (visited on 21/06/2023).
- Mauney, Sarah A. et al. (15th Sept. 2013). 'Developmental Pattern of Perineuronal Nets in the Human Prefrontal Cortex and Their Deficit in Schizophrenia'. In: *Biological Psychiatry*. Schizophrenia: Biomarkers of Risk and Illness Progression 74.6, pp. 427–435. ISSN: 0006-3223. DOI: 10.1016/j.biopsych.2013.05.007. URL: <https://www.sciencedirect.com/science/article/pii/S0006322313004174> (visited on 24/06/2023).
- McRae, Paulette A. and Brenda E. Porter (1st Dec. 2012). 'The perineuronal net component of the extracellular matrix in plasticity and epilepsy'.

- In: *Neurochemistry International* 61.7, pp. 963–972. ISSN: 0197-0186. DOI: 10.1016/j.neuint.2012.08.007. URL: <https://www.sciencedirect.com/science/article/pii/S0197018612002744> (visited on 24/06/2023).
- Michelson, Nicholas J., Matthieu P. Vanni and Timothy H. Murphy (June 2019). ‘Comparison between transgenic and AAV-PHP.eB-mediated expression of GCaMP6s using in vivo wide-field functional imaging of brain activity’. In: *Neurophotonics* 6.2. Publisher: SPIE, p. 025014. ISSN: 2329-423X, 2329-4248. DOI: 10.1117/1.NPh.6.2.025014. URL: <https://www.spiedigitallibrary.org/journals/neurophotonics/volume-6/issue-2/025014/Comparison-between-transgenic-and-AAV-PHPeB-mediated-expression-of-GCaMP6s/10.1117/1.NPh.6.2.025014.full> (visited on 03/07/2023).
- Miller, Mark N. et al. (1st Jan. 2011). ‘Activity-Dependent Changes in the Firing Properties of Neocortical Fast-Spiking Interneurons in the Absence of Large Changes in Gene Expression’. In: *Developmental neurobiology* 71.1, pp. 62–70. ISSN: 1932-8451. DOI: 10.1002/dneu.20811. URL: <https://www.ncbi.nlm.nih.gov/pmc/articles/PMC3059083/> (visited on 02/07/2023).
- Miyata, Seiji, Yousuke Nishimura and Toshihiro Nakashima (30th May 2007). ‘Perineuronal nets protect against amyloid Beta-protein neurotoxicity in cultured cortical neurons’. In: *Brain Research* 1150, pp. 200–206. ISSN: 0006-8993. DOI: 10.1016/j.brainres.2007.02.066. URL: <https://www.sciencedirect.com/science/article/pii/S0006899307004969> (visited on 24/06/2023).
- Miyata, Shinji and Hiroshi Kitagawa (2016). ‘Chondroitin 6-Sulfation Regulates Perineuronal Net Formation by Controlling the Stability of Aggrecan’. In: *Neural Plasticity* 2016, p. 1305801. ISSN: 2090-5904. DOI: 10.1155/2016/1305801. URL: <https://www.ncbi.nlm.nih.gov/pmc/articles/PMC4738747/> (visited on 17/06/2023).
- Morawski, M. et al. (1st Sept. 2010). ‘Neurons associated with aggrecan-based perineuronal nets are protected against tau pathology in subcortical regions in Alzheimer’s disease’. In: *Neuroscience* 169.3, pp. 1347–1363. ISSN: 0306-4522. DOI: 10.1016/j.neuroscience.2010.05.022. URL: <https://www.sciencedirect.com/science/article/pii/S0306452210007426> (visited on 24/06/2023).
- Morawski, Markus et al. (13th Jan. 2012). ‘Involvement of Perineuronal and Perisynaptic Extracellular Matrix in Alzheimer’s Disease Neuro-

- pathology'. In: *Brain Pathology* 22.4, pp. 547–561. ISSN: 1015-6305. DOI: 10.1111/j.1750-3639.2011.00557.x. URL: <https://www.ncbi.nlm.nih.gov/pmc/articles/PMC3639011/> (visited on 21/06/2023).
- Nakada, Mitsutoshi et al. (Sept. 2005). 'Human glioblastomas overexpress ADAMTS-5 that degrades brevican'. In: *Acta Neuropathologica* 110.3, pp. 239–246. ISSN: 0001-6322. DOI: 10.1007/s00401-005-1032-6.
- Nakai, Junichi, Masamichi Ohkura and Keiji Imoto (Feb. 2001). 'A high signal-to-noise Ca²⁺ probe composed of a single green fluorescent protein'. In: *Nature Biotechnology* 19.2. Number: 2 Publisher: Nature Publishing Group, pp. 137–141. ISSN: 1546-1696. DOI: 10.1038/84397. URL: https://www.nature.com/articles/nbt0201_137 (visited on 25/06/2023).
- Nicholson, C. and E. Syková (May 1998). 'Extracellular space structure revealed by diffusion analysis'. In: *Trends in Neurosciences* 21.5, pp. 207–215. ISSN: 0166-2236. DOI: 10.1016/s0166-2236(98)01261-2.
- Nordby, J. Cully, S. Elizabeth Campbell and Michael D. Beecher (1st Apr. 2001). 'Late song learning in song sparrows'. In: *Animal Behaviour* 61.4, pp. 835–846. ISSN: 0003-3472. DOI: 10.1006/anbe.2000.1673. URL: <https://www.sciencedirect.com/science/article/pii/S0003347200916737> (visited on 28/06/2023).
- Pantazopoulos, Harry et al. (31st July 2020). 'Circadian Rhythms of Perineuronal Net Composition'. In: *eNeuro* 7.4, ENEURO.0034–19.2020. ISSN: 2373-2822. DOI: 10.1523/ENEURO.0034-19.2020. URL: <https://www.ncbi.nlm.nih.gov/pmc/articles/PMC7405073/> (visited on 17/06/2023).
- Pizzorusso, Tommaso, Paolo Medini, Nicoletta Berardi et al. (Nov. 2002). 'Reactivation of ocular dominance plasticity in the adult visual cortex.' In: *Science (New York, N.Y.)* 298.5596, pp. 1248–51. ISSN: 1095-9203. DOI: 10.1126/science.1072699.
- Pizzorusso, Tommaso, Paolo Medini, Silvia Landi et al. (30th May 2006). 'Structural and functional recovery from early monocular deprivation in adult rats'. In: *Proceedings of the National Academy of Sciences* 103.22. Publisher: Proceedings of the National Academy of Sciences, pp. 8517–8522. DOI: 10.1073/pnas.0602657103. URL: <https://www.pnas.org/doi/10.1073/pnas.0602657103> (visited on 14/06/2023).
- Pritchett, David et al. (Apr. 2016). 'Searching for cognitive enhancement in the Morris water maze: better and worse performance in D-amino acid oxidase knockout (*Dao*^{-/-}) mice'. In: *European Journal of Neuroscience*

- 43.7. Ed. by Anthony Isles. Publisher: Blackwell Publishing Ltd, pp. 979–989. ISSN: 0953816X. DOI: 10.1111/ejn.13192.
- Pyka, Martin et al. (June 2011). ‘Chondroitin sulfate proteoglycans regulate astrocyte-dependent synaptogenesis and modulate synaptic activity in primary embryonic hippocampal neurons’. In: *The European Journal of Neuroscience* 33.12, pp. 2187–2202. ISSN: 1460-9568. DOI: 10.1111/j.1460-9568.2011.07690.x.
- Rankin-Gee, Elyse K. et al. (2015). ‘Perineuronal net degradation in epilepsy’. In: *Epilepsia* 56.7, pp. 1124–1133. ISSN: 1528-1167. DOI: 10.1111/epi.13026. URL: <https://onlinelibrary.wiley.com/doi/abs/10.1111/epi.13026> (visited on 24/06/2023).
- Robinson, Paul et al. (1st July 2023). ‘Comparing the effects of chemical Ca²⁺ dyes and R-GECO on contractility and Ca²⁺ transients in adult and human iPSC cardiomyocytes’. In: *Journal of Molecular and Cellular Cardiology* 180, pp. 44–57. ISSN: 0022-2828. DOI: 10.1016/j.yjmcc.2023.04.008. URL: <https://www.sciencedirect.com/science/article/pii/S0022282823000809> (visited on 14/06/2023).
- Romberg, Carola et al. (17th Apr. 2013). ‘Depletion of Perineuronal Nets Enhances Recognition Memory and Long-Term Depression in the Perirhinal Cortex’. In: *The Journal of Neuroscience* 33.16, pp. 7057–7065. ISSN: 0270-6474. DOI: 10.1523/JNEUROSCI.6267-11.2013. URL: <https://www.ncbi.nlm.nih.gov/pmc/articles/PMC3655688/> (visited on 15/06/2023).
- Rossier, J et al. (Feb. 2015). ‘Cortical fast-spiking parvalbumin interneurons enwrapped in the perineuronal net express the metallopeptidases Adamts8, Adamts15 and Neprilysin’. In: *Molecular Psychiatry* 20.2, pp. 154–161. ISSN: 1359-4184. DOI: 10.1038/mp.2014.162. URL: <https://www.ncbi.nlm.nih.gov/pmc/articles/PMC4356748/> (visited on 17/06/2023).
- Rowlands, Daire et al. (Nov. 2018). ‘Aggrecan directs extracellular matrix-mediated neuronal plasticity’. In: *Journal of Neuroscience* 38.47. Publisher: Society for Neuroscience, pp. 10102–10113. ISSN: 15292401. DOI: 10.1523/JNEUROSCI.1122-18.2018.
- Scarlett, Jarrad M., Shannon J. Hu and Kimberly M. Alonge (2022). ‘The “Loss” of Perineuronal Nets in Alzheimer’s Disease: Missing or Hiding in Plain Sight?’ In: *Frontiers in Integrative Neuroscience* 16. ISSN: 1662-

5145. URL: <https://www.frontiersin.org/articles/10.3389/fnint.2022.896400> (visited on 30/06/2023).
- Shemesh, Or A. et al. (5th Aug. 2020). 'Precision Calcium Imaging of Dense Neural Populations via a Cell-Body-Targeted Calcium Indicator'. In: *Neuron* 107.3, 470–486.e11. ISSN: 0896-6273. DOI: 10.1016/j.neuron.2020.05.029. URL: <https://www.sciencedirect.com/science/article/pii/S0896627320303986> (visited on 25/06/2023).
- Slaker, Megan et al. (Mar. 2015). 'Removal of perineuronal nets in the medial prefrontal cortex impairs the acquisition and reconsolidation of a cocaine-induced conditioned place preference memory.' In: *The Journal of neuroscience : the official journal of the Society for Neuroscience* 35.10, pp. 4190–202. ISSN: 1529-2401. DOI: 10.1523/JNEUROSCI.3592-14.2015.
- Snow, D. M. et al. (Nov. 1994). 'Chondroitin sulfate proteoglycan elevates cytoplasmic calcium in DRG neurons'. In: *Developmental Biology* 166.1, pp. 87–100. ISSN: 0012-1606. DOI: 10.1006/dbio.1994.1298.
- Sohal, Vikaas S. et al. (4th June 2009). 'Parvalbumin neurons and gamma rhythms enhance cortical circuit performance'. In: *Nature* 459.7247, pp. 698–702. ISSN: 1476-4687. DOI: 10.1038/nature07991.
- Stanton, Heather et al. (1st Dec. 2011). 'Proteoglycan degradation by the ADAMTS family of proteinases'. In: *Biochimica et Biophysica Acta (BBA) - Molecular Basis of Disease* 1812.12, pp. 1616–1629. ISSN: 0925-4439. DOI: 10.1016/j.bbadis.2011.08.009. URL: <https://www.sciencedirect.com/science/article/pii/S0925443911001918> (visited on 17/06/2023).
- Steinmetz, Nicholas A. et al. (1st Sept. 2017). 'Aberrant Cortical Activity in Multiple GCaMP6-Expressing Transgenic Mouse Lines'. In: *eNeuro* 4.5. Publisher: Society for Neuroscience Section: Methods/New Tools. ISSN: 2373-2822. DOI: 10.1523/ENEURO.0207-17.2017. URL: <https://www.eneuro.org/content/4/5/ENEURO.0207-17.2017> (visited on 28/06/2023).
- Sterratt, David et al. (2023). *Principles of Computational Modelling in Neuroscience*. 2nd ed. Cambridge University Press.
- Stohs, S. J. and D. Bagchi (Feb. 1995). 'Oxidative mechanisms in the toxicity of metal ions'. In: *Free Radical Biology & Medicine* 18.2, pp. 321–336. ISSN: 0891-5849. DOI: 10.1016/0891-5849(94)00159-h.
- Sugiyama, Sayaka et al. (Aug. 2008). 'Experience-Dependent Transfer of Otx2 Homeoprotein into the Visual Cortex Activates Postnatal Plasticity'. In: *Cell* 134.3, pp. 508–520. ISSN: 00928674. DOI: 10.1016/j.cell.2008.05.054.

- Suttkus, A. et al. (Mar. 2014). 'Aggrecan, link protein and tenascin-R are essential components of the perineuronal net to protect neurons against iron-induced oxidative stress'. In: *Cell Death & Disease* 5.3. Number: 3 Publisher: Nature Publishing Group, e1119–e1119. ISSN: 2041-4889. DOI: 10.1038/cddis.2014.25. URL: <https://www.nature.com/articles/cddis201425> (visited on 24/06/2023).
- Suttkus, Anne et al. (23rd July 2012). 'Neuroprotection against iron-induced cell death by perineuronal nets - an in vivo analysis of oxidative stress'. In: *American Journal of Neurodegenerative Disease* 1.2, pp. 122–129. ISSN: 2165-591X. URL: <https://www.ncbi.nlm.nih.gov/pmc/articles/PMC3560462/> (visited on 24/06/2023).
- Tewari, Bhanu P et al. (2018). 'Perineuronal nets decrease membrane capacitance of peritumoral fast spiking interneurons in a model of epilepsy.' In: *Nature communications* 9.1. Publisher: Nature Publishing Group, p. 4724. ISSN: 2041-1723. DOI: 10.1038/s41467-018-07113-0.
- Thompson, Elise Holter et al. (Jan. 2018). 'Removal of perineuronal nets disrupts recall of a remote fear memory'. In: *Proceedings of the National Academy of Sciences of the United States of America* 115.3. Publisher: National Academy of Sciences, pp. 607–612. ISSN: 10916490. DOI: 10.1073/pnas.1713530115.
- Tsien, Roger Y. (23rd July 2013). 'Very long-term memories may be stored in the pattern of holes in the perineuronal net'. In: *Proceedings of the National Academy of Sciences* 110.30. Publisher: Proceedings of the National Academy of Sciences, pp. 12456–12461. DOI: 10.1073/pnas.1310158110. URL: <https://www.pnas.org/doi/10.1073/pnas.1310158110> (visited on 29/06/2023).
- Vardalaki, Dimitra, Kwanghun Chung and Mark T. Harnett (Dec. 2022). 'Filopodia are a structural substrate for silent synapses in adult neocortex'. In: *Nature* 612.7939. Number: 7939 Publisher: Nature Publishing Group, pp. 323–327. ISSN: 1476-4687. DOI: 10.1038/s41586-022-05483-6. URL: <https://www.nature.com/articles/s41586-022-05483-6> (visited on 02/07/2023).
- Verma, Priyanka and Krishna Dalal (Dec. 2011). 'ADAMTS-4 and ADAMTS-5: key enzymes in osteoarthritis'. In: *Journal of Cellular Biochemistry* 112.12, pp. 3507–3514. ISSN: 1097-4644. DOI: 10.1002/jcb.23298.
- Wait, Sarah J. et al. (16th Apr. 2023). *Machine Learning Ensemble Directed Engineering of Genetically Encoded Fluorescent Calcium Indicators*.

- Pages: 2023.04.13.536801 Section: New Results. DOI: 10.1101/2023.04.13.536801. URL: <https://www.biorxiv.org/content/10.1101/2023.04.13.536801v1> (visited on 03/07/2023).
- Wang, Difei and James Fawcett (1st July 2012). 'The perineuronal net and the control of CNS plasticity'. In: *Cell and Tissue Research* 349.1, pp. 147–160. ISSN: 1432-0878. DOI: 10.1007/s00441-012-1375-y. URL: <https://doi.org/10.1007/s00441-012-1375-y> (visited on 14/06/2023).
- Wen, Teresa H. et al. (3rd Aug. 2018). 'The Perineuronal 'Safety' Net? Perineuronal Net Abnormalities in Neurological Disorders'. In: *Frontiers in Molecular Neuroscience* 11, p. 270. ISSN: 1662-5099. DOI: 10.3389/fnmol.2018.00270. URL: <https://www.ncbi.nlm.nih.gov/pmc/articles/PMC6085424/> (visited on 19/06/2023).
- Westling, Jennifer et al. (3rd May 2002). 'ADAMTS4 cleaves at the aggrecanase site (Glu373-Ala374) and secondarily at the matrix metalloproteinase site (Asn341-Phe342) in the aggrecan interglobular domain'. In: *The Journal of Biological Chemistry* 277.18, pp. 16059–16066. ISSN: 0021-9258. DOI: 10.1074/jbc.M108607200.
- WIESEL, T. N. and D. H. HUBEL (Nov. 1963). 'SINGLE-CELL RESPONSES IN STRIATE CORTEX OF KITTENS DEPRIVED OF VISION IN ONE EYE'. In: *Journal of neurophysiology* 26. Publisher: J Neurophysiol, pp. 1003–1017. ISSN: 00223077. DOI: 10.1152/jn.1963.26.6.1003.
- Wilczynski, Grzegorz M. et al. (10th Mar. 2008). 'Important role of matrix metalloproteinase 9 in epileptogenesis'. In: *Journal of Cell Biology* 180.5, pp. 1021–1035. ISSN: 0021-9525. DOI: 10.1083/jcb.200708213. URL: <https://doi.org/10.1083/jcb.200708213> (visited on 24/06/2023).
- Wingert, J C and B A Sorg (2021). 'Impact of Perineuronal Nets on Electrophysiology of Parvalbumin Interneurons, Principal Neurons, and Brain Oscillations: A Review'. In: *Review. Front. Synaptic Neurosci* 13, p. 673210. DOI: 10.3389/fnsyn.2021.673210. URL: www.frontiersin.org (visited on 09/06/2023).
- Yazaki-Sugiyama, Yoko et al. (Nov. 2009). 'Bidirectional plasticity in fast-spiking GABA circuits by visual experience'. In: *Nature* 462.7270. Number: 7270 Publisher: Nature Publishing Group, pp. 218–221. ISSN: 1476-4687. DOI: 10.1038/nature08485. URL: <https://www.nature.com/articles/nature08485> (visited on 28/06/2023).
- Ye, Qian and Qing-Long Miao (8th Aug. 2013). 'Experience-dependent development of perineuronal nets and chondroitin sulfate proteoglycan

- receptors in mouse visual cortex'. In: *Matrix Biology: Journal of the International Society for Matrix Biology* 32.6, pp. 352–363. ISSN: 1569-1802. DOI: 10.1016/j.matbio.2013.04.001.
- Yuan, W. et al. (2002). 'Association between protease-specific proteolytic cleavage of brevican and synaptic loss in the dentate gyrus of kainate-treated rats'. In: *Neuroscience* 114.4, pp. 1091–1101. ISSN: 0306-4522. DOI: 10.1016/s0306-4522(02)00347-0.
- Yutsudo, Noriko and Hiroshi Kitagawa (1st Dec. 2015). 'Involvement of chondroitin 6-sulfation in temporal lobe epilepsy'. In: *Experimental Neurology*. Deciphering sugar chain-based signals regulating integrative neuronal functions 274, pp. 126–133. ISSN: 0014-4886. DOI: 10.1016/j.expneurol.2015.07.009. URL: <https://www.sciencedirect.com/science/article/pii/S001448861530042X> (visited on 24/06/2023).
- Zenke, Friedemann, Guillaume Hennequin and Wulfram Gerstner (14th Nov. 2013). 'Synaptic Plasticity in Neural Networks Needs Homeostasis with a Fast Rate Detector'. In: *PLOS Computational Biology* 9.11. Publisher: Public Library of Science, e1003330. ISSN: 1553-7358. DOI: 10.1371/journal.pcbi.1003330. URL: <https://journals.plos.org/ploscompbiol/article?id=10.1371/journal.pcbi.1003330> (visited on 29/06/2023).
- Zhang, Yan et al. (Mar. 2023). 'Fast and sensitive GCaMP calcium indicators for imaging neural populations'. In: *Nature* 615.7954. Number: 7954. Publisher: Nature Publishing Group, pp. 884–891. ISSN: 1476-4687. DOI: 10.1038/s41586-023-05828-9. URL: <https://www.nature.com/articles/s41586-023-05828-9> (visited on 25/06/2023).

Papers

Paper I

Deciphering the Role of Aggrecan in Parvalbumin Interneurons: Unexpected Outcomes from a Conditional ACAN Knockout That Eliminates WFA+ Perineuronal nets

Paper II

Responses in Fast-spiking Interneuron Firing Rates to Parameter Variations Associated with Degradation of Perineuronal Nets

III



Responses in fast-spiking interneuron firing rates to parameter variations associated with degradation of perineuronal nets

Kine Ødegård Hanssen^{1,2} · Sverre Grødem^{2,3} · Marianne Fyhn^{2,3} · Torkel Hafting^{2,4} · Gaute T. Einevoll^{1,2,5} · Torbjørn Vefferstad Ness^{2,5} · Geir Halmes^{2,5}

Received: 24 October 2022 / Revised: 1 March 2023 / Accepted: 10 March 2023 / Published online: 14 April 2023
© The Author(s) 2023

Abstract

The perineuronal nets (PNNs) are sugar coated protein structures that encapsulate certain neurons in the brain, such as parvalbumin positive (PV) inhibitory neurons. As PNNs are theorized to act as a barrier to ion transport, they may effectively increase the membrane charge-separation distance, thereby affecting the membrane capacitance. Tewari et al. (2018) found that degradation of PNNs induced a 25%-50% increase in membrane capacitance c_m and a reduction in the firing rates of PV-cells. In the current work, we explore how changes in c_m affects the firing rate in a selection of computational neuron models, ranging in complexity from a single compartment Hodgkin-Huxley model to morphologically detailed PV-neuron models. In all models, an increased c_m lead to reduced firing, but the experimentally reported increase in c_m was not alone sufficient to explain the experimentally reported reduction in firing rate. We therefore hypothesized that PNN degradation in the experiments affected not only c_m , but also ionic reversal potentials and ion channel conductances. In simulations, we explored how various model parameters affected the firing rate of the model neurons, and identified which parameter variations in addition to c_m that are most likely candidates for explaining the experimentally reported reduction in firing rate.

Keywords Perineuronal nets · Capacitance · Firing rate · PV cells · Fast-spiking interneurons · Multicompartment models of neurons

1 Introduction

The perineuronal nets (PNNs) are condensed structures of extracellular matrix that encapsulate the soma and proximal dendrites of among others parvalbumin positive (PV) inhibitory neurons in the brain (Fawcett et al., 2019). PNNs are composed of hyaluronan chains, to which chondroitin

sulphated proteoglycans (CSPGs) are attached. The CSPGs in PNNs are mainly aggrecan and brevican. Both hyaluronan and chondroitin sulfate are glycosaminoglycans, which are large, unbranched, strongly negatively charged sugar molecules. The CSPGs in the PNNs are cross-linked by tenascin-R. PNNs are long-lived, stable structures hypothesized to stabilize synapses and they have to be enzymatically cleaved to allow for synapse growth (van 't Spijker & Kwok, 2017). Furthermore, they are thought to act as a barrier to ion transport because of their massive negative charge (Morawski et al., 2015; Hanssen & Malthe-Sørensen, 2022).

Enzymatic degradation of PNNs induces a dramatic increase in plasticity in visual cortex (Pizzorusso et al., 2002) and reduces spiking activity of putative PV neurons *in vivo* (Balmer, 2016; Lensjø et al., 2017; Christensen et al., 2021). However, the mechanisms underlying these changes remain elusive. Some experimental studies find no significant differences in the electrophysiological properties of neurons with and without PNNs, using chondroitinase ABC treatment to degrade the PNNs (Dityatev et al., 2007; Pyka et al., 2011).

Action Editor: Emre Aksay

✉ Kine Ødegård Hanssen
hanssen.kine@gmail.com

- ¹ Department of Physics, University of Oslo, Oslo, Norway
- ² Centre for Integrative Neuroplasticity, University of Oslo, Oslo, Norway
- ³ Department of Biosciences, University of Oslo, Oslo, Norway
- ⁴ Institute of Basic Medical Sciences, University of Oslo, Oslo, Norway
- ⁵ Department of Physics, Norwegian University of Life Sciences, Ås, Norway

Tewari et al. (2018) performed *in vitro* measurements of capacitance and firing rate f under the presence of glutamate-releasing tumor GBM22 and non-glutamate releasing tumor GBM14, and found that matrix metalloproteinases (MMPs) released from the tumors disintegrated the PNNs, leading to a 25% increase in capacitance for the PNN-enwrapped interneurons and the 38% decrease in f seen in Fig. 1.

However, variability within their results implies that the change in capacitance in some instances could be up to 50%. As a control, they also showed that application of MMP-blocker GM6001 in the presence of tumor, resulted in normal behavior of the PNN-enwrapped neurons. In an attempt to reproduce the results *in vitro*, acute brain slices were treated with the bacterial chondroitinase-ABC (chABC) which degrades PNNs. Recording from the same neurons before and after chABC treatment showed an increased capacitance and decreased f . To complement their experimental findings, Tewari et al. performed simulations using a modified one-compartment version of the Hodgkin-Huxley (HH) model (as proposed by Abbott and Kepler (1990)). Similar to the experiments, the simulations showed that an increase in C_m resulted in a reduced f . However, the effect in the model was smaller than in their experiments (Tewari et al., 2018).

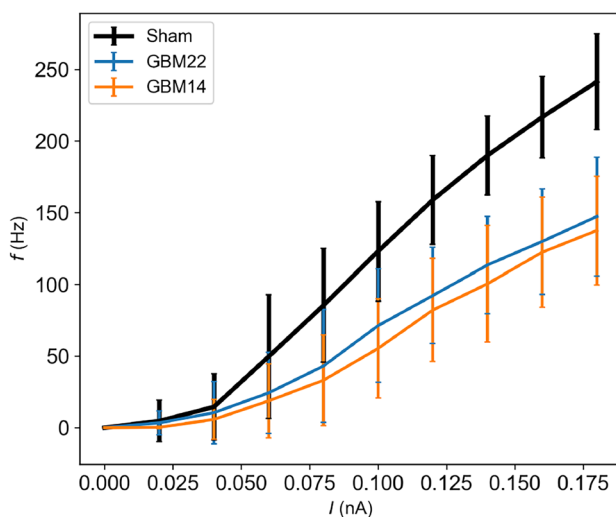


Fig. 1 Fast-spiking interneurons without perineuronal nets show reduced firing rate in experimental data from Tewari et al. (2018). Recordings were made from brain slices from mice injected with the following: Sham - phosphate-buffered saline, GBM14 - Non-glutamate releasing tumor, GBM22 - Glutamate-releasing tumor. Measurements were made on a minimum of seven neurons for each injection type. The tumors were shown to break down PNNs in their proximity. Firing rate f is plotted against input current I . The decrease in f was 38% from Sham to GBM22 and 41% from Sham to GBM14, as measured for the highest input current in the figure. The data were provided by Tewari et al. (2018)

Since the membrane is largely impermeable to ions, it acts as the dielectric in a capacitor which can separate a net positive charge (on one side) from a net negative charge (on the other side). PNNs have been suggested to act as an insulator that effectively acts to thicken the membrane, thereby decreasing C_m by increasing the distance between the exterior and interior membrane charges Tewari et al. (2018). This provides an explanation to why PNN degradation leads to an increased C_m in the experiments by Tewari et al. (2018). In principle, the insulating properties of PNNs might also lead to an increase in the membrane resistance R_m , but notable effects of PNN degradation on R_m were not found in the experiments by Tewari et al. (2018).

Since the membrane time constant τ_m is related to C_m by $\tau_m = R_m C_m$, a decrease in C_m (with a fixed R_m) will lead to a decrease in τ_m . As a decrease in C_m leads to a decrease in the membrane time constant and thereby to faster membrane dynamics, we might expect a decrease in C_m to increase the firing frequency f of the neuron. Likewise, we might expect an increase in C_m , e.g. due to degradation of PNNs, to reduce f . However, altering the time course of the membrane potential dynamics will also alter the complex interplay between various depolarizing and hyperpolarizing membrane currents through active ion channels. Hence, the relationship between C_m and f is not trivial, and will generally depend on the ion channels that a neuron possesses, as well as its input conditions (Szlavik, 2003; Wang et al., 2012).

The one-compartment HH model used by Tewari et al. has its limitations when it comes to modeling effects of PNN changes in PV neurons. Firstly, the HH model was constructed from measurements from the squid giant axon and does not encompass the properties of mammalian PV interneurons. It is common to distinguish between two types of excitability in neurons: Type I excitability, where the neuron can fire with arbitrarily low firing frequency close to the threshold current, and Type II, where firing increases abruptly from zero to a non-zero value when the threshold is reached. The HH model has Type II excitability. Thus, the HH model does not share the dynamical properties of the PV neurons in Tewari et al.'s experiments, whose $f - I$ curves displayed a Type I excitability (Sterratt et al., 2011).

Lastly, PNNs typically enwrap only the soma and proximal dendrites of PV neurons. Using a one-compartment model, one cannot account for such geometrical specificity, as one are forced to introduce the same changes in C_m over the neuron as a whole. Thus, the one-compartment HH model is not the best choice for capturing the firing characteristic of PV cells, for which there exist recent state-of-the-art multicompartment models.

In the present work, we perform a more systematic modeling study to explore possible mechanisms behind the reduction in f observed *in vitro* by Tewari et al. (2018). Similar results have also been observed *in vivo* (Balmer,

2016; Lensjø et al., 2017). To do this, we implement a range of models taken from the literature, including models constrained to electrophysiological data from PV cells. We find that in none of the models, the moderate capacitance changes observed in the experiments of Tewari and co-workers are sufficient to explain the measured changes in f , suggesting that PNN degradation also affects other cellular properties. We therefore expand the study, suggesting additional candidate mechanisms that may have contributed to the experimentally observed changes in f .

2 Methods

In the present study we try to explain the experiments by Tewari et al. (Fig. 1) in terms of changes in specific membrane capacitance c_m (capacitance per membrane area), conductance values \bar{g}_X for maximally open ion channels, and reversal potentials E_X for various ion channels X . The effects of these candidate mechanisms on the firing frequency f were studied in nine models, as presented in Table 1: a one-compartment HH model (OC), a ball-and-stick HH model (BAS) and three models developed by the Allen Institute for Brain science (A1, A2, A3). The multi-compartmental models come in two versions: one where c_m is varied everywhere (all), and one where c_m is varied only on the soma and proximal dendrites (sprx), as the PNNs are normally believed to encapsulate these parts of the neuron (Sorg et al., 2016). The proximal part of the dendrites was set to encompass every segment of the dendrite less than 3.5 soma lengths away from the cell body as measured by path distance along the neurites.

All models were based on a Hodgkin-Huxley type formalism, where the membrane potential dynamics in a given

compartment j (with membrane area A_j) is governed by the differential equation,

$$c_{m,j} \frac{dV_{m,j}}{dt} = -i_{L,j} - \sum_X i_{X,j} + \frac{I_{stim,j}}{A_j} + \frac{I_{j-1,j} - I_{j,j+1}}{A_j}. \quad (1)$$

Here, $I_{j-1,j}$ and $I_{j,j+1}$ represent incoming and outgoing axial currents, respectively, from neighboring compartments (relevant only for multicompartment models). Parameters affecting the axial currents explicitly were not changed in this project. The remaining currents are membrane current densities for the leakage channel

$$i_L = \bar{g}_L(V - E_L), \quad (2)$$

and various ion channels

$$i_X = \bar{g}_X m^\alpha h^\beta (V - E_X), \quad (3)$$

the assembly of which differed between the different models. In this general formalism, m and h are so-called gating variables, opening and closing the ion channels as a function of membrane potential and time, while α and β represent the number of gates of each type. Whereas these gating variables express genetically coded kinetics of the ion channel, \bar{g}_X represents the conductance when all channels of type X are fully open. E_X is the reversal potential for the ion channel of type X .

The Hodgkin-Huxley model contains conductances for sodium, potassium and a leak conductance. The Allen models incorporate six different potassium conductances, a voltage dependent-sodium conductance, two calcium conductances and a general cation conductance, along with a passive leak conductance. The calcium reversal potential E_{Ca} can change dynamically, as a function of intracellular calcium dynamics, which was explicitly accounted for in the Allen models.

Table 1 Models used in this study. OC is a one-compartment Hodgkin-Huxley model, BAS is a ball-and-stick model with passive dendrite and Hodgkin-Huxley mechanisms in the soma, and A1-A3 are three PV interneuron models developed by the Allen Institute for Brain Science constrained to morphological and electrophysiological data from real PV neurons. $c_{m,all}$ - c_m is changed everywhere, $c_{m,sprx}$ - c_m is changed only on the soma and proximal dendrites, Multicomp. - Multicompartment

Model	Multicomp.	HH	Allen	$c_{m,all}$	$c_{m,sprx}$
OC		✓		✓	
BAS, all	✓	✓		✓	
BAS, sprx	✓	✓			✓
A1, all	✓		✓	✓	
A2, all	✓		✓	✓	
A3, all	✓		✓	✓	
A1, sprx	✓		✓		✓
A2, sprx	✓		✓		✓
A3, sprx	✓		✓		✓

2.1 Implementation

Simulations with varying input currents, conductances, reversal potentials and specific capacitances were run in NEURON (Carnevale & Hines, 2006) with LFPy (Hagen et al., 2018) as a wrapper. Time and somatic membrane potential was written to file and analyzed using custom-made scripts. The time step of all simulations was set to $dt = 0.0078125$ ms, and all simulations were run for 600 ms before the recording started.

2.2 One-compartment model

The one-compartment model was simulated with the use of NEURON's built-in Hodgkin-Huxley mechanisms. The length and diameter of the one-compartment model was set to 10 μm .

2.3 Ball-and-stick models

The ball-and-stick models were constructed by connecting a soma compartment to a dendrite compartment in NEURON. The dendrite was divided into segments of 5 μm for the simulations. The diameter of the soma was 10 μm .

The dendrite length was set to $l = 1000 \mu\text{m}$ and the dendrite diameter to $d = 1 \mu\text{m}$. NEURON's HH mechanisms were inserted into the soma and passive mechanisms were inserted into the dendrite. The leak potential of the dendrite was set to -65 mV to match the resting potential of the soma, and the leak conductance was set to 0.0003 S/cm² in the dendrite. The axial resistivity R_a was set to 100 Ωcm .

2.4 Allen models

Mechanisms and morphologies of PV-neurons were taken from the Allen Brain Atlas' Cell Database (Allen Institute for Brain Science, 2022) and run in NEURON. Allen model 1, 2 and 3 are the perisomatic models (meaning that active conductances were only included in the soma compartment) of cells with CellID 471077857, 487667205 and 396608557, respectively. The Allen group removed all axon compartments and replaced them with an axon initial segment of 60 μm length and 1 μm diameter before performing the fit. For consistency, we used the same axon, giving it two compartments of two segments each.

The Allen models included the following mechanisms (Allen Institute for Brain Science, 2017):

- Hyperpolarization-activated cation conductance g_h
- Markov-style formulation Na⁺ channel conductance g_{NaV}
- K_v1-like K⁺ conductance g_{Kd}
- K_v2-like conductance g_{Kv2like}
- Fast-inactivating (K_v4-like) K⁺ conductance g_{KT}
- K_v3-like conductance g_{Kv3}
- M-type K⁺ conductance g_{Imv2}
- SK-type Ca²⁺-activated K⁺ conductance g_{SK}
- High-voltage-activated Ca²⁺ conductance g_{CaHVA}
- Low-voltage-activated Ca²⁺ conductance g_{CaLVA}
- A passive conductance g_L

The conductances were fit to experimental recordings by the Allen Institute for Brain Science and differed from model to model.

2.4.1 Changes in Nernst potentials

The reversal potential E_k of ion species k is

$$E_k = \frac{RT}{z_k F} \ln \frac{[k]_{\text{out}}}{[k]_{\text{in}}}, \quad (4)$$

where R is the gas constant, F is Faraday's constant, z_k is the valency and $[k]_{\text{in}}$ and $[k]_{\text{out}}$ are the intracellular and extracellular concentrations. In the Allen models, E_{Ca} varied dynamically through equations for calcium dynamics proposed by Destexhe et al. (1994) and Eq. (4), as Ca²⁺ currents affected the intracellular Ca²⁺ concentration. When we investigated hypothesized effects on E_{Ca} due to PNN degradation, we changed $E_{\text{Ca}}(t = 0)$ by specifying fixed changes in the extracellular Ca²⁺ concentration, which did not vary dynamically in the model.

2.5 Simulation protocol

Frequency-input ($f - I$) curves were computed by injecting constant currents of different amplitude into the soma. The current was increased in increments of 0.01 nA up to the value where the neuron was driven into depolarization block and was no longer able to fire action potentials. The input current duration was set to 1000 ms for the HH models. The Allen model neurons often exhibited late-onset spiking for current injections close to the threshold current. They were therefore stimulated by currents of 2000 ms duration, with the spiking frequency obtained from the last 1000 ms of the stimulus. The same protocol was used to find the threshold current, with a resolution of 0.001 nA. Spike frequencies and thresholds were found for sustained firing: Spikes were only counted if at least one spike occurred in the latter half of the stimulation interval, that is the last 1000 ms for the Allen models and the last 500 ms for the HH models. A spike was detected if the voltage at one point in time was larger than for both the preceding and the following time step, while also being larger than -20 mV.

3 Results

We studied how $f - I$ curves in the nine models described in the methods section were sensitive to a selection of model parameters, including the specific membrane capacitance c_m , maximal conductances \bar{g}_X for various ion channels, and ionic reversal potentials E_k .

3.1 Effects of c_m on firing properties

The firing properties of all models were sensitive to the value of c_m/c_{m0} , where c_{m0} is the model's default value of the capacitance. An example illustration is given in Fig. 2A showing the voltage trace of Allen model 1, where an increasing c_m lead to a broadening of the spikes, a lower spike amplitude and a decreased firing rate. The broadening was general for all models (Fig. 2E, F), as expected, since $c_m \propto \tau_m$ should slow down the membrane dynamics.

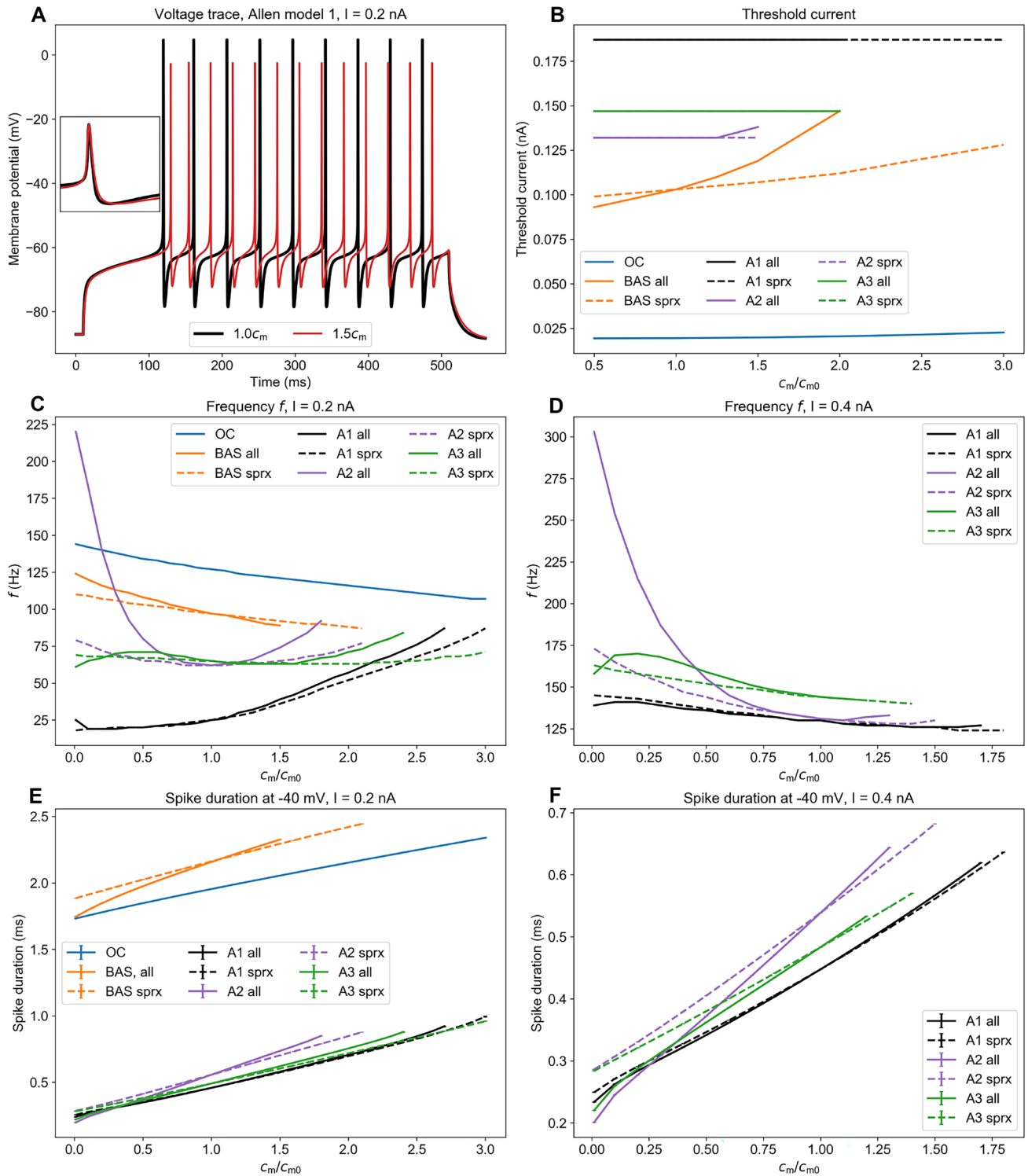


Fig. 2 Properties of the neuron model as a function of specific membrane capacitance c_m . c_{m0} is the default value of c_m in the model. **A** Voltage trace for Allen model 1 for default c_m and $1.5c_m$. Inset: normalized voltage trace over the duration of one peak. The two traces have been shifted to align the peak maxima, **B** Threshold current vs c_m , **C** Frequency f vs c_m for all models for input current $I = 0.2$ nA, **D** f vs c_m for the Allen models for $I = 0.4$ nA, **E** Spike duration

(defined as the width of the spike at -40 mV) for $I = 0.2$ nA, **F** Spike duration at -40 mV for $I = 0.4$ nA. Note that the one-compartment model and the ball-and-stick model do not fire for $I = 0.4$ nA. OC - one-compartment model, BAS - ball-and-stick model, A1 - Allen model 1, A2 - Allen model 2, A3 - Allen model 3, all - c_m changed at every segment of the neuron, sprx - c_m only changed at the soma and proximal dendrites

Note that the Allen models exhibit narrower spikes than the HH models, resembling the short spike duration observed in PV cells (Bartos & Elgueta, 2012).

The effect of c_m on the threshold current for firing onset is shown in Fig. 2B. The threshold current remained constant or varied only slightly with the capacitance, except for the ball-and-stick model. However, in none of the models the onset was shifted when varying c_m over the interval relevant under Tewari et al.'s experiments (i.e. from default to a factor 1.5 increase). This held both for simulations where c_m had only been altered in the soma and proximal dendrites, as indicated by dashed lines, and simulations where c_m was changed everywhere, as indicated by solid lines.

There was no clear general trend shared among the models in terms of how the firing frequency f depended on c_m . Over the same c_m interval, f increased with c_m in some models, while it decreased with c_m in others (Fig. 2C, D). This was also the case for the c_m interval relevant under the experiments by Tewari et al. However, for the strongest of the current injections considered (0.4 nA in Fig. 2D), all models except Allen model 2 (which stopped firing at $\sim 25\%$ increase in c_m) showed a decreasing trend in f with c_m . This suggests that at least the maximal firing rate in these models should be reduced, like in the experiments, when c_m is increased (as an effect of PNN degradation).

For all the Allen models, f vs c_m varied less when c_m was only changed in the soma and proximal dendrites, which is to be expected as we altered c_m on a smaller part of the neuron. For Allen model 3, for instance, this graph appeared far less curved when c_m was changed in the soma and the proximal dendrites compared to when c_m was changed everywhere. However, within the range $c_m/c_{m0} \in [1.0, 1.5]$, the difference between the two cases was relatively small. In the following, we therefore show results only for the supposedly more realistic case where PNN degradation is assumed to alter c_m only on the soma and proximal dendrites (results for c_m altered everywhere is found in Supplementary Fig. 1).

To compare with the $f - I$ curves of Tewari et al. (2018) (Fig. 1) we stimulated the different neuron models with a range of input currents for various values of c_m . Except for stimuli near the onset threshold, all models displayed a reduction in f when increasing c_m (Fig. 3).

In addition to affecting the firing rate, changes in c_m caused a shift in the spiking onset threshold in some of the models (Fig. 3). However, in none of the models the onset was shifted when varying c_m over the interval relevant under the Tewari et al.'s experiments.

The HH models (Fig. 3A, B) exhibited type II firing, meaning that the firing rate increases abruptly from zero to a higher value when the threshold current is reached. However, Tewari et al. observed Type I firing in their experiments. The HH models are therefore not ideal for simulating PV cells.

The Allen models, which were constructed based on morphological and electrophysiological recordings from real PV cells, had $f - I$ curves that were more similar to the experimental recordings. For Allen model 1 the firing frequency increased with c_m for input currents close to the threshold current (Fig. 3C). At an input current of around $I = 0.28$ nA, the $f - I$ curves crossed, after which the firing frequency decreased with c_m . For Allen model 2, the $f - I$ curve crossings started closer to the threshold current and were less pronounced (Fig. 3D). For a relatively larger range of input currents f decreased with increasing c_m . For Allen model 3, the firing frequency was approximately equal for all c_m for stimuli up to $I = 0.18$ nA, after which f started to decrease as c_m was increased (Fig. 3E).

None of the $f - I$ curves in Fig. 3 show a sufficient reduction in firing when reducing c_m by 25 or 50% to explain the observations in the experiments by Tewari et al. (as seen from Fig. 3G). In other words, changing c_m was on its own not enough to reproduce their findings. We therefore hypothesized that PNN degradation affected additional mechanisms which also contributed to the observed reduction in f . It has been reported that PNNs might affect both local concentrations of ions (Morawski et al., 2015; Burket et al., 2021) or currents through ion channels (Vigetti et al., 2008; van 't Spijker & Kwok, 2017). In the following sections, we have therefore explored how variations in reversal potentials E_k and ion channel conductances \bar{g}_X affect the firing frequency of our model neurons.

As the HH models contained relatively few of the membrane mechanisms present in PV neurons, and also produced type II firing unlike the type I firing seen in Tewari et al.'s experiments, we excluded them from our further analyses, and focused on the Allen models.

3.2 Effects of reversal potentials on firing rates

PNNs have been shown to be involved in the regulation of ionic concentrations (Morawski et al., 2015; Burket et al., 2017), and it is therefore likely that PNN degradation will lead to changes in ionic reversal potentials. This may in turn have dramatic consequences for neural firing properties, as has been the topic of many previous studies (Kager et al., 2000; Wei et al., 2014; Sætra et al., 2020). In order to gauge their general effect on the firing in PV neurons, all reversal potentials in the Allen models were changed separately by up to ± 20 mV, as shown in Fig. 4.

The simulations suggested that, among the reversal potentials, E_{Na} (all Allen models: Fig. 4A-C) and E_{Ca} (in Allen model 1: Fig. 4J) seemed the most likely candidates to have contributed during the experiments by Tewari et al. Both these led to moderate changes in the firing rate without strongly affecting the onset of firing. In contrast, changes in E_K and E_L (Fig. 4D-I) caused large shifts in firing onset not seen in the experiments, or no effect at all (Fig. 4H).

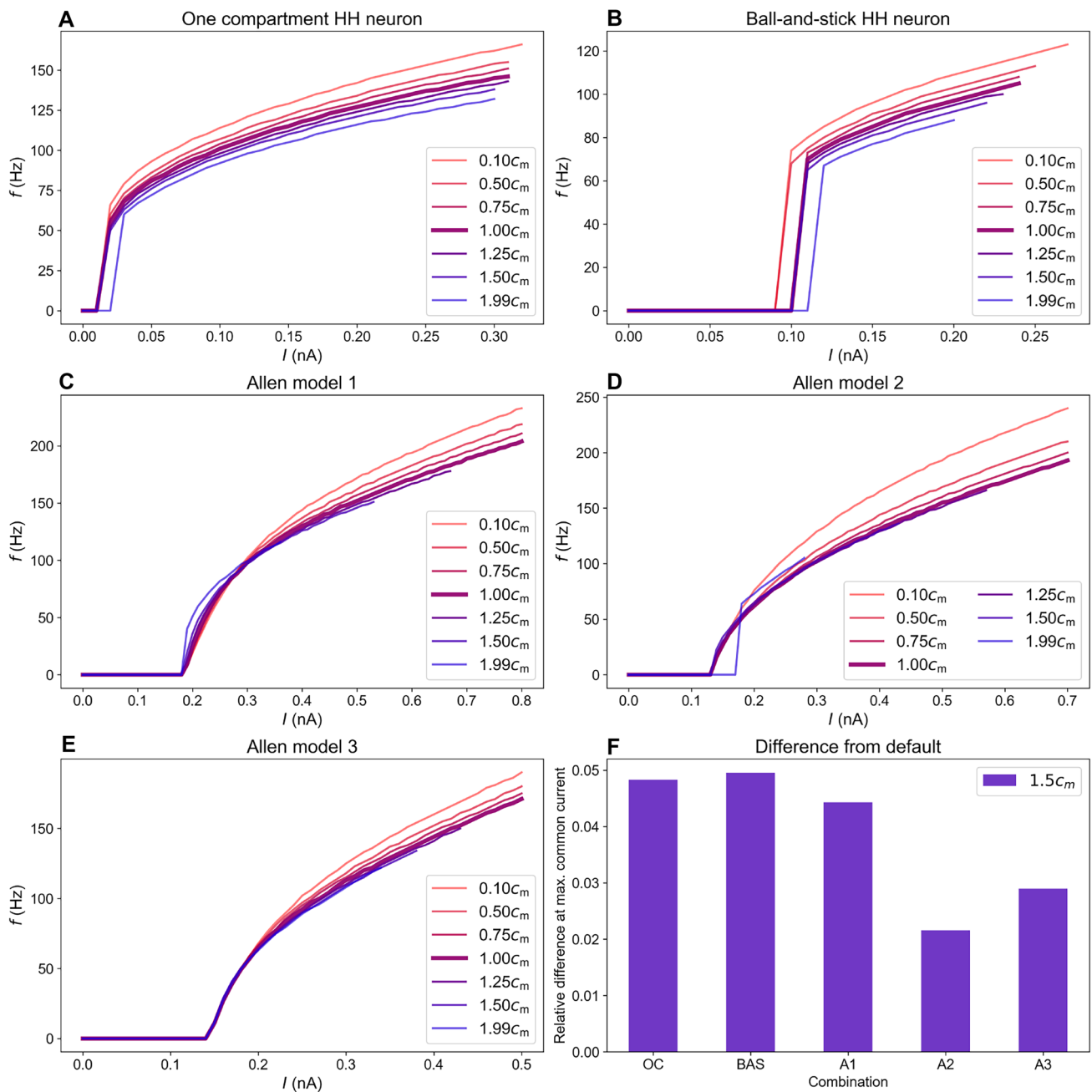


Fig. 3 Frequency-input curves for selected values of c_m for the various models. c_m is altered in the soma and proximal dendrites. **A** The one-compartment Hodgkin-Huxley model, **B** The ball-and-stick Hodgkin-Huxley model, **C** Allen model 1, **D** Allen model 2, **E** Allen

model 3, **F** The relative difference in f between the $1.0c_m$ - and $1.5c_m$ curves computed at the largest current that gave sustained firing in both cases

3.3 Effect of conductances on firing rates

To gauge the effect of conductance changes on $f - I$ curves, we varied all conductances one-by-one over an interval ranging from $0.3\bar{g}_X$ to $10.0\bar{g}_X$, where \bar{g}_X is the default maximal conductance (for fully open ion channels). Among the nine models, Allen model 1 responded most strongly to conductance changes. We therefore show results only for that model

(Figure 5). The effect of conductance on Allen models 2 and 3 is shown in (Supplementary Figs. 2 and 3).

3.3.1 Calcium conductances

In many neuron types, inward depolarizing Ca^{2+} currents trigger outward hyperpolarizing K^+ currents

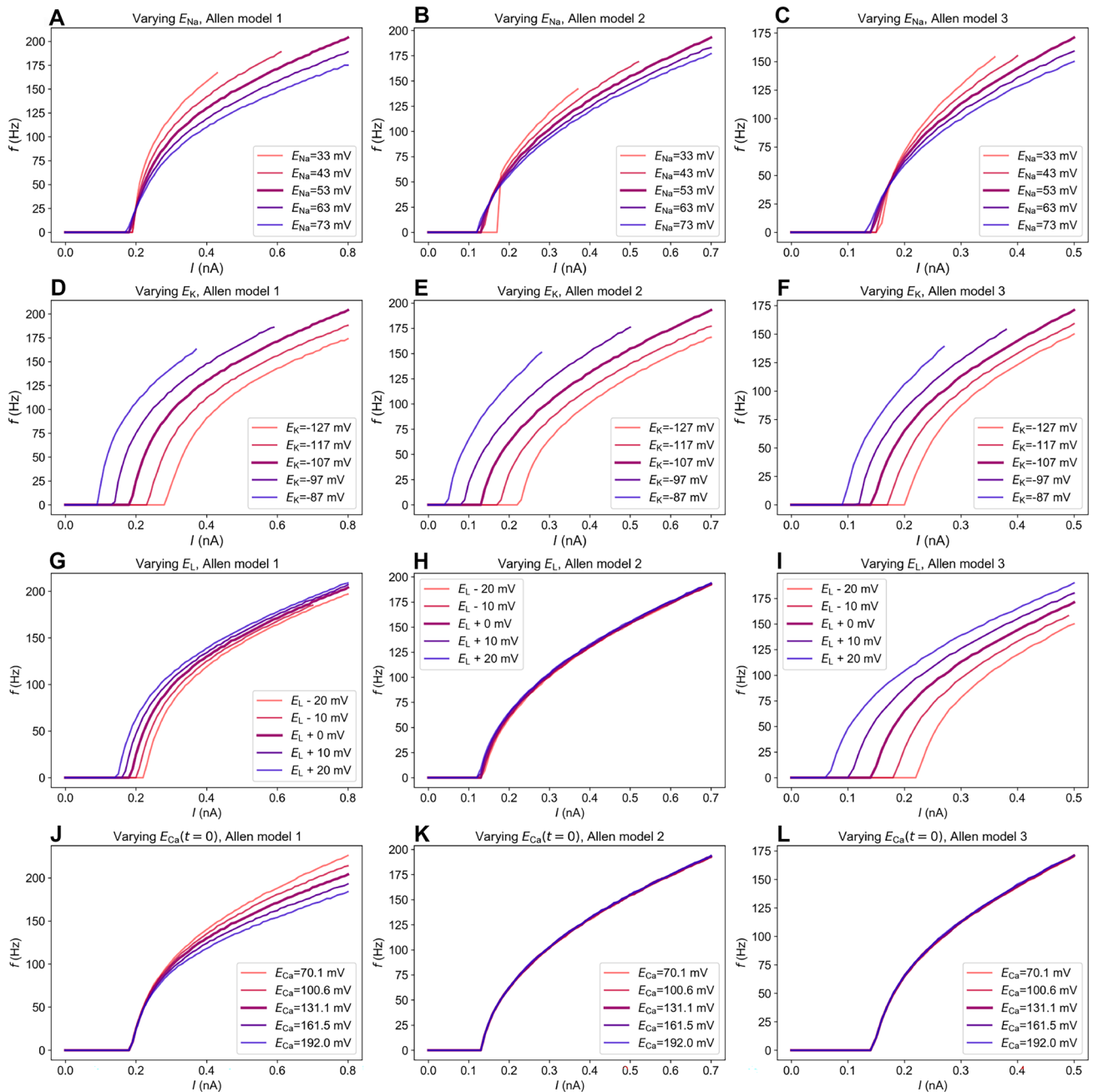


Fig. 4 Frequency-input curves when varying the different reversal potentials in the Allen models. Note that the reversal potential of calcium in the Allen models was found using calcium dynamics together with Eq. (4), so E_{Ca} is given at $t = 0$ ms and will vary throughout the simulations

through Ca^{2+} -activated K^+ channels (see e.g. Destexhe & Sejnowski (2003) or Hanes et al. (2011)). Hence, whether the overall effect of a Ca^{2+} current leads to an increased or decreased firing rate generally depends on the neuron's ion channel composition.

In Allen model 1, the direct depolarizing effect associated with inward Ca^{2+} currents was much smaller than the secondary hyperpolarizing effects associated with the activation of Ca^{2+} -activated SK channels. Increasing \bar{g}_{CaHVA} thus had

a negative effect on the firing rate in this model (Fig. 5A). Increasing \bar{g}_{CaHVA} by factors 3, 7 and 10, lead to quite pronounced decreases in f by 28%, 54% and 65%, respectively, at the maximal current injection considered (0.8 pA). In comparison, the decrease in f (at the maximal current injection) in Tewari et al.'s experiments was 38%. The increased conductance did not lead to a shift in the onset of firing. Likewise, reductions in f (without a shift in the onset threshold) could also be obtained by an increase in \bar{g}_{CaLVA} (Fig. 5B).

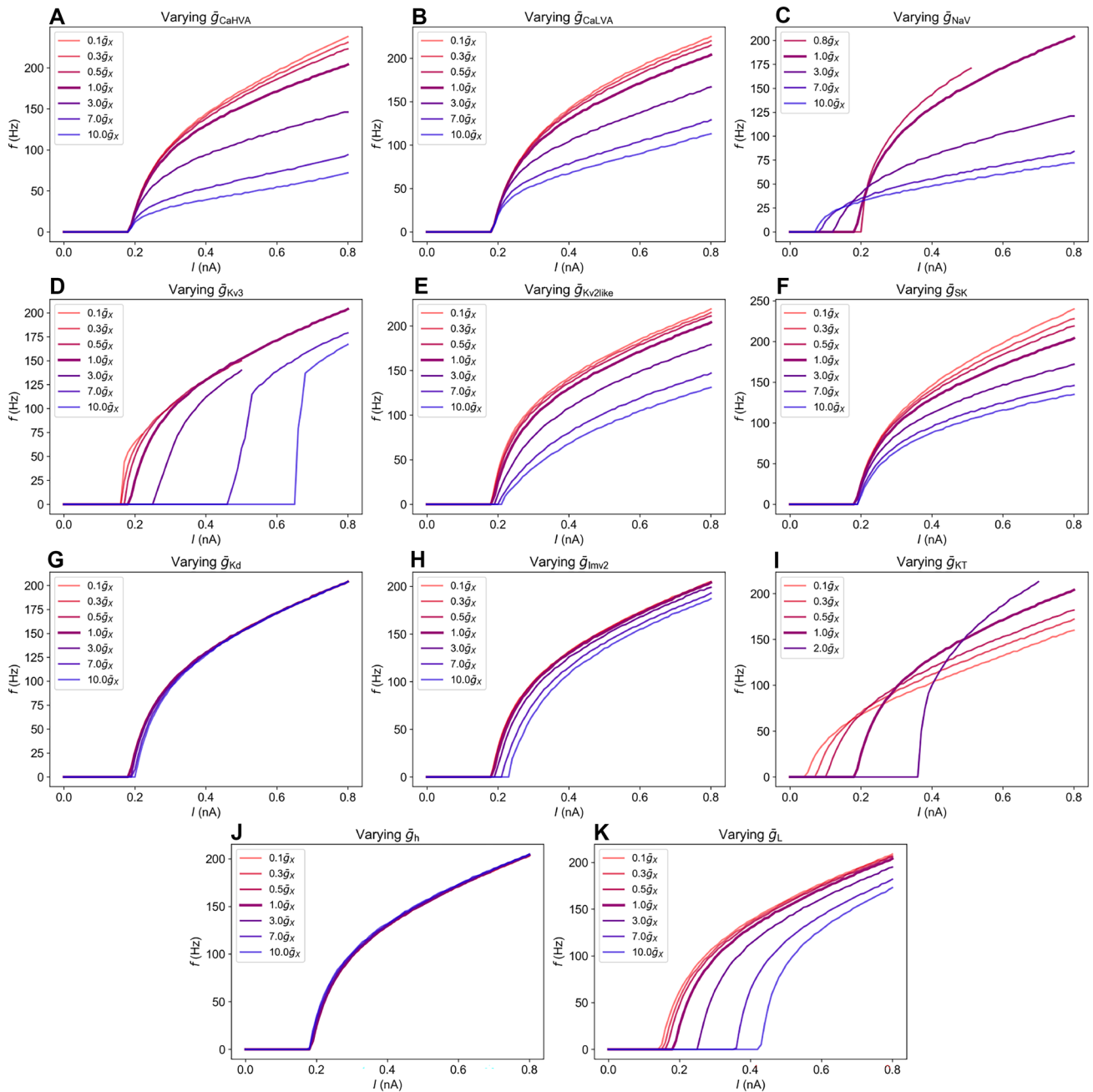


Fig. 5 Frequency-input curves when varying different conductances in Allen model 1. \bar{g}_x is the default value of the conductance. **A** \bar{g}_{CaHVA} , **B** \bar{g}_{CaLVA} , **C** \bar{g}_{NaV} , **D** \bar{g}_{Kv3} , **E** $\bar{g}_{Kv2like}$, **F** \bar{g}_{SK} , **G** \bar{g}_{Kd} , **H** \bar{g}_{Imv2} , **I** \bar{g}_{KT} , **J** \bar{g}_h , **K** \bar{g}_L

Combined with changes in c_m and possibly other mechanisms, \bar{g}_{CaHVA} and \bar{g}_{CaLVA} could be candidate mechanisms for explaining effects of PNN degradation on firing properties. However, we did not find experimental studies in support of the notion that PNN degradation should increase Ca^{2+} conductances. Contrarily, in retinal photoreceptors, chondroitin sulfates, which are key components of the PNNs, were found to shift the activation curve of unspecified calcium channels towards lower voltages (Vigetti et al., 2008). Hence, if

removing PNNs means removing chondroitin sulfates, we would expect activation to shift towards higher values, resulting in generally reduced calcium current I_{Ca} . Likewise, in experiments on hippocampal slices, (Kochlamazashvili et al., 2010) found that I_{CaHVA} was reduced upon breakdown of PNN component hyaluronan by hyaluronidase, and increased when hyaluronan was added to the hyaluronidase-treated neurons. If anything, the cited experiments thus suggest that PNN degradation should decrease overall calcium

currents, rather than increase them, as we needed to do to reduce f in Allen model 1. Hence, we do not consider \bar{g}_{CaLVA} or \bar{g}_{CaHVA} as main candidates for explaining Tewari et al.'s results.

We note that while \bar{g}_{CaHVA} had almost no effect on f in Allen models 2 and 3 (Supplementary Figs. 2A and 3A), increases in \bar{g}_{CaLVA} had a small positive effect on f in these models (Supplementary Figs. 2B and 3B). The latter suggests that in these models, the depolarizing effect of I_{CaLVA} dominated over indirect hyperpolarizing effects via SK activation. However, f was insensitive to reductions in \bar{g}_{CaHVA} and \bar{g}_{CaLVA} in these models. Hence, the decrease in f observed in Tewari et al.'s experiments could not be obtained by reducing Ca^{2+} conductances in any of the Allen models.

3.3.2 Sodium conductance

An increase in \bar{g}_{NaV} lead to a downward (towards lower input) shift in the onset of firing (Fig. 5C) in Allen model 1, and thus and increased f for weak stimuli. However, the $f - I$ curves for various \bar{g}_{NaV} crossed at about $I = 0.22$ nA, and for input stronger than this, increase in \bar{g}_{NaV} caused a decrease in f , as has been seen in a previous modeling study (Kispersky et al., 2012).

There is experimental support that PNNs affect NaV currents. Tenascin-C and net component tenascin-R have been found to play a crucial role in localizing NaV channels in the axon initial segment and nodes of Ranvier (Srinivasan et al., 1998), and tenascin-R has also been found to increase the maximum amplitude of NaV currents when in solution, thus indicating an increase in \bar{g}_{NaV} (Xiao et al., 1999).

As tenascin-R is a crosslinker in the nets, it is unclear whether it would get close enough to the NaV channels to affect them when present in intact PNNs. It is possible that removing the nets would lead to free tenascin-R and hence increased \bar{g}_{NaV} , but this effect might be transient due to diffusion of tenascin-R away from the cell surface. If tenascin-R lingers near the cell membrane after dissolving PNNs, a resulting increase in \bar{g}_{NaV} could, as we saw in Fig. 5C, partially explain the decrease in firing in Fig. 1. However, increases in \bar{g}_{NaV} produced pronounced shifts in the onset of firing not seen in the Tewari et al.'s experiments, and changes in \bar{g}_{NaV} thus does not seem like a main candidate for explaining the experiments.

3.3.3 Potassium conductance: \bar{g}_{Kv3}

Ion channel Kv3.1b is often highly expressed in PV neurons, which are often enwrapped in PNNs (Favuzzi et al., 2017). Experiments have also suggested that PNNs affect Kv3.1b channels. In brevicin knock-out mice, clustering of these

channels were altered, and active Kv3.1b was increased (Favuzzi et al., 2017). As PNNs contain brevicin, it thus seems natural to expect that PNN degradation should lead to an increase in Kv3.1b conductance and hence \bar{g}_{Kv3} .

The above evidence suggests that effects of PNN on \bar{g}_{Kv3} could be an important contributor to the reduction in f seen in Fig. 1. However, increasing \bar{g}_{Kv3} only gave a small reduction in f , but a pronounced shift towards higher input in the onset of firing (Fig. 5D), not seen in Tewari et al.'s experiments. According to the simulations, \bar{g}_{Kv3} is thus not a good candidate mechanism for explaining Tewari et al.'s experiments.

3.3.4 Potassium conductance: \bar{g}_{SK} and \bar{g}_{Kv2like}

Moderate and quite similar reductions in f could be obtained by increasing \bar{g}_{Kv2like} (Fig. 5E) and \bar{g}_{SK} (Fig. 5F). Neither of these mechanisms affected the onset of the $f - I$ curve significantly. The increase in \bar{g}_{SK} has experimental support, as attenuation of the extracellular matrix through application of chondroitinase ABC have been shown to upregulate SK-channels in hippocampal neurons, leading to an increase in I_{SK} by, on average, a factor 3 (see Fig. 2f in Dembitskaya et al. (2021)). When it comes to \bar{g}_{Kv2like} , we found no mention in the literature as to whether it is affected by PNNs. As the curves look promising and the literature does not exclude them, we consider both these conductances as candidate mechanisms for explaining parts of the reduction in f found in the experiments of Tewari et al.

3.3.5 Other potassium conductances

The K^+ conductances \bar{g}_{Kd} (Fig. 5G) and \bar{g}_{Imv2} (Fig. 5H) had little impact on f . Also, we have not found any mentions in the experimental literature suggesting that PNN affect these currents, and do not consider them as candidates for explaining Tewari et al.'s experiments.

In contrast, \bar{g}_{KT} induced a clear shift in the onset of firing, as seen from Fig. 5I. Its $f - I$ curves (for various values of \bar{g}_{KT}) crossed at different input currents. For low input currents, f decreased with increasing \bar{g}_{KT} , while for larger input currents f increased with decreasing \bar{g}_{KT} . Due to the relatively large shifts and lack of mention in the literature, we do not consider \bar{g}_{KT} as a main candidate for explaining Tewari et al.'s experiments.

3.3.6 \bar{g}_{h}

The hyperpolarization activated I_{h} current was almost inactive during the depolarizing current injections used in our simulations, and presumably also in Tewari et al.'s

experiments. Changing \bar{g}_h in Allen model 1 thus had almost no impact on its $f - I$ curves (Fig. 5J). Due to its low impact on the firing frequency, we conclude that \bar{g}_h is not a candidate mechanism for explaining the reduction in f found in Fig. 1. We note that chondroitin sulfates, which are present in PNNs have been found to shift the activation curve of I_h in photoreceptors (Vigetti et al., 2008), but PNNs were not found to have any effect on I_h in deep cerebellar nuclei (Hirono et al., 2018). As previously explained, we have focused on conductances of various channels, and have not tried to account for activation kinetics.

3.3.7 Leak conductance

A decrease in f could also be obtained by increasing the leak conductance \bar{g}_L (Fig. 5K). However, similarly to \bar{g}_{KT} , \bar{g}_L induced a clear shift in the onset of firing. Also, changes in the membrane resistance consistent with a change in \bar{g}_L were not found in the experiments by Tewari et al. (2018). We therefore do not consider \bar{g}_L as a main candidate for explaining Fig. 1.

3.4 A combinatorial explanation

In the experiments by Tewari et al. (2018), PNN degradation lead to a maximum reduction in c_m by 50%. As the simulations in Fig. 3G suggested, such a change in c_m did reduce the firing rate in fast-spiking interneuron, but not sufficiently to explain the experiments in Fig. 3G). The parameter explorations in Sections 3.2 and 3.3 allowed us to identify possible candidate mechanisms that, combined with the observed change in c_m , could explain the drop in f found in the experiments.

According to the simulations, \bar{g}_{Kd} , \bar{g}_{Imv2} and \bar{g}_h are unlikely candidates since they had close to no effect on the $f - I$ curve. The conductances \bar{g}_L , \bar{g}_{Kv3} and \bar{g}_{NaV} and the reversal potentials E_K and E_L are unlikely candidates since varying them introduced large shifts in the onset of the $f - I$ curves not observed by Tewari et al. $f - I$ curves resembling those in Fig. 1 could be obtained by upregulating the Ca^{2+} conductances \bar{g}_{HVA} and \bar{g}_{LVA} . However, such upregulations are in conflict with previous experimental studies suggesting that PNN degradation should rather lead to a down-regulation of the mechanisms in question. Ruling out the above parameters, we are left with four possible candidate mechanisms: the reversal potentials E_{Na} and E_{Ca} , and the conductances \bar{g}_{SK} and $\bar{g}_{Kv2like}$.

Upregulating the conductances \bar{g}_{SK} and $\bar{g}_{Kv2like}$, both present in the Allen PV cell models, had an effect on the $f - I$ curve similar to those seen in Fig. 1. Among these, upregulation of \bar{g}_{SK} by PNN degradation is supported by previous experiments, while we found no mention in the literature of PNN effects on $\bar{g}_{Kv2like}$. Likewise, increasing

E_{Na} and E_{Ca} also lead to the desired reduction in f . PNNs have been shown to accumulate cationic molecules and may provide ion sorting on neuronal membranes (Morawski et al., 2015; Burket et al., 2017). The notion that PNN degradation should affect ionic reversal potentials is thus not unlikely.

As shown in Fig. 6, the experiments of Tewari et al. could be explained through various combinations of changes in a selection of the parameters c_m , E_{Na} , E_{Ca} , $\bar{g}_{Kv2like}$ and \bar{g}_{SK} . Allen model 1 was chosen as that yielded the strongest responses to changes in parameters, and was therefore the most promising candidate for recreating the 38% average drop in f from Tewari et al.'s experiments.

In general, achieving a reduction in f similar to what was seen in Fig. 1 required quite large changes in several parameters, and a large increase in c_m was a necessary part of it. In Fig. 6, c_m was increased by a factor 1.5, E_{Ca} and E_{Na} (when included) were shifted by 30 and 10 mV, respectively, while $\bar{g}_{Kv2like}$ and \bar{g}_{SK} were varied (jointly, when both were included) by factors between 1.5 and 4 as indicated in the figure legends. Upregulation of \bar{g}_{SK} by such a high factor due to PNN degradation is supported by the experiments by Dembitskaya et al. (2021). It was there found that on average, \bar{g}_{SK} increased by a factor three after PNN degradation, but changes up to a factor six was within the standard deviation in the experimental data. For the remaining parameters, the literature gives no guidance as to whether PNN degradation should affect them in the way suggested in Fig. 6.

Not surprisingly, the largest effect on f was found when the full set of candidate mechanisms were changed in the same model. When $\bar{g}_{Kv2like}$ and \bar{g}_{SK} were increased by a factor four (relative to their default values in the model), the reduction in f exceeded that seen in Fig. 1.

4 Discussion

While an increasing number of studies show that degradation of PNNs increases plasticity (Fawcett et al., 2019), the underlying mechanisms remain elusive. An important piece of the puzzle is to reveal the role of PNNs for the neuron's electrophysiological properties. In the experimental paper by Tewari et al. (2018) it was shown that PNN degradation led to a 25–50% increase in the membrane capacitance c_m , and a decrease in the firing rate f of parvalbumin positive (PV) interneurons. In the current study, we showed for a selection of nine computational neuron models, that the reported reduction in c_m indeed lead to reduced f , but could not explain a reduction as large as that seen in the experiments. We therefore hypothesized that the reduction in f was due to a combination of cellular mechanisms affected by PNN degradation.

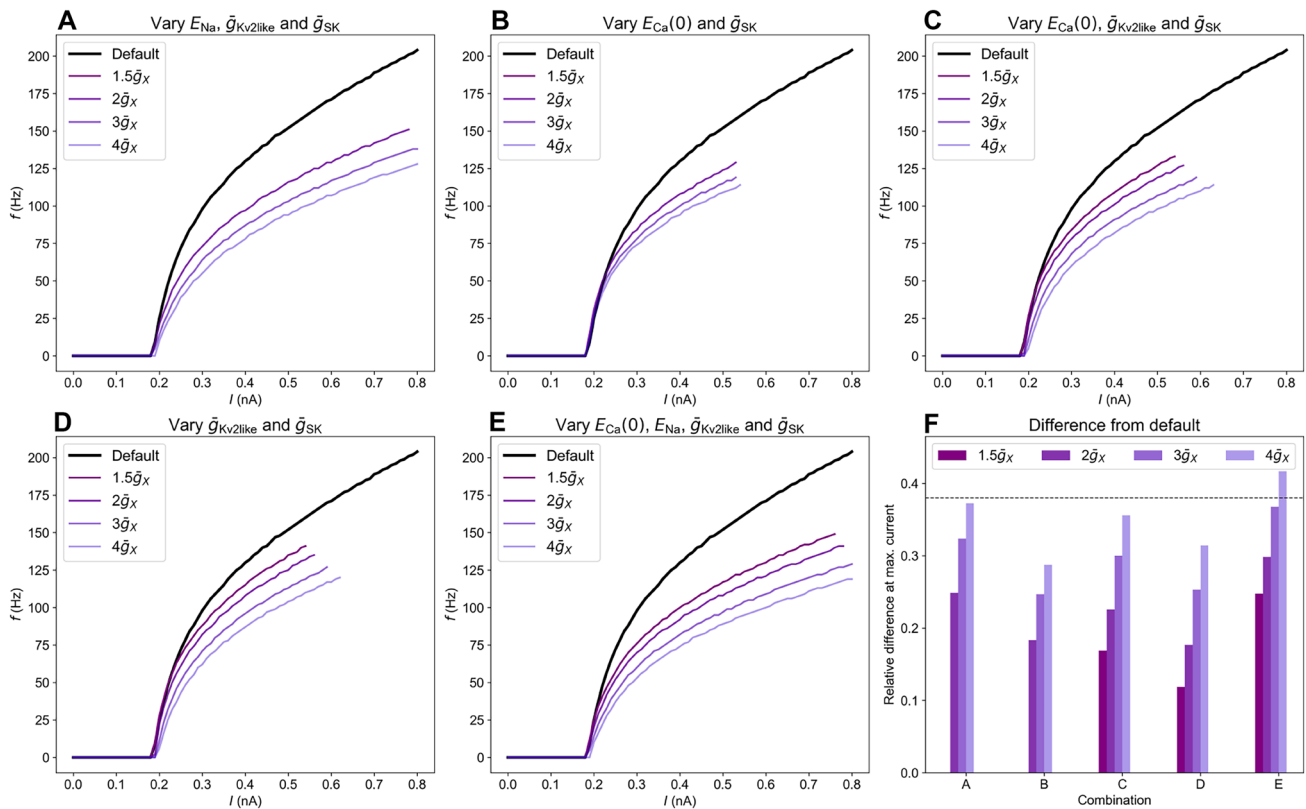


Fig. 6 Frequency-input curves of Allen model 1 when varying c_m and **A** E_{Na} , $\bar{g}_{Kv2like}$ and \bar{g}_{SK} , **B** $E_{Ca}(t=0)$ and \bar{g}_{SK} , **C** $E_{Ca}(t=0)$, $\bar{g}_{Kv2like}$ and \bar{g}_{SK} , **D** $\bar{g}_{Kv2like}$ and \bar{g}_{SK} , **E** $E_{Ca}(t=0)$, E_{Na} , $\bar{g}_{Kv2like}$ and \bar{g}_{SK} , **F** Relative difference between each parameter combination and default at the largest current that gave sustained firing in both cases. The horizontal dashed line indicate the relative difference between f of Sham

and GBM22 in Tewari et al.'s experiments. The difference between Sham and GBM14 is a bit larger. Default - default values, $E_{Na} = 53$ mV and $E_{Ca}(0) = 131.06$ mV. For the altered models, $E_{Na} = 63$ mV and $E_{Ca}(0) = 161.53$ mV, c_m is increased by a factor 1.5 and the conductances are indicated in the legend

By systematically exploring how f was reduced by changes in selected model parameters, we proposed an explanation where the reduced firing rate in Tewari et al.'s experiments is due to (1) the reported change in c_m combined with (2) upregulation of potassium channels \bar{g}_{SK} and $\bar{g}_{Kv2like}$, and (3) upward shifts in Ca^{2+} and Na^+ reversal potentials. Whereas the upregulation of \bar{g}_{SK} is supported by previous experimental data (Dembitskaya et al., 2021), the proposed effects of PNN degradation on the remaining parameters are neither supported nor conflicted by existing literature.

Experimental literature on how PNNs affect ion channels and reversal potentials is sparse. In the few studies that exist, the focus is often on how individual PNN components affect cell properties, and not on PNNs as an intact structure (see e.g. Xiao et al., (1999), or Favuzzi et al., (2017)). This opens up for speculation about how PNN degradation actually affects the cell. When we in the current study compared our model predictions with experimental findings, we assumed effects of net components were the same when embedded in the net as when applied artificially in a bath solution, and likewise that dissolving PNNs corresponds to degradation of all PNN

components. However, we cannot exclude the possibility that components of dissolved nets in reality will be floating around in the extracellular space, having the same (or even stronger) effect on cells as when embedded in the PNNs.

PNNs encapsulate neural membranes inhibiting the growth of new spines (Dansie & Ethell, 2011; Bikbaev et al., 2015). The impact on spine growth provides a quite simple explanation to the relationship between PNNs and \bar{g}_{SK} : PNN degradation would facilitate the growth of new spines, and as \bar{g}_{SK} are expressed in spines in many neurons, this could lead to a quite dramatic increase \bar{g}_{SK} expression (Dembitskaya et al., 2021). The mechanisms through which PNNs should affect the expression or kinetics of ion channels not primarily located in spines are less clear. For simplicity, we assumed that key effects of PNN degradation on ion channels could be modeled as up- or down regulation of conductances (for fully open channels). However, we note that in some cases, net components can have more complex effects on ion channels than mere up- or down-regulation. For instance, net components have been shown to alter the activation curves of Ca^{2+} channels (Vigetti et al.,

2008), and in principle, activation time constants could also be affected. Since there is little available data that would allow us to constrain PNN effects on ion channel kinetics, we made the simple choice of only varying the conductances. However, a more in-depth study of effects of PNN degradation on firing rates could be conducted when more data is available on how PNN degradation affects specific mechanisms on the cellular level.

An important feature of Allen model 1 (our selected “main model”) was that the effect on f by regulating Ca^{2+} conductances \bar{g}_{HVA} and \bar{g}_{LVA} was always indirect, i.e. via the activation of \bar{g}_{SK} by intracellular Ca^{2+} . The interplay between Ca^{2+} influx and the activation of Ca^{2+} activated K^+ channels such as SK is generally intricate (Sah & Faber, 2002; Shin et al., 2022), and we note that the Ca^{2+} conductances in our model could have the opposite effect if \bar{g}_{SK} were very small or absent in the model. In that case, f would decrease with decreasing Ca^{2+} conductances, and not increase, as it did in our simulations. This would reinstate the Ca^{2+} conductances as candidate mechanisms for firing frequency reduction, as a reduction in I_{Ca} and f has been found upon PNN degradation (Vigetti et al., 2008; Kochlamazashvili et al., 2010). As Allen model 1 instead leads us to suggest \bar{g}_{SK} as a key candidate mechanism for explaining reduced firing rates in the experiments of Tewari et al. (2018), we would encourage follow-up experiments aimed to verify this finding. Such experiments could for example use immunohistology or patch-clamping combined with SK antagonists or agonists to verify if (i) PNN degradation actually leads to a change in \bar{g}_{SK} in the relevant neurons, and (ii) whether \bar{g}_{SK} regulation actually causes pronounced changes in their firing rates.

The idea that PNNs should affect ionic reversal potentials seems plausible since PNNs consist of negatively charged glycans. It has been suggested that these locally immobilized charges can accumulate a reservoir of physiologically relevant cations such as K^+ , Na^+ and Ca^{2+} in the extracellular vicinity of PNN encapsulated neurons (Brückner et al., 1993; Morawski et al., 2015). However, it is not obvious how such a cation reservoir should affect the reversal potentials. One might imagine that the reservoir simply amounts to increased extracellular concentrations of free K^+ , Na^+ and Ca^{2+} , which would correspond to depolarized reversal potentials of these ions. Alternatively, one could imagine that the reservoir instead represents a buffering of these ions, hindering them in crossing the membrane, with the possible consequence of more hyperpolarized reversal potentials. So far, we have failed to find experimental evidence for either of the possibilities, and the link between PNN associated glycans and ionic concentrations appears to be anything but trivial. For example, PNN associated glycans have been found to decrease the intracellular Cl^- concentration, and not increase it, as one intuitively might expect based on their negative (extracellular) charge. As

a consequence, enzymatic digestion of glycans was found to depolarize the Cl^- -reversal potential E_{Cl} (Glykys et al., 2014). When it comes to reversal potentials of the other ion species, we have found no clear statements in the literature as to how PNNs should affect them. One might seek some evidence by exploring effects of PNNs on resting membrane potentials, which depend on the weighted reversal potential of all ions that the resting membrane is permeable to. However, PNN degradation has not been consistently found to alter resting membrane potentials in fast-spiking interneurons (Balmer, 2016; Tewari et al., 2018). The lacking impact on resting potentials implies that PNNs either have little impact on ionic reversal potentials, or that they by chance or evolutionary selection affect multiple reversal potentials in concert so that their net effects on the resting membrane is small. In this context, it should be noted that the resting membrane potential is by far most sensitive to E_{K} and E_{Cl} , while E_{Na} and especially E_{Ca} could in principle change quite a lot without affecting the resting membrane potential much (Hodgkin & Katz, 1949).

We note that PNN degradation is likely to impact many mechanisms besides those considered in the current study. PNNs can for example influence glycan-protein ligand interactions and accessibility to receptors on the neuronal surface (McRae et al., 2012), influence neuron-glia interactions (Carulli et al., 2016), synaptic transmission (Sonntag et al., 2018), and regulate PV expression in itself (Enwright et al., 2016), as might have possible effects on the dynamical properties of the affected neurons. Most of these off-target changes were in the experiments of Tewari et al. (2018) ruled out as the main explanatory effects behind changed firing-rate changes (Tewari et al., 2018), and neither of these effects were considered in the current modeling study.

In general, the parameter changes that affected $f - I$ curves in our models also affected shapes of their action potential shapes and $f - I$ curves is generally not trivial. The durations (or widths) of action potentials are in many studies reported to increase with firing frequency (see e.g. Bourque & Renaud (1985) or Stratton et al. (2012)), yet examples of the opposite can also be found (see e.g. Kispersky et al., (2012) or Halnes et al., (2019)). As demonstrated in Supplementary Fig. 4, (panels F–K) for the final set of candidate models (those in Fig. 6), the duration of the action potentials could in our simulations both increase and decrease with firing frequency, depending on position on the stimulus-current axis. However, the overall variations in the action potential-shape were quite moderate, and its relationship to the $f - I$ curves was not studied further here.

Finally, we note that all models are simplifications that are bound to lack some mechanisms present in the real systems. In that context, we note that the $f - I$ curves of fast-spiking interneurons in the Tewari data (Fig. 1) were more linear than the $f - I$ curves of any of our nine considered computational models, both

under in control conditions and after PNN-degradation. Hence, none of the models seem to accurately describe the firing properties of the cell type in the experiments, pointing to mechanisms lacking in the models. The ideal starting point for the study presented would thus be the construction of a new multicompartment neuron model, validated against electrophysiological data from the relevant neuron type under the same experimental conditions as in the experiments of Tewari et al. (2018). This would require a large modeling effort including collaboration with experimentalists willing to do the relevant recordings, and was regarded as being beyond the scope of the current study. We instead considered the morphologically detailed state-of-the-art models from the Allen Brain Atlas' Cell Database as the best candidate models for the neurons in question, as these had passive and active parameters fitted to electrophysiological data from PV neurons in mice, i.e., the same kind of neurons that were targeted in the experiments of Tewari et al. (2018).

Supplementary Information The online version contains supplementary material available at <https://doi.org/10.1007/s10827-023-00849-9>.

Acknowledgements We thank Dr. Bhanu Tewari for supplying us with the $f - I$ data.

Author contributions KØH: Conceptualization, Formal analysis, Methodology, Software, Validation, Visualization, Writing - original draft. SG: Conceptualization, Visualization, Writing - original draft. MF: Conceptualization, Writing - original draft. TH: Conceptualization, Writing - original draft. GTE: Project administration, Writing - original draft. TVN: Conceptualization, Methodology, Software, Supervision, Writing - original draft. GH: Conceptualization, Formal analysis, Methodology, Project administration, Supervision, Writing - original draft.

Funding Open access funding provided by University of Oslo (incl Oslo University Hospital) K{OH, SG, MF, TH: The Research Council of Norway (<https://www.forskningradet.no/en/>) grant no. 568117 (received by MF). GH, GTE, TVN: EU project (Horizon 2020) HBP SGA3 Grant agreement ID: 945539 (received by GTE).

Data availability The code used to produce and analyze the results in this paper is archived on Zenodo: <https://doi.org/10.5281/zenodo.7688284>. It is also available on GitHub: https://github.com/KineOdegardHanssen/NEURON_Allen_capacitance.

Declarations

Ethics approval Not applicable.

Conflicts of interest The authors have no competing interests to declare.

Open Access This article is licensed under a Creative Commons Attribution 4.0 International License, which permits use, sharing, adaptation, distribution and reproduction in any medium or format, as long as you give appropriate credit to the original author(s) and the source, provide a link to the Creative Commons licence, and indicate if changes were made. The images or other third party material in this article are included in the article's Creative Commons licence, unless indicated otherwise in a credit line to the material. If material is not included in the article's Creative Commons licence and your intended use is not

permitted by statutory regulation or exceeds the permitted use, you will need to obtain permission directly from the copyright holder. To view a copy of this licence, visit <http://creativecommons.org/licenses/by/4.0/>.

References

- Abbott, L. F., & Kepler, T. B. (1990). Model neurons: from Hodgkin-Huxley to Hopfield. In *Statistical mechanics of neural networks* (Springer). 5–18
- Allen Institute for Brain Science. (2017). Technical White Paper: Biophysical Modeling - Perisomatic. <http://help.brain-map.org/display/celltypes/Documentation>
- Allen Institute for Brain Science. (2022). Overview: Allen brain atlas: Cell types. <http://celltypes.brain-map.org/>
- Balmer, T. S. (2016). Perineuronal nets enhance the excitability of fast-spiking neurons. *eNeuro* 3. <https://doi.org/10.1523/ENEURO.0112-16.2016>
- Bartos, M., & Elgueta, C. (2012). Functional characteristics of parvalbumin- and cholecystokinin-expressing basket cells. *The Journal of Physiology* 590, 669–681. <https://onlinelibrary.wiley.com/doi/pdf/10.1113/jphysiol.2011.226175>
- Bikbaev, A., Frischknecht, R., & Heine, M. (2015). Brain extracellular matrix retains connectivity in neuronal networks. *Scientific Reports*, 5, 14527.
- Bourque, C., & Renaud, L. (1985). Activity dependence of action potential duration in rat supraoptic neurosecretory neurones recorded in vitro. *The Journal of Physiology*, 363, 429–439.
- Brückner, G., Brauer, K., Härtig, W., Wolff, J. R., Rickmann, M. J., Derouiche, A., et al. (1993). Perineuronal nets provide a polyanionic, glia-associated form of microenvironment around certain neurons in many parts of the rat brain. *Glia*, 8, 183–200.
- Burket, J. A., Webb, J. D., & Deutsch, S. I. (2021). Perineuronal nets and metal cation concentrations in the microenvironments of fast-spiking, parvalbumin-expressing gabaergic interneurons: relevance to neurodevelopment and neurodevelopmental disorders. *Biomolecules*, 11, 1235.
- Burket, J. A., Urbano, M. R., & Deutsch, S. I. (2022). Sugarcoated perineuronal nets regulate “GABAergic” transmission: Bittersweet hypothesis in autism spectrum disorder. *Clinical Neuropharmacology*, 40, 120–130. <https://doi.org/10.1097/WNF.0000000000000209>
- Carnevale, N. T. & Hines, M. L. (2006). *The NEURON Book* (Cambridge University Press). <https://doi.org/10.1017/CBO9780511541612>
- Carulli, D., Kwok, J. C., & Pizzorusso, T. (2016). [Dataset] Perineuronal nets and cns plasticity and repair.
- Christensen, A. C., Lensjø, K. K., Lepperød, M. E., Dragly, S. -A., Sutterud, H., Blackstad, J. S., et al. (2021). Perineuronal nets stabilize the grid cell network Nature. *Communications*, 12, 253. Number: 1 Publisher: Nature Publishing Group. <https://doi.org/10.1038/s41467-020-20241-w>
- Dansie, L. E., & Ethell, I. M. (2011). Casting a net on dendritic spines: the extracellular matrix and its receptors. *Developmental neurobiology*, 71, 956–981.
- Dembitskaya, Y., Gavrilov, N., Kraev, I., Doronin, M., Tang, Y., Li, L., et al. (2021). Attenuation of the extracellular matrix increases the number of synapses but suppresses synaptic plasticity through upregulation of sk channels. *Cell Calcium*, 96, 102406.
- Destexhe, A., Mainen, Z. F., & Sejnowski, T. J. (1994). Synthesis of models for excitable membranes, synaptic transmission and neuromodulation using a common kinetic formalism. *Journal of Computational Neuroscience* 1, 195–230. <https://doi.org/10.1007/BF00961734>
- Destexhe, A., & Sejnowski, T. J. (2003). Interactions between membrane conductances underlying thalamocortical slow-wave oscillations. *Physiological reviews*, 83, 1401–1453.

- Dityatev, A., Brückner, G., Dityateva, G., Grosche, J., Kleene, R., & Schachner, M. (2007). Activity-dependent formation and functions of chondroitin sulfate-rich extracellular matrix of perineuronal nets. *Developmental Neurobiology*, *67*, 570–588. <https://onlinelibrary.wiley.com/doi/pdf/10.1002/dneu.20361>
- Enwright, J. F., Sanapala, S., Foglio, A., Berry, R., Fish, K. N., & Lewis, D. A. (2016). Reduced labeling of parvalbumin neurons and perineuronal nets in the dorsolateral prefrontal cortex of subjects with schizophrenia. *Neuropsychopharmacology*, *41*, 2206–2214.
- Favuzzi, E., Marques-Smith, A., Deogracias, R., Winterflood, C. M., Sánchez-Aguilera, A., Mantoan, L., et al. (2017). Activity-dependent gating of parvalbumin interneuron function by the perineuronal net protein brevican. *Neuron*, *95*, 639–655. <https://doi.org/10.1016/j.neuron.2017.06.028>
- Fawcett, J. W., Oohashi, T., & Pizzorusso, T. (2019). The roles of perineuronal nets and the perinodal extracellular matrix in neuronal function. *Nature Reviews Neuroscience* *20*, 451–465. Number: 8 Publisher: Nature Publishing Group. <https://doi.org/10.1038/s41583-019-0196-3>
- Glykys, J., Dzhalal, V., Egawa, K., Balena, T., Saponjian, Y., Kuchibhotla, K., et al. (2014). Local impermeant anions establish the neuronal chloride concentration. *Science*, *343*, 670–675.
- Hagen, E., Næss, S., Ness, T. V., & Einevoll, G. T. (2018). Multimodal modeling of neural network activity: Computing LFP, ECoG, EEG, and MEG signals with LFPy 2.0. *Frontiers in Neuroinformatics* *12*.
- Halnes, G., Augustinaite, S., Heggelund, P., Einevoll, G. T., & Migliore, M. (2011). *A multi-compartment model for interneurons in the dorsal lateral geniculate nucleus*. *PLOS Computational Biology*, *7*, e1002160. Publisher: Public Library of Science. <https://doi.org/10.1371/journal.pcbi.1002160>
- Halnes, G., Tennøe, S., Haug, T. M., Einevoll, G. T., Weltzien, F.-A., & Hodne, K. (2019). A computational model for gonadotropin releasing cells in the teleost fish medaka. *PLoS Computational Biology*, *15*, e1006662.
- Hanssen, K. Ø., & Malthe-Sørensen, A. (2022). Perineuronal nets restrict transport near the neuron surface: A coarse-grained molecular dynamics study. *Frontiers in Computational Neuroscience*, *16*.
- Hirono, M., Watanabe, S., Karube, F., Fujiyama, F., Kawahara, S., Nagao, S., et al. (2018). Perineuronal nets in the deep cerebellar nuclei regulate GABAergic transmission and delay eyeblink conditioning. *The Journal of Neuroscience*, *38*, 6130–6144. <https://doi.org/10.1523/JNEUROSCI.3238-17.2018>
- Hodgkin, A. L., & Katz, B. (1949). The effect of sodium ions on the electrical activity of the giant axon of the squid. *The Journal of physiology*, *108*, 37.
- Kager, H., Wadman, W. J., & Somjen, G. G. (2000). Simulated seizures and spreading depression in a neuron model incorporating interstitial space and ion concentrations. *Journal of Neurophysiology*, *84*, 495–512.
- Kispersky, T. J., Caplan, J. S., & Marder, E. (2012). Increase in sodium conductance decreases firing rate and gain in model neurons. *Journal of Neuroscience*, *32*, 10995–11004.
- Kochlamazashvili, G., Henneberger, C., Bukalo, O., Dvoretskova, E., Senkov, O., Lievens, P. M. J., et al. (2010). The extracellular matrix molecule hyaluronic acid regulates hippocampal synaptic plasticity by modulating postsynaptic I-type Ca²⁺ channels. *Neuron* *67*, 116–128. <https://doi.org/10.1016/j.neuron.2010.05.030>
- Lensjø, K. K., Lepperød, M. E., Dick, G., Hafting, T., & Fyhn, M. (2017). Removal of perineuronal nets unlocks juvenile plasticity through network mechanisms of decreased inhibition and increased gamma activity. *The Journal of Neuroscience*, *37*, 1269–1283. <https://doi.org/10.1523/JNEUROSCI.2504-16.2016>
- McRae, P. A., Baranov, E., Rogers, S. L., & Porter, B. E. (2012). Persistent decrease in multiple components of the perineuronal net following status epilepticus. *European Journal of Neuroscience*, *36*, 3471–3482.
- Morawski, M., Reinert, T., Meyer-Klaucke, W., Wagner, F. E., Tröger, W., Reinert, A., et al. (2015). *Ion exchanger in the brain: Quantitative analysis of perineuronally fixed anionic binding sites suggests diffusion barriers with ion sorting properties*. *Scientific Reports*, *5*, 16471. <https://doi.org/10.1038/srep16471>
- Pizzorusso, T., Medini, P., Berardi, N., Chierzi, S., Fawcett, J. W., & Maffei, L. (2002). Reactivation of ocular dominance plasticity in the adult visual cortex. *Science*, *298*. <https://doi.org/10.1126/science.1072699>
- Pyka, M., Wetzel, C., Aguado, A., Geissler, M., Hatt, H., & Faissner, A. (2011). Chondroitin sulfate proteoglycans regulate astrocyte-dependent synaptogenesis and modulate synaptic activity in primary embryonic hippocampal neurons. *European Journal of Neuroscience* *33*, 2187–2202. <https://onlinelibrary.wiley.com/doi/pdf/10.1111/j.1460-9568.2011.07690.x>
- Sætra, M. J., Einevoll, G. T., & Halnes, G. (2020). An electrodiffusive, ion conserving Pinsky-Rinzel model with homeostatic mechanisms. *PLOS Computational Biology*, *16*, e1007661.
- Shin, J., Kovacheva, L., Thomas, D., Stojanovic, S., Knowlton, C. J., Mankel, J., et al. (2022). Cav1.3 calcium channels are full-range linear amplifiers of firing frequencies in lateral DA SN neurons. *Science Advances*, *8*, eabm4560
- Sorg, B. A., Berretta, S., Blacktop, J. M., Fawcett, J. W., Kitagawa, H., Kwok, J. C., et al. (2016). Casting a wide net: Role of perineuronal nets in neural plasticity. *The Journal of Neuroscience*, *36*, 11459–11468. <https://doi.org/10.1523/JNEUROSCI.2351-16.2016>
- Srinivasan, J., Schachner, M., & Catterall, W. A. (1998). Interaction of voltage-gated sodium channels with the extracellular matrix molecules tenascin-C and tenascin-R. *Proceedings of the National Academy of Sciences* *95*, 15753–15757. Publisher: Proceedings of the National Academy of Sciences. <https://doi.org/10.1073/pnas.95.26.15753>
- Sterratt, D., Graham, B., Gillies, A., & Willshaw, D. (2011). *Principles of Computational Modelling in Neuroscience* (Cambridge University Press), 1. edn.
- Szlovak, R. B. (2003). Strategies for improving neural signal detection using a neural-electronic interface. *IEEE Transactions on neural systems and rehabilitation engineering*, *11*, 1–8.
- Sah, P., & Faber, E. L. (2002). Channels underlying neuronal calcium-activated potassium currents. *Progress in neurobiology*, *66*, 345–353.
- Sonntag, M., Blosa, M., Schmidt, S., Reimann, K., Blum, K., Eckrich, T., et al. (2018). Synaptic coupling of inner ear sensory cells is controlled by brevican-based extracellular matrix baskets resembling perineuronal nets. *BMC Biology*, *16*, 1–18.
- Stratton, P., Cheung, A., Wiles, J., Kiyatkin, E., Sah, P., & Windels, F. (2012). Action potential waveform variability limits multi-unit separation in freely behaving rats. *PLoS One*, *7*, e38482.
- Tewari, B. P., Chaunsali, L., Campbell, S. L., Patel, D. C., Goode, A. E., & Sontheimer, H. (2018). Perineuronal nets decrease membrane capacitance of peritumoral fast spiking interneurons in a model of epilepsy. *Abstract Nature Communications*, *9*(1). <https://doi.org/10.1038/s41467-018-07113-0>
- van 't Spijker, H. M., & Kwok, J. C. F. (2017). A sweet talk: The molecular systems of perineuronal nets in controlling neuronal communication. *Frontiers in Integrative Neuroscience* *11*. <https://doi.org/10.3389/fnint.2017.00033>
- Xiao, Z.-C., Ragsdale, D. S., Malhotra, J. D., Mattei, L. N., Braun, P. E., Schachner, M., et al. (1999). Tenascin-R is a functional modulator of sodium channel β subunits. *Journal of Biological Chemistry* *274*, 26511–26517. <https://doi.org/10.1074/jbc.274.37.26511>
- Vigetti, D., Andriani, O., Clerici, M., Negrini, D., Passi, A., & Moriondo, A. (2008). Chondroitin sulfates act as extracellular gating modifiers

- on voltage-dependent ion channels. *Cellular Physiology and Biochemistry*, 22, 137–146. Publisher: Karger Publishers. <https://doi.org/10.1159/000149791>
- Wang, L., Liu, S., Zhang, J., & Zeng, Y. (2012). Burst firing transitions in two-compartment pyramidal neuron induced by the perturbation of membrane capacitance. *Neurological Sciences*, 33, 595–604.
- Wei, Y., Ullah, G., & Schiff, S. J. (2014). Unification of neuronal spikes, seizures, and spreading depression. *Journal of Neuroscience*, 34, 11733–11743.

Publisher's Note Springer Nature remains neutral with regard to jurisdictional claims in published maps and institutional affiliations.

Paper III

An Updated Suite of Viral Vectors for *in vivo* Calcium Imaging Using Intracerebral and Retro-orbital Injections in Male Mice



An updated suite of viral vectors for in vivo calcium imaging using intracerebral and retro-orbital injections in male mice

Received: 10 March 2022

Accepted: 26 January 2023

Published online: 04 February 2023

 Check for updates

Sverre Grødem^{1,2}, Ingeborg Nymoen ^{1,2}, Guro Helén Vatne¹,
Frederik Sebastian Rogge¹, Valgerður Björnsdóttir¹,
Kristian Kinden Lensjø ^{1,3} ✉ & Marianne Fyhn^{1,3}

Genetically encoded Ca²⁺ indicators (GECIs) are widely used to measure neural activity. Here, we explore the use of systemically administered PHP.eB AAVs for brain-wide expression of GECIs and compare the expression properties to intracerebrally injected AAVs in male mice. We show that systemic administration is a promising strategy for imaging neural activity. Next, we establish the use of EE-RR- (soma) and RPL10a (Ribo) soma-targeting peptides with the latest jGCaMP and show that EE-RR-tagged jGCaMP8 gives rise to strong expression but limited soma-targeting. In contrast, Ribo-tagged jGCaMP8 lacks neuropil signal, but the expression rate is reduced. To combat this, we modified the linker region of the Ribo-tag (RiboL1-). RiboL1-jGCaMP8 expresses faster than Ribo-jGCaMP8 but remains too dim for reliable use with systemic virus administration. However, intracerebral injections of the RiboL1-tagged jGCaMP8 constructs provide strong Ca²⁺ signals devoid of neuropil contamination, with remarkable labeling density.

The use of microscopy to measure the activity of neurons is widely applied in modern neuroscience. With the development of genetically encoded Ca²⁺ indicators (GECIs) there have been rapid advances in response kinetics, sensitivity, and brightness of Ca²⁺ sensors (e.g.,^{1–3}), of which the GCaMP sensors are the most prominent. These engineered proteins contain a Ca²⁺-binding motif and a circularly permuted green fluorescent protein that brightens when Ca²⁺ is present. Using GECIs for activity measurements allows for cell-type targeted recordings, repeated measurements of the same cells for up to several months, and recordings from large populations of neurons. Ideally, GECIs should be uniformly expressed across the neuronal population with sufficient activity-dependent sensitivity and fluorescence range for in vivo applications. Overexpression in a subset of cells can lead to intracellular aggregation of GCaMP which can affect cellular function, and ultimately lead to cell death.

Various methods to introduce genetic constructs into cells have been explored. An often-preferred method for introducing GECIs into neurons is using transgenic animal models that are genetically

modified to express the desired construct (e.g.,^{4–6}). These models allow for strong, evenly distributed, and sustained expression throughout the animal's life and can be targeted to specific cell types. However, transgenic GCaMP mice require intricate and costly breeding schemes, both financially and for animal welfare. Furthermore, they depend on driver lines that prevent the simultaneous use of other transgenics³, thus limiting experimental flexibility. Moreover, since the GECIs are expressed throughout development, this may account for the frequent ictal activity that has been reported for several such mouse strains⁷, questioning their reliability for measurement of neuronal activity. Finally, relying on transgenic GECI-expressing lines limits the opportunity to adopt new and improved GECIs as they become available. New GECIs with faster kinetics and higher sensitivity or different excitation/emission wavelengths are frequently published, while developing transgenic lines takes considerably longer, and adopting new lines comes with substantial costs.

An alternative strategy is to deliver GECIs to neurons using a viral vector, which, in contrast to transgenic lines, allows for complete

¹Center for Integrative Neuroplasticity, Department of Bioscience, University of Oslo, Oslo, Norway. ²These authors contributed equally: Sverre Grødem, Ingeborg Nymoen. ³These authors jointly supervised this work: Kristian Kinden Lensjø, Marianne Fyhn. ✉ e-mail: kristian.lensjo@ibv.uio.no

flexibility in the adoption of alternative GECI constructs. In the brain, viral vectors encoding GECIs can be delivered by way of an intracerebral (IC) injection directly into the tissue of interest (e.g.,⁸) or cerebral ventricles⁹. However, IC injections of viral vectors tend to lead to highly variable expression depending on the concentration of virus particles and are often associated with cell damage or death¹⁰. Furthermore, using adeno-associated virus (AAV) serotype 9 which crosses the blood-brain-barrier¹¹ in neonatal mice, GECIs may be administered systemically through an intravenous injection into the tail -or temporal vein¹², or the transverse sinus¹³. However, these administration techniques are technically challenging, and come with a high risk of overexpression of the GECI because of the young age at the time of injection, and extended period from injections to experiments which may lead to cell damage or ictal events.

In contrast to AAV9, the recently developed AAV serotype PHP.eB crosses the blood-brain barrier in adult animals and efficiently transduces neurons across the brain¹⁴, suggesting that genes can be delivered via intravenous injections¹⁵. Importantly, such injections can be performed at any stage of development and thus prevent accumulation of GECIs and disturbances to Ca²⁺ homeostasis during sensitive parts of development. Moreover, this would enable brain-wide expression of the GECI in combination with transgenic models for e.g. cell-type specific activity perturbations. In contrast to the tail vein and other intravenous injection procedures, injections into the retro-orbital (RO) sinus can be performed with only limited training. RO injections are quick, non-invasive, and impose little stress on the animals compared to other methods¹⁶.

With the recent development of new GECIs and methods to restrict expression to parts of the cell, in combination with alternative delivery methods, there is need for a systematic assessment of these approaches. Here, we present a screening of multiple GECI constructs in mice comparing the RO injection method for systemic viral delivery with IC injections in primary visual cortex (V1), and assess functionality of the GECIs using wide-field and two-photon laser-scanning microscopy. We screen both widely used GECIs, such as GCaMP6f, and recently developed GECIs with improved sensitivity and kinetics³ (jGCaMP8s and jGCaMP8m). We show that several modern GECIs are highly suitable for systemic administration and give rise to uniform and stable expression for many weeks, and can readily be combined with other transgenic models for e.g., cell-specific expression of optogenetic or chemogenetic receptors. Because of the high brightness and sensitivity of jGCaMP8s, we also apply EE-RR- and ribosome-targeting peptides, where GECI localization is restricted to the soma, in order to limit neuropil signal^{17,18}. Ribosome-tethered (RLIO) jGCaMP8 provided highly selective expression in the cell soma and showed remarkable density of cell labeling for two-photon imaging, but the expression rate was substantially reduced compared to EE-RR soma targeting and non-soma-targeted GECIs. To circumvent this issue, we screened three different linker peptides in an effort to improve expression rate. One of these linker peptides, a long and flexible GS repeat linker, provided strong expression just one week after intracerebral injection. The ribosome-tethered construct with a modified linker, Ribol1-jGCaMP8, is both rapidly expressed and is all but completely excluded from neuropil.

Results

In order to compare the performance of GECI variants with different administration methods, we initially screened the performance of 10 existing GECI variants administered by RO or IC injections in high titer PHP.eB serotype AAVs, all expressed under a synapsin promoter. Pairs of mice were randomly assigned a GECI-expressing AAV and evaluated every two weeks for 2.5 months using wide-field and two-photon imaging through a cranial window. Expression of the GECIs were confirmed by post-mortem immunohistological inspection (Figs. 1a–c, S1, S2). In vivo imaging was performed in awake, head-fixed mice

running freely on a running wheel. We collected imaging data during periods of spontaneous activity (in darkness) or during presentation of visual stimuli (drifting sinusoidal gratings) for all GECIs tested. We mainly focused the two-photon imaging to layer 2/3 neurons at a depth of approximately 150–200 μm below the cortical surface, but images were also captured from deeper layers (3–400 μm , Fig. 1d) to assess expression levels across layers. The example images and analysis shown in the following section are based on data collected during spontaneous activity, unless described otherwise.

Of the GECIs included in our initial screening (Table 1), which are all variations of GCaMP, most have been widely used with IC injections in previous work. We confirmed detectable expression at reasonable laser power (40–50 mW output power at the front aperture of the objective at 920 nm) when administering the GCaMPs with IC injections with the PHP.eB serotype. However, following systemic virus administration, the majority of these GECIs were not sufficiently bright for in vivo Ca²⁺ imaging (Fig. 2a, Table 1). The most widely used GECI, GCaMP6f, was undetectable using reasonable laser power when expressed from an RO injection. At 6 weeks post injection, GCaMP6f was detectable, but only at very high laser power (>140 mW output at the objective) which would not be sustainable for functional experiments (Fig. 2a). Moreover, jGCaMP8f, which is reported to be brighter than previous “fast” iterations, was also not sufficiently bright for in vivo imaging when administered systemically. In an attempt to improve the brightness, we both doubled and tripled injection volumes of RO administered GCaMP6f and jGCaMP8f, but the resulting expression was still too dim to image at reasonable laser power (in vivo data for triple injection volumes were of similar brightness to the image of GCaMP6f shown in Fig. 2a, histology shown in Fig. 2b, c). Of the more recently developed GECIs; jGCaMP7s, jGCaMP8s, and jGCaMP8m were all sufficiently bright for use with RO-injected viruses (Figs. 1c and 2a, Supplementary Video 1), i.e., single-cell Ca²⁺ transients were detectable at reasonable laser power (40–50 mW). Of these, jGCaMP7s displayed the lowest neuropil signal but also the slowest response kinetics, the latter in line with earlier reports². Encouragingly, none of the GECIs we tested by RO injection showed signs of ictal activity (measured by wide-field fluorescence imaging, example data shown in Fig. S1), contrasting previous reports in transgenic GECI-expressing mice⁷.

Importantly, post-mortem histological analysis indicated that brightness of the GECI was the determining factor for whether a GECI was detectable in vivo, as the expression of GCaMP when labeled with a GFP antibody was comparable between GECIs with very different in vivo performance (Figs. 2b and S3a–c). Overall, the histology and in vivo imaging matched previous reports on PHP.eB infection¹⁹, both with respect to the expression pattern across the cortex and that the highest density was found in cortical layer 5 (Figs. 1d, 3a, S2 and S3). This was true for the visual cortex, somatosensory, retrosplenial, and motor cortex (Fig. S2). In the hippocampus, we observed only sparse labeling, apart from very dense labeling in area CA2 (Figs. S2 and S3). We also confirmed expression in the spinal cord (Fig. S2, lower panel).

While sufficient brightness for imaging is a requirement for any GECI to be viable, there are many factors to consider when selecting the optimal sensor for a given experiment. The newer iterations of GCaMP feature improved kinetics and higher sensitivity relative to previous versions. However, higher sensitivity may also affect the signals detected from neuronal processes such as dendrites, which can both disturb the quantification of Ca²⁺ transients from the cell soma and reduce the number of cells one can record from by introducing noise. Recent efforts have attempted to alleviate these effects by restricting the expression of the GECI to the cell soma^{17,18}, but it is unclear how the soma-specificity and efficiency are affected by brain-wide expression of the brighter iterations of jGCaMP. We therefore applied two main soma-targeting strategies using jGCaMP8 and compared their performance with IC and RO-injected viruses.

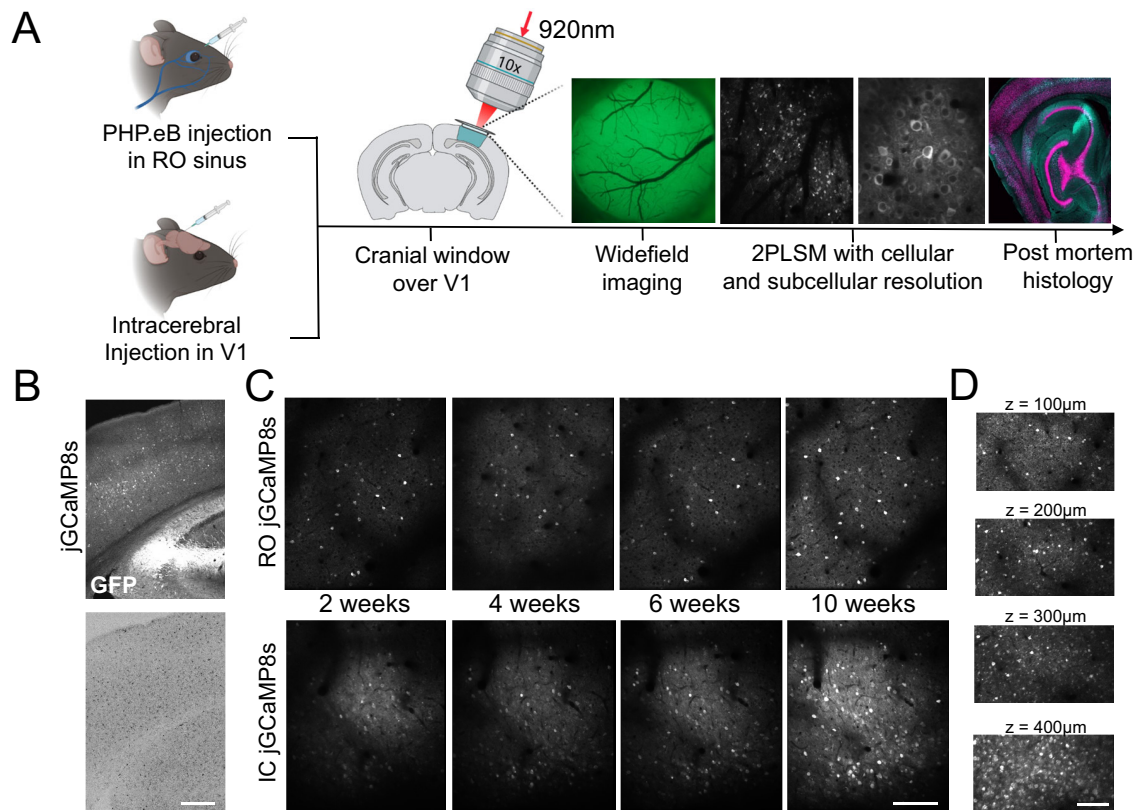


Fig. 1 | Systemic and local administration of GECIs using PHP.eB AAVs.
A Experimental overview indicating the two injection methods, and the approaches used to monitor the expression. Illustration created with Biorender.com. **B** Post-mortem histological verification of jGCaMP8s expression 10 weeks after RO injection and microglia activation verified by Iba1-positive labeling. Scale bar indicates

200 μm . **C** Example images from in vivo two-photon microscopy of jGCaMP8s expressed by RO or IC virus injections 2, 4, 6, and 10 weeks after injection. Scale bar indicates 200 μm . **D** GECI expression at different depths in cortex after RO injection of jGCaMP8s. Scale bar indicates 150 μm .

We first constructed EE-RR tagged versions of the jGCaMP8 variants that showed functional expression levels after systemic virus injection (jGCaMP8m and s). 2–4 weeks post RO injection, the EE-RR-jGCaMP8 was comparably bright to the unaltered jGCaMP8 but had limited effects on the localization to neuropil (Figs. 3a, S3,

Supplementary Video S2 and 3). Similar to the RO-injected animals, we observed strong signals from both EE-RR and regular jGCaMP8 after IC injections with comparable neuropil signals (Fig. 3b, Supplementary Video S4).

Table 1 | Overview of initial GECI screening with virus titer and Addgene reference indicated

GECI	Titer (VG/ml)	Detectable at 50 mW (RO injection)	Addgene plasmid #
GCaMP6f	2.44E+13	No	100837
EE-RR- GCaMP6f	2.04E+13	No	158756
jGCaMP7f	2.04E+13	No	104488
EE-RR- GCaMP7f	1.53E+13	No	158760
jGCaMP7s	1.11E+13	Yes	104487
jGCaMP8f	1.04E+13	No	162376
jGCaMP8m	9.43E+12	Yes	162375
jGCaMP8s	1.49E+13	Yes	162374
jREX-GECO1	9.36E+12	Yes	169259 ^a
Ribo-GCaMP6m	1.86E+13	No	158777
CAG-mNeonGreen	1.09E+13	Yes	99134

^ajREX-GECO1 expressed from a hSyn promoter was made and used in this manuscript. All constructs were tested and confirmed viable for imaging using IC injections (with the exception of Ribo-GCaMP6m, where we did not observe in vivo expression). “Detectable at 50 mW (RO injections)” is defined as whether a single imaging plane using a 16 \times Nikon objective and 50 mW laser power at 920 nm gives clear single-cell fluorescence transients 6 weeks after injection. The fluorescent protein mNeonGreen expressed under a CAG promoter was used as a positive expression control for the RO injection method.

In comparison to EE-RR soma targeting and other non-soma-targeted GECIs, ribosome-tethered (RPL10a) GCaMP expression has been reported to drastically reduce the brightness of the attached GCaMP¹⁷, demanding high laser intensity for in vivo imaging. In contrast to EE-RR, Ribo-GCaMP localization is strictly confined to the soma. We therefore constructed Ribo-jGCaMP8m and Ribo-jGCaMP8s and first tested their suitability for systemic virus injections. In line with the previously reported reduction of brightness of GCaMP6m by the Ribo-tag, Ribo-GCaMP8s only displayed dim signal confined to a small space in the soma 2 and 4 weeks after injection. After 6 weeks the signal had improved somewhat, to a level where single cells could be observed, but was still dim relative to the other functional constructs (Fig. 3). The expression was strictly confined to the soma, with little to no visible neuropil signal (Figs. 3a, right panel, S3b), however, we also observed indications of aggregated GCaMP in RO injected animals, possibly from projecting axon terminals or small ribosome clusters in dendrites. When delivered by an IC injection, Ribo-jGCaMP8 was relatively dim 2 and 4 weeks after injection and only showed small aggregated fluorescent spots with static signals (Fig. 3c, left image), similar to what we observed after RO injections. However, 6 weeks after IC injection both Ribo-jGCaMP8m and Ribo-jGCaMP8s showed bright and dynamic signals (Figs. 3b, S3b, Supplementary Video S5 and S6). The expression remained remarkably stable over time, up to the last sampling point 10 weeks post injection.

Notably, the wide-field signals from mice injected with Ribo-jGCaMPs were very weak throughout the experiment, likely as a result

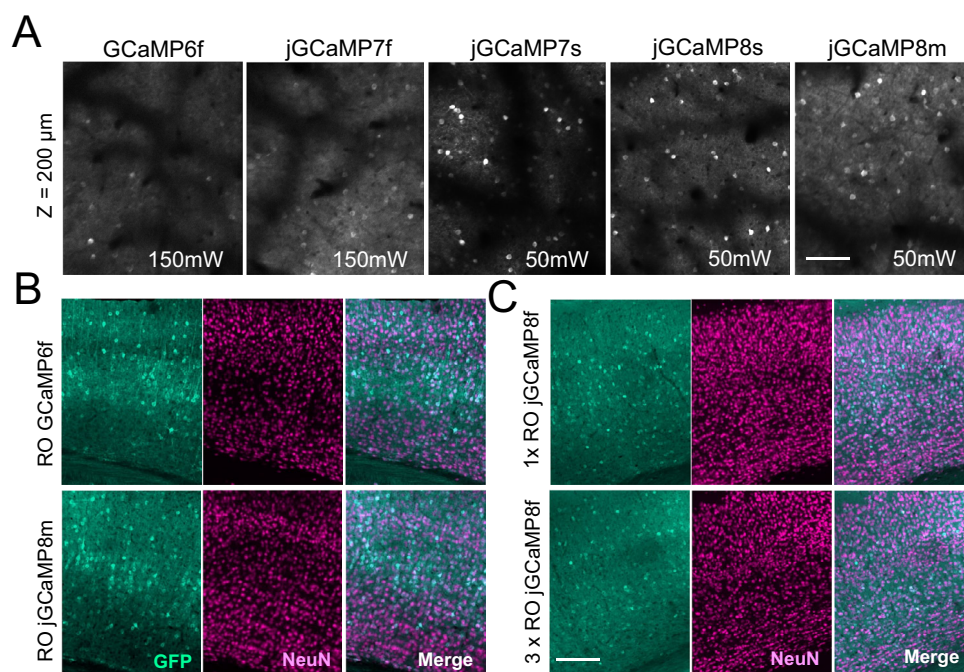


Fig. 2 | In vivo GECI screening after retro-orbital (RO) virus injections.

A Representative example images acquired by two-photon microscopy from five different GECIs acquired six weeks after RO virus injections. Note that GCaMP6f and jGCaMP7f were not detectable at reasonable illumination intensity (40–50 mW at 920 nm). The images shown from GCaMP6f and jGCaMP7f were acquired using 150 mW laser power for testing purposes only. The recently developed jGCaMP7s, 8 s, and 8 m were sufficiently bright using 50 mW. Scale bar indicates 250 μm. All

images are average intensity projections from 2000 frames with identical adjustments to brightness and contrast. **B** Representative histology images of sections from the primary visual cortex six weeks after RO injection. **A**, **B** the results were reproduced in $n \geq 3$ mice. **C** Similar to **B**, showing a comparison of expression levels of jGCaMP8f between RO injections of 100 or 300 μL volume. Scale bar for **B**, **C** indicates 250 μm. The results were reproduced in 2 mice.

of the lacking neuropil signals (example image from Ribo-jGCaMP8s shown in Fig. S1a). This indicates that wide-field Ca^{2+} imaging using these sensors would require far more sensitive imaging equipment compared to non-targeted or EE-RR-targeted jGCaMP8, but the recorded signal would reflect activity in the cell soma and not e.g. projecting axons.

We also tested former iterations of GCaMP (6m, 6f, 7f) in combination with EE-RR or ribosome-tethering. As expected from the performance of non-soma-targeted versions, these were not bright enough to use with RO injections.

The slow expression and aggregation of Ribo-jGCaMP8 that we observed may be a limiting factor to some experiments, for example by preventing imaging experiments in young animals, requiring removal of bone growth in suboptimal cranial window implants, or having to perform the virus injections and window implant in separate surgeries. In an attempt to improve the rate of expression, we replaced the linker region of Ribo-GCaMP8 with three different linker sequences; one longer and more flexible sequence, and two variations of rigid, helical linkers. The rigid helical linkers failed to rescue Ribo-GCaMP8 expression. However, the more flexible and longer linker, which is identical in amino acid sequence to the one used in EE-RR-GCaMP, greatly increased the rate of protein expression. This construct, which we term RiboL1-jGCaMP8s, displayed strong expression 1–2 weeks after intracerebral virus injection (Fig. 3b, c, Supplementary Video S7). In contrast to the original Ribo-jGCaMP8 construct, we could detect a substantial number of single cells just two weeks after the injection, with no indication of the aggregated, static puncta that we observed at the same time-point using Ribo-jGCaMP (Fig. 3c). The expression remained stable across many weeks. When tested with systemic injections, RiboL1-jGCaMP8 (m and s versions) was relatively dim, similar to the original Ribo-jGCaMP8 construct (example shown Fig. 4). Because of the promising expression patterns of RiboL1 compared to

the former ribosome-tethered versions when used with IC injection, we proceeded with this construct for further testing and analysis.

To verify that the functional properties of the neurons expressing EE-RR- and RiboL1 versions of jGCaMP8 were not compromised, we presented the mice with visual stimuli and measured the responses of single neurons in V1. With both GECIs we found strong visual responses and stable orientation tuning (examples shown in Fig. S5). Quantifications of spontaneous and stimulus-evoked Ca^{2+} events are shown in Fig. S5.

To directly compare the performance of the most promising GECIs using the two injection approaches, we first monitored expression stability over time, from 2 to 10 weeks after virus injection (Fig. 4). Our data indicated that RO injection gave rise to stable expression levels when compared to IC injection (Fig. 4), with no indication of microglia activation or intracellular aggregation (Fig. S6a). Notably, the RiboL1-jGCaMP8 construct gave rise to very stable expression levels when injected by an IC injection (Fig. 4, lower left panel) with no indication of intracellular aggregation. Indeed, in a separate experiment, we could record from the same population of neurons for more than 5 months (Fig. S6b).

Next, we compared the extracted Ca^{2+} traces from the cell soma and neuropil for the most promising GECIs using both injection techniques. The data used for the analysis were acquired 4–6 weeks after virus injections, and we narrowed our analysis to include jGCaMP8s, EE-RR-jGCaMP8s, and RiboL1-jGCaMP8s. We also included mice with IC injections of GCaMP6f for comparison, and for a within-subject visual comparison with RiboL1-jGCaMP8s, as these two GECIs were injected in opposite ends of the very same cranial windows in three mice (Fig. S4d).

We first calculated correlation coefficients between the soma and neuropil signal of the different GECIs. As described above, the high sensitivity and brightness of jGCaMP8 may lead to neuropil signals that

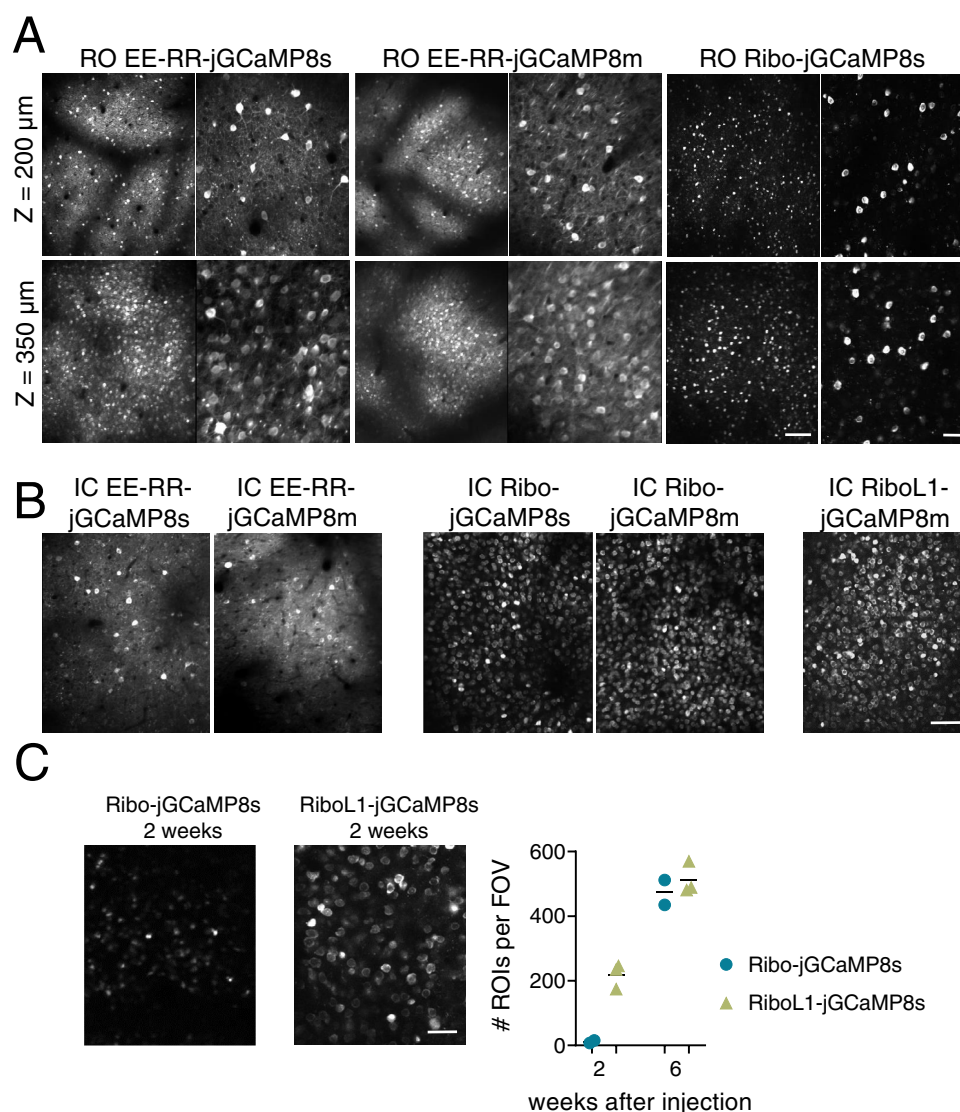


Fig. 3 | Soma-targeted jRCaMP8s expressed by RO and IC injections in primary visual cortex. **A** Representative example images from RO injected mice expressing EE-RR-jRCaMP8s and m, and Ribo-jRCaMP8s, at two different depths in cortex. Scale bars on lower right aligned images indicate 150 and 50 μm, respectively. All images shown are average intensity projections from 2000 frames with identical adjustments to brightness and contrast. Data from EE-RR constructs was acquired 4 weeks after virus injections, and 6 weeks for the ribosome-tethered construct. **B** Similar to **A**, showing expression after IC injections. Note the high number of identifiable single neurons with ribosome-tethering, compared to jRCaMP and EE-

RR-jRCaMP8s. Scale bar indicates 100 μm. **C** Development of expression of Ribo-jRCaMP8s and RiboL1-jRCaMP8s after IC injections. Two weeks after virus injections, Ribo-jRCaMP8s was only visible as static spots, while with RiboL1-jRCaMP8s individual neurons were identified. Six weeks after injection the two constructs were expressed similarly, as shown in **B**. Right panel shows the number of identified neurons per field of view 2 and 6 weeks after virus injections, identified from average intensity projections of 250 imaging frames. Field of view size was 420 × 350 μm, and $n = 2$ and 3 mice for Ribo-jRCaMP and RiboL1-jRCaMP, respectively. Scale bar indicates 30 μm. **A–C** The results were reproduced in $n \geq 3$ mice.

skew the $\Delta F/F$ calculation ratio which is often used for measuring neuronal activity. We found that the soma and neuropil signals were highly correlated for jRCaMP8s and EE-RR-jRCaMP8s, independent of injection technique (Fig. 5a). In contrast, RiboL1-jRCaMP8s correlations to neuropil were low. We next measured the baseline brightness (Fig. 5b). In line with our earlier observations, the expression of jRCaMP8 gave rise to the brightest baseline signals (median values across a recording), and fields-of-view (FOVs) with an IC injection were brighter than from RO injections. Moreover, RiboL1 baseline fluorescence was low, in particular when expressed from RO injections. However, when we compared the ratio between soma and neuropil signal brightness at baseline, RiboL1-jRCaMP8s showed the highest ratio using both RO and IC injections (Fig. 5c). Notably, RO injections of jRCaMP8s and EE-RR-jRCaMP8s gave rise to higher ratios compared to IC injections of the same constructs. Together, these results indicate

that IC-injected RiboL1-jRCaMP8s may provide better estimates of fluctuations of Ca^{2+} dynamics in the cell soma compared to the other constructs tested.

We next investigated the expression of GCaMP within the individual FOVs for each GECl, by comparing images made from average intensity projections. Surprisingly, the number of cells identified was not very different between RO and IC injected jRCaMP8s and EE-RR-jRCaMP8s, despite the difference in concentration of virus particles in the tissue that arises from the two techniques. However, this difference was substantial for RiboL1-jRCaMP8s between the two methods. The IC injections of RiboL1-jRCaMP8s gave by far the highest number of identified cells, which is in line with a previous report on ribosome-tethering and our earlier observations (Figs. 3b, 5d, e, S3).

Virus delivery by IC injections distributes the virus unevenly in the tissue, with a higher concentration of viral particles closer to the

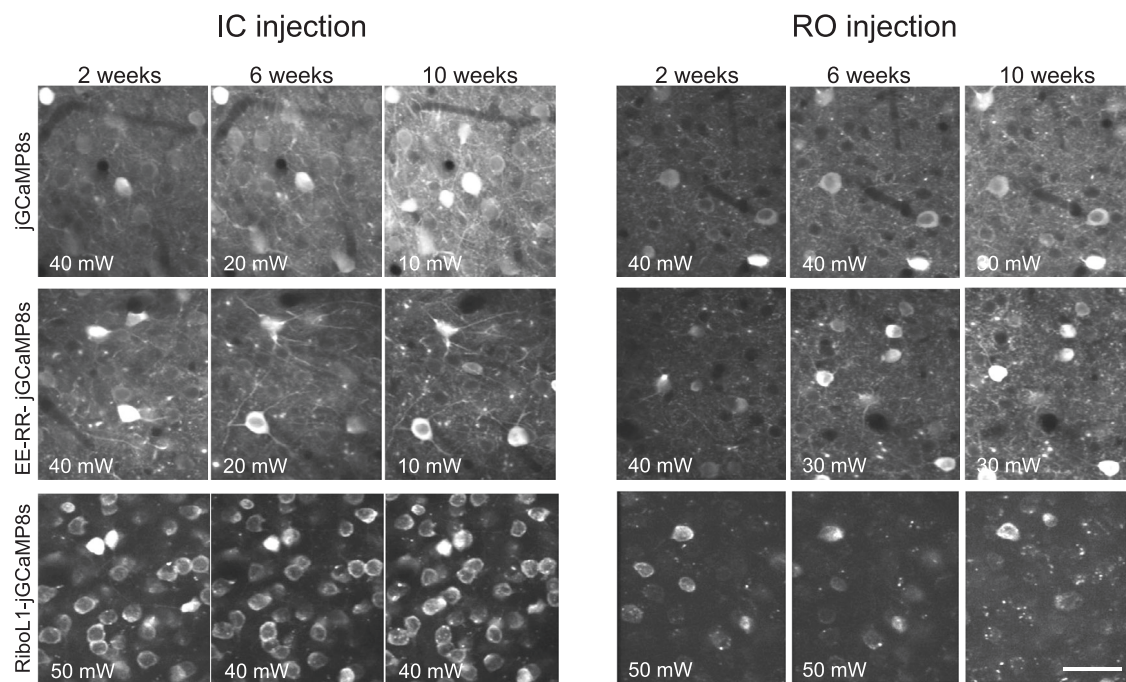


Fig. 4 | Expression over time of jGCaMP8s and soma-targeted jGCaMP8 using RO and IC virus injections. Note the dramatic reduction in illumination power (noted in the bottom left corner) used for jGCaMP8s and the EE-RR versions when expressed by an IC injection. RO injected jGCaMP8s and EE-RR-jGCaMP8s gave rise to very stable expression levels. For RiboLI-jGCaMP8s RO injections the signal was

relatively weak, but when using the same construct with IC injections a large population of neurons could be detected and the signal intensity remained stable throughout the experimental period. All images shown are average intensity projections from 250 frames with identical adjustments to brightness and contrast, and the results were reproduced in ≥ 3 mice. Scale bar indicates 30 μm .

injection site. This may lead to differences in signal intensity across the imaging area, and again affect the quality of the data collection, an effect that may be alleviated by systemic administration of the viral vector. To test this, we compared the signal intensity across the FOV (x direction) at three evenly distributed sampling sites per FOV (Fig. 5e). We found that RO injections of jGCaMP8s indeed showed even signal intensity across the FOV, albeit with some variation and higher intensity around the central area, possibly reflecting uneven illumination that leads to increased neuropil signals. In contrast, the signal intensity after IC injections of jGCaMP8s was more than 40% higher in the center of the FOV compared to the edges. The expression following IC injections of RiboLI-jGCaMP showed by far the most even signal intensity, likely reflecting the almost complete lack of neuropil signals (Fig. 5f).

Applications of systemic GECI injections

One of the challenges with using transgenic mice to express a GECI is that it limits the use of cell-type targeted transgenics, e.g. manipulations of the activity of a specific cell population, while expressing the GECI brain-wide. To test the suitability of RO injections for this purpose, we used PV-Cre mice¹⁹ that express Cre under the parvalbumin (PV) promoter and performed an RO injection of EE-RR-jGCaMP8s combined with intracerebral injections of an AAV5 vector expressing a FLEX-hM4D receptor (DREADD). Indeed, this produced co-expression of both constructs in putative PV neurons and with a uniform expression of jGCaMP8 in surrounding neurons (Fig. S7a). This was also verified by post-mortem histology (Fig. S7a).

Next, we tested the red-shifted GECI jREX-GECO1 (Fig. S7b), a long Stokes-shift version of the red GECI RGECO that is optimized for two-color imaging with a single laser source. This enables imaging with the same 920 nm laser as for green GECIs meaning that jREX-GECO1 could be used for imaging axonal activity in combination with a soma-targeted green-shifted Ca^{2+} indicator (e.g.,^{20,21}). To this end, we constructed axon-targeted jREX-GECO1 (hSyn-Axon-jREX-GECO1) and

performed virus injections into the dorsal lateral geniculate nucleus, combined with IC injections of RiboLI-jGCaMP8s in VI. We then imaged the activity in axonal boutons and cell somas in VI two weeks after viral injections, and found strong signals from both GECIs (Fig. 6a, f shows examples from in vivo imaging and histology, respectively). We detected axonal boutons with both highly correlated and non-correlated changes in fluorescence with the soma signal (Fig. 6b–e). Axon-jGCaMP8s m and f were also prepared, but were not tested in this paper.

Discussion

Engineered AAV serotypes with high affinity for the central nervous system that can be delivered intravenously represent a minimally invasive and low-cost method for introducing genetic payloads into the brain. Yet, these new serotypes, notably PHP.eB, have not been much used to deliver GECIs, despite obvious advantages in terms of animal welfare, cost, productivity, and experimental flexibility. Previous work shows that wide-field imaging with systemically administered GCaMP6f is feasible using other promoters than synapsin^{15,22}. In our own preliminary experiments, we experienced that widely used GECIs (such as GCaMP6f) was not bright enough to be compatible with systemic administration for use with two-photon imaging. A reduction in brightness in a systemic administration is not unexpected, as the multiplicity of infection will be lower relative to an intracerebral injection, i.e., each cell is infected by fewer viral particles. Here, we screened 16 GECIs and one fluorescent probe and show that newer iterations of jGCaMPs, particularly jGCaMP7s, jGCaMP8s, and jGCaMP8m, are indeed sufficiently bright for two-photon in vivo Ca^{2+} imaging when administered systemically in PHP.eB AAVs. However, we also observed strong neuropil signals from these sensors which may influence the detection accuracy of individual neuron activity, regardless of the administration route. By fusing the latest jGCaMP variants with soma-targeting peptides we overcame this issue. We show that

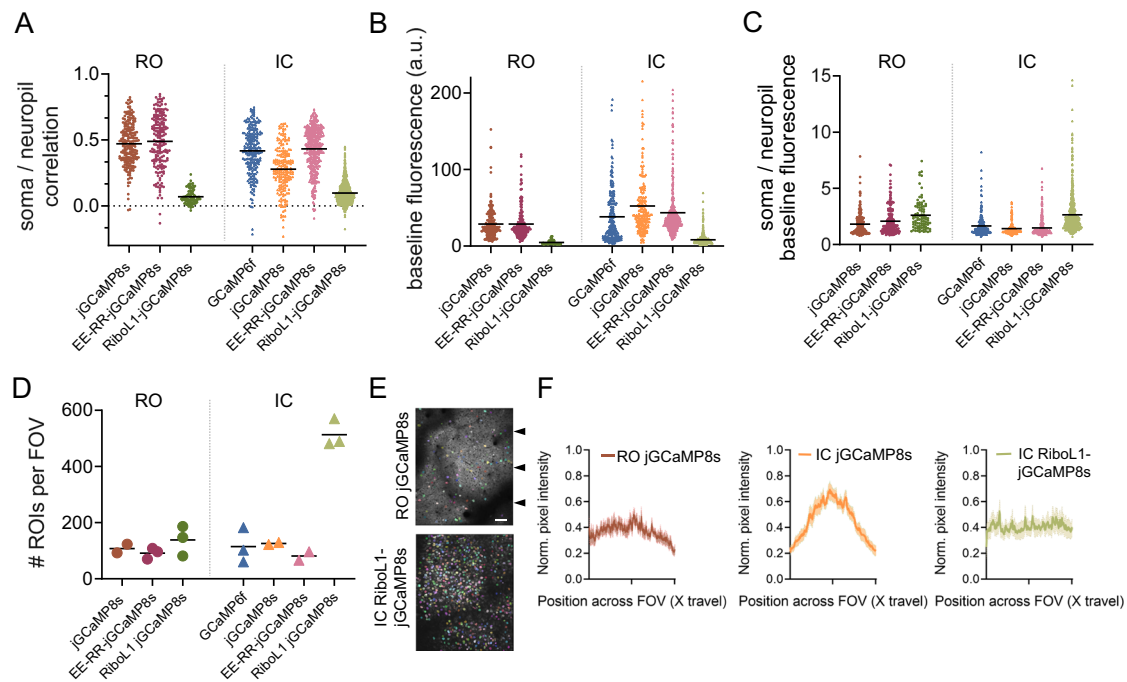


Fig. 5 | Baseline brightness, signal-to-noise, and cell density quantification. **A** Pearson correlation coefficients of somatic to neuropil signals of RO or IC administered jCaMP8s. **B** Baseline (median) fluorescence intensity. **C** Soma over neuropil baseline (median) fluorescence intensity. **A–C** $n = 4$ mice per GECl for RO injections, 3 mice per GECl for IC injections; all data points indicate individual cells, lines indicate population means. **D** Number of ROIs detected per field of view in Cellpose. Each data point indicates one FOV from one mouse, line indicates

population mean. Scale bar indicates 50 μm . **E** Examples of Cellpose segmentation mask (ROIs) for RO jCaMP8s and IC RiboL1-jCaMP8s. Arrows indicate the y positions of measurements used for **F**. **F** Normalized intensity profiles across the field of view. Intensity was measured at three y positions and normalized to the highest pixel value. $n = 5, 4,$ and 4 mice. Lines indicate population mean, shaded area represents the SEM. Source data are available as a Source Data file.

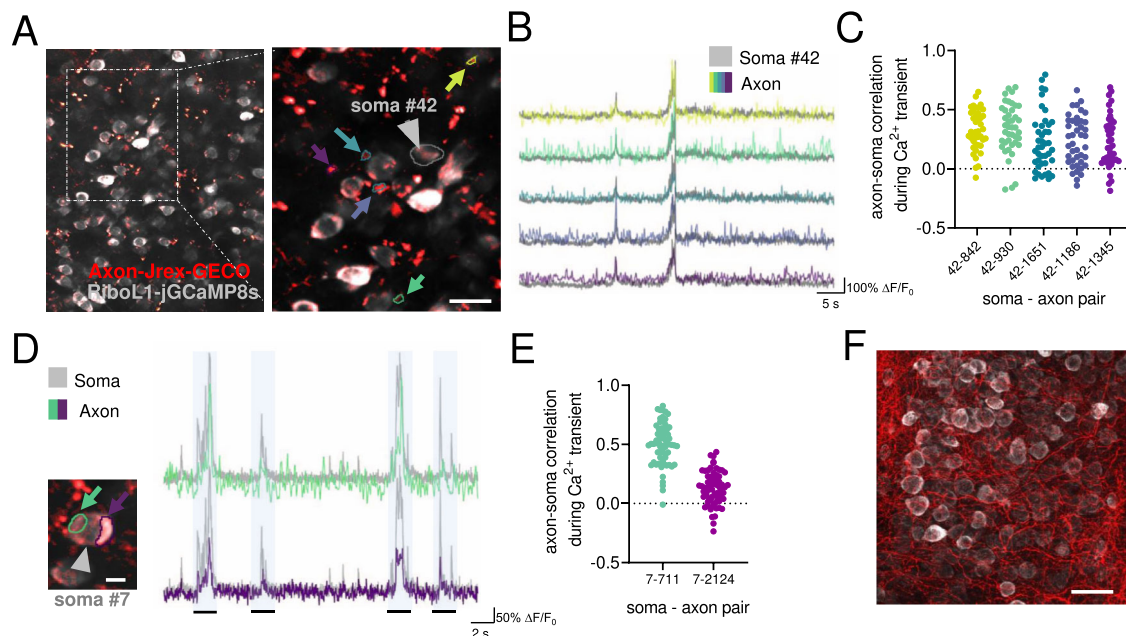


Fig. 6 | Simultaneous in vivo imaging of axonal and somatic activity. **A** An example field-of-view in primary visual cortex with Axon-jREX-GECO1 in red and RiboL1-jCaMP8s in gray. Colored arrows indicate labeled regions of interest from the red channel. The cell soma ROI from the green channel is indicated by a gray arrow. Scale bar indicates 15 μm . **B** Red channel Ca^{2+} traces (colored) from each bouton overlaid on the soma signal (gray). Despite clear spatial separation, the indicated regions of interest show similar activity patterns (middle and right panel). **C** Cross-correlation of soma and axon signal during periods of Ca^{2+} transients in the

soma. Each dot represents the correlation between soma # 42 (as shown in **B**) and a specific axon bouton (colors indicate different boutons shown in **B**), for each somatic Ca^{2+} transient during a recording. **D**, **E** Two regions of interest in close proximity to a cell soma, indicated by colored arrows, and corresponding Ca^{2+} traces overlaid on the soma signal at different time points. The shaded regions represent time bins where cross-correlations were calculated. Scale bar indicates 5 μm . **E**, **F** Histological verification of expression. Source data used for **C** and **E** are available as a Source Data file. Scale bar indicates 25 μm .

RiboL1-jGCaMP8 outperforms existing GECI constructs using intracerebral virus injections.

An intravenous AAV injection in the retro-orbital sinus can be performed within minutes and requires very little training. The procedure is substantially less invasive than stereotaxic/intracerebral injections. The intravenous injection provides largely uniform expression across the mouse brain, which is stable over extended time periods. This stands in contrast to intracerebral virus injections that may result in excessive expression leading to unhealthy cells and even cell death. Moreover, we observed that the variability in expression that may arise from differences in viral titers is less prominent with RO-administrated AAVs compared to IC administration. This is in line with our observations from the triple RO injected animals, where more virus delivered across days did not increase GECI expression. We note that in our hands, stable expression was resulting both from the administration route and the PHP.eB serotype.

Despite the many advantages of intravenously injected virus for GECI delivery, it has one considerable drawback; intravenous administration requires a large dose of virus per animal. If all viruses are purchased from commercial vendors, this could be prohibitively expensive. On the other hand, if viruses are produced in-house or by a local virus core, scaling up production to suitable levels is relatively inexpensive, and was not an issue for our experiments. Performing injections in younger animals will substantially reduce the amount of virus required. Additionally, a stronger promoter such as CAG could be used to reduce the required amount of virus²³. Unlike the Synapsin promoter, which is commonly used in neuroscience, CAG would not limit expression to neurons, and despite the strong tropism of PHP.eB AAV to neurons, would result in some glial cells expressing jGCaMP. This could be prevented if a FLEX/DIO construct is used, but this would introduce the need for transgenic lines or an additional Cre-expressing virus. An additional caveat concerning PHP.eB and AAV9 serotype AAVs is the clear bias in expression for cortical layer 5, striatum, CA2, and subiculum regions. While the bias towards cortical layer 5 might be explained by the large cell volumes and thus higher capacity for transgene production, this does not appear to be a common feature for the preferred brain areas. An alternative explanation might be that differences in vascularization are determinants of expression levels. However, this is at least unlikely for CA2 of the hippocampus which exhibits strikingly strong expression compared to neighboring hippocampal areas with no large differences in vascularization^{24,25}. Notably, the bias for layer 5 neurons was not as clear for ribosome-tethered versions of jGCaMP8. Because transfection efficiency is mainly decided by serotype, this could indicate that it could be a result of signal masking by neuropil. If the mechanisms behind expression differences are identified and reduced in future iterations of synthetic AAV serotypes, fewer viruses may be required to achieve sufficient expression in the upper layers of the cortex for in vivo imaging. Future versions of synthetic AAV serotypes could also, potentially, deliver the virus more efficiently through the BBB to the brain, reducing the required volume of virus.

The need for high brightness of the GECI for systemic administration also caused neuropil contamination of the signals. We therefore made use of two soma-targeting strategies that restricted expression to the cell somata. We show that EE-RR soma-targeting led to the highly stable expression, which was already visible after two weeks, while ribosome-tethering reduced the brightness to such an extent that we did not observe cells during in vivo imaging until 4–6 weeks after injection. Nonetheless, imaging could be performed using reasonable laser power 6 weeks after injection, and the ribosome-tethering led to highly selective although somewhat limited expression in the cell soma. For intracerebral injections, ribosome tethering showed a very high density of cell labeling, but again the expression was slow. We therefore introduced a version with a modified linker region (RiboL1-jGCaMP8) that greatly improved this

feature. Using RiboL1-jGCaMP8 we could initiate imaging just one week after intracerebral virus injection, with no apparent drawbacks such as overexpression over extended time periods. In general, ribosome-targeted GECI expression leads to improved signal-to-noise and the possibility to detect activity from a higher number of cells as their activity is not masked by neuropil activity. We also observed that automatic cell detection in Suite2p was more accurate and required smaller data sets from recordings with the ribosome-tethered GECIs.

While reducing neuropil signal is generally favorable when recording from somata, it may in some cases be required for the acquisition of reliable data; a recent paper demonstrates that the signal recorded in striatal fiber photometry or one-photon experiments is mostly produced by neural processes, not striatal cell bodies²⁶. Eliminating neuropil signal with a strictly soma-targeted GECI could potentially circumvent this issue, allowing for reliable recordings of somatic Ca²⁺ transients in striatum, or similar brain regions with dense neuropil.

A major challenge when using transgenic animal models to express GECIs is the need for driver lines with general promoters preventing the use of other transgenics. Moreover, co-expression of several viruses in the same brain region, at least in our hands, often proves difficult. In contrast, we show that RO-injected PHP.eB virus is compatible with transgenic lines and co-expression of another virus to obtain cell-specific expression of e.g., a chemogenetic receptor to manipulate their activity or labeling a specific cell population.

In summary, we present a suite of viral vectors for use with both systemic and intracerebral administration that show remarkably high performance and sustainable expression over longer periods. Due to the simplicity of the methods, high experimental flexibility, low-cost and high performance, we believe that these GECI constructs are promising candidates to replace, or complement, transgenic animal models for GECI expression. Our results show that jGCaMP8 and EE-RR-jGCaMP8 are highly suitable for systemic delivery and give rise to brain-wide expression within two weeks and remain stable over months. Finally, the ribosome-tethered jGCaMP8 shows unprecedented labeling density and signal-to-noise that is highly suitable for intracerebral virus injections.

Methods

GECI plasmids

All plasmids were transformed into NEB Stable (NEB) competent cells for amplification, and purified using the Zymopure II maxiprep kit (Zymo Research). To obtain Soma-targeted (EE-RR) jGCaMP8, pAAV-Syn-Soma-jGCaMP7 was digested with HpaI and EcoRI to isolate the linker and Soma-tag. The fragment was then ligated into AAV-hSyn-jGCaMP8s, m and f, which was previously digested using the same restriction enzymes. pAAV-Syn-Soma-jGCaMP7¹⁸ was a gift from Edward Boyden (http://n2t.net/addgene:158759;RRID:Addgene_158759). AAV-syn-jGCaMP8s-WPRE³ was a gift from GENIE Project (http://n2t.net/addgene:162374;RRID:Addgene_162374), as well as jGCaMP8f (Addgene:162376), jGCaMP8m (Addgene:162376) and jGCaMP7c (Addgene: 105320). To obtain ribo-tagged jGCaMP8, pyc126m (Ribo-GCaMP6m) was digested with HpaI and EcoRI to isolate the linker and Ribo-tag. The fragment was then ligated into AAV-syn-jGCaMP8s, m and f, previously linearized using the same restriction enzymes. pycm126¹⁷ was a gift from Jennifer Garrison & Zachary Knight (http://n2t.net/addgene:158777;RRID:Addgene_158777). To obtain Synapsin promoter expressed jREX-GECO1, the jREX-GECO1 coding sequence was cut from CMV-jREX-GECO1 using BamHI and EcoRI, and inserted into a pAAV-Syn-Chr2 plasmid, which was digested with the same restriction enzymes, removing the coding sequence of Chr2 and replacing it with jREX-GECO1. jREX-GECO1 expressed under a CMV promoter was a gift from Neurophotonic^{27,28}. The hSyn plasmid, pAAV-Syn_ChR2(H134R)-GFP²⁹ was a gift from Edward Boyden (http://n2t.net/addgene:58880;RRID:Addgene_58880). To obtain

Ribo-jGCaMP8 with modified linkers, three different linkers were synthesized (Table S1, GeneArt Invitrogen, codon optimized) and inserted into jGCaMP8s, m and f plasmids using HpaI and AclI (NEB). The first linker, RiboL1, was adapted from the SomajGCaMP7f plasmid. The second and third linkers were variations of rigid helical linkers³⁰, RiboL2: LEA(EAAAK)4ALE, and RiboL3: LEA(EAAAK)4ALEA(EAAAK)4ALE. To obtain axon-targeted jREX-GECO1 and jGCaMP8, a fragment (Table S1) encoding the 20AA axon targeting motif from Broussard et al.²⁰ was synthesized (Invitrogen, GeneArt) and ligated into jREX-GECO1 and jGCaMP8s and m plasmids. FLEX-RiboL1-jGCaMP8s/f/m plasmids were generated by PCR cloning; briefly, a 5' NheI restriction site was introduced via PCR amplification, and the resulting amplicon containing RiboL1-jGCaMP8 was linearized using NheI/AscI, and ligated to a FLEX backbone (#44362) linearized with the same enzymes. Additional plasmids, GCaMP6f, somaGCaMP6f, jGCaMP7f, jGCaMP7s and mNeonGreen were acquired from addgene and were not modified in this paper. pAAV.Syn.GCaMP6f.WPRE.SV40³¹ was a gift from Douglas Kim & GENIE Project (<http://n2t.net/addgene:100837>; RRID:Addgene_100837). pGP-AAV-Syn-jGCaMP7f-WPRE was a gift from Douglas Kim & GENIE Project (<http://n2t.net/addgene:104488>; RRID:Addgene_104488). pGP-AAV-Syn-jGCaMP7s-WPRE² was a gift from Douglas Kim & GENIE Project (<http://n2t.net/addgene:104487>; RRID:Addgene_104487). pAAV-CAG-mNeonGreen¹⁴ was a gift from Viviana Gradinaru (<http://n2t.net/addgene:99134>; RRID:Addgene_99134). Plasmids for AAV packaging were acquired from Addgene and Penn Vector core, which is now available from Addgene. Only PHP.eB serotype viruses were used in this paper, except for the cre-dependent DREADD-mCherry, pAAV-hSyn-DIO-hM4D(Gi)-mCherry³² which was a gift from Bryan Roth (Addgene viral prep # 44362-AAV5;<http://n2t.net/addgene:44362>; RRID:Addgene_44362). The PHP.eB serotype plasmid, pUCmini-iCAP-PHP.eB¹⁴ was a gift from Viviana Gradinaru (<http://n2t.net/addgene:103005>; RRID:Addgene_103005). The DeltaF6 helper plasmid, pAdDeltaF6, was a gift from James M. Wilson (<http://n2t.net/addgene:112867>; RRID:Addgene_112867).

AAV production. Viral vectors were produced according to the protocol developed by Challis et al.³³. Briefly, AAV HEK293T cells (Agilent) were cultured in DMEM with 4.5 g/L glucose & L-Glutamine (Lonza), 10% FBS (Sigma) and 1% PenStrep (Sigma), in a 37 °C humidified incubator. The cells were thawed fresh and split at ~80% confluency until four 182.5 cm² flasks were obtained for each viral prep. The cells were transfected at 80% confluency and the media was exchanged for fresh media directly before transfection. The cells were triple transfected with ΔF6 helper plasmid and PHP.eB serotype plasmid. Polyethylenimine (PEI), linear, molecular weight (MW) 25,000 (Polysciences, cat. no. 23966-1) was used as the transfection reagent. Media was harvested three days after transfection and kept at 4 °C, and media with cells was harvested five days after transfection and combined with the first media harvest. After 30 min centrifugation at 4000 × g, the cell pellet was incubated with SAN enzyme (Arctic enzymes) for 1 h. The supernatant was mixed 1:5 with PEG and incubated for 2 h on ice, then centrifuged at 4000 × g for 30 min to obtain a PEG pellet containing the virus. The PEG pellet was dissolved in SAN buffer and combined with the SAN cell pellet for incubation at 37 °C for 30 min. To purify the AAV particles, the suspension was centrifuged at 3000 × g for 15 min. The supernatant was loaded on the top layer of an Optiseal tube with gradients consisting of 15%, 25%, 40 and 60% iodixanol (Optiprep). Ultracentrifugation was performed for 2.5 h at 18 °C at 350,000 × g in a type 70 Ti rotor. The interface between the 60 and 40% gradient was extracted along with the 40% layer, avoiding the protein layer on top of the 40% layer. The viral solution was filtered through a Millex- 33 mm PES filter and transferred to an Amicon Ultra-15 centrifugal filter device (100-kDa molecular weight cutoff, Millipore) for buffer exchange. A total of four washes with 13 ml

DPBS were performed at 3000 × g before concentration to a volume of ~500–750 μL. Viral solutions were sterilized using a 13 mm PES syringe filter 0.2 μm (Nalgene), and stored in sterile, low-bind screw-cap vials at 4 °C.

Viral titers were determined using qPCR with primers targeting AAV2 ITR sites³⁴ (Table S1), following the “AAV Titration by qPCR Using SYBR Green Technology” protocol by Addgene¹². Briefly, 5 μL of viral sample was added to 39 μL ultrapure H₂O, 5 μL 10× DNase buffer, 1 μL DNase, and incubated at 37 °C for 30 min to eliminate all DNA not packaged into AAV capsids. 5 μL of the DNase-treated sample was added to a reaction mix consisting of 10 μL 2× SYBR master mix, 0.15 μL of each primer (100 μM) and 4.7 μL nuclease free H₂O. Cycling conditions for the qPCR program were: 98 °C 3 min/98 °C 15 s/58 °C 30 s/read plate/ repeat 39× from step 3/melt curve.

In addition to the constructs tested in the manuscript, we also made modified versions of them (e.g. FLEX- versions and jGCaMP8f). All plasmids are deposited to Addgene.

Experimental animals. All work with experimental animals was performed at the animal facility at the Department of Biosciences, Oslo, Norway, in agreement with guidelines for work with laboratory animals described by the European union (directive 2010/63/EU) and the Norwegian Animal Welfare Act from 2010. The experiments were approved by the National Animal Research Authority of Norway (Mattilsynet, FOTS #14680 and 29491).

Four weeks old male C57/BL6j mice were purchased from Janvier Labs, and housed in GM500 IVC cages in groups of four. After an acclimation period of two weeks, the animals were split into two mice per cage prior to virus injections. One week after injections, the mice were housed individually, and remained single-housed for the duration of the experimental period. The housing room had a 12/12 h light cycle, with lights off at noon. In the light phase, light intensity in the room was 215 lux, and in the cages varied from 20–60 lux, depending on position in the rack. The ambient temperature in the housing room was kept at 21 ± 1 °C, with 25–30% humidity. All experiments were performed in the dark phase. For enrichment purposes, each cage had a running wheel and large amounts of nesting material, and the mice had *ad libitum* access to food and water.

Prior to starting the imaging experiments, the mice were habituated to head-fixation and the running wheel. Each animal was head-fixed for 5–10 min on three to five consecutive days and given Ensure milkshake by a syringe as positive reinforcement. If the mouse at any point showed clear signs of discomfort, they were placed back in their home cage and reintroduced to the apparatus later in the same day.

Retro-orbital injections. Pairs of mice were randomly assigned to a viral vector. The mice were placed in an induction chamber and briefly anesthetized by isoflurane, before they were transferred to a mask with 1–2% isoflurane delivered. An eye drop of local anesthetic (oxybuprocaine 4 mg/mL, Bausch Health), was applied to the right eye, and one minute later 100–150 μL of virus (virus titers are listed in Tables 1 and 2) injected into the retro-orbital sinus using a U100 insulin syringe (BD micro-fine 0.3 mL, 30 gauge needle). The volume was determined based on the animal's weight¹⁶. The surface of the eye was flushed with saline and cleaned with a cotton tip. The mice were then placed back in the home cage and monitored for 10–15 min, before they were returned to the housing room. All animals fully recovered within minutes. In one single mouse, we observed eye damage to the injected side after one week. It is not clear whether this resulted from the injection or resulting from the high incidence of eye abnormalities in the c57bl6 mouse strain³⁵. Each viral vector was tested in at least two mice with RO injections and one mouse with intracerebral injection. The GEICs that were deemed bright enough for use with RO injections were further tested in at least three additional mice with both injection techniques.

Table 2 | Soma and axon-targeted GECI constructs prepared in this work

GECI	Titer (VG/ml)	Detectable at 50 mW (RO injection)	Addgene plasmid #
EE-RR-jGCaMP8m (soma)	1.93E + 13	Yes	169257
EE-RR-jGCaMP8s (soma)	1.73E + 13	Yes	169256
EE-RR-jGCaMP8f (soma)	NA	Not tested	169258
Ribo-jGCaMP8m	3.27E + 13	No	167574
Ribo-jGCaMP8s	2.80E + 13	Yes	167572
Ribo-jGCaMP8f	NA	Not tested	167573
RiboL1-jGCaMP8s	1.17E + 13	Yes	169247
RiboL1-jGCaMP8m	3.18E12	No	169248
RiboL1-jGCaMP8f	NA	Not tested	169249
RiboL1-jGCaMP7c	NA	Not tested	192619
FLEX-RiboL1-jGCaMP8s	NA	Not tested	192616
FLEX-RiboL1-jGCaMP8m	NA	Not tested	192617
FLEX-RiboL1-jGCaMP8f	NA	Not tested	192618
Axon-jGCaMP8m	NA	Not tested	172719
Axon-jGCaMP8s	NA	Not tested	172720
Axon-jGCaMP8f	NA	Not tested	192615
Axon-jREX-GECO1	6,66E + 12	Not tested	172714

Surgical procedures. The mice were anesthetized by an intraperitoneal injection of a ketamine/xylazine cocktail (Ketamine 12.5 mg/kg, Pfizer; xylazine 5 mg/kg, Bayer Animal Health GmbH). The top of the head was shaved, and the animals placed on a heating pad in a stereotaxic frame with a mouse adapter (Model 926, David Kopf Instruments). The eyes were covered with white vaseline to prevent drying and to protect them from light. Dexamethasone (5 mg/kg, MSD Animal Health) was delivered via intramuscular injection to prevent edema, and local anesthetic bupivacaine (Aspen) injected in the skin of the scalp. In a subset of animals, the mice were anesthetized by isoflurane (3.5% induction, 1–1.5% maintenance) and additionally injected subcutaneously with buprenorphine (0.05 mg/kg, Indivior Ltd) for analgesia. The skin was cleaned with 70% ethanol and chlorhexidine, and a small piece of skin covering the top of the skull was cut away. The periosteum and other membranes were removed using fine forceps and cotton swabs, and the surface of the skull slightly scored with a scalpel. A custom titanium head post was attached using a few drops of cyanoacrylate and secured using VetBond (3 M) and C&B Metabond (Parkell). A 3.0 mm craniotomy was made using a Perfecta 300 hand-held drill (W&H) with a 0.5 mm drill bit (Hager & Meisinger GmbH), centered over primary visual cortex (center coordinates were 2.5 mm ML and 1 mm AP relative to lambda). Custom cranial windows were made by attaching a 3.0 mm diameter round glass (Tower Optical) with 0.45 mm thickness to a 5.0 mm diameter glass (Warner Instruments, USA) with 100 μ m thickness using Norland Optical adhesive (Thorlabs GmbH, Germany) under UV light. The cranial window was implanted and secured with C&B Metabond, and a 3D-printed light shield was attached to the head post with black dental acrylic⁸. At the end of the procedures, the mice were injected subcutaneously with 0.3 mL 0.9% saline, meloxicam (5 mg/kg, Boehringer Ingelheim Vet-Medica GmbH), and Antisedan (0.0012 mg/kg, Orion Pharma) (the latter only applies to the mice injected with ketamine/xylazine for anesthesia). Injections of meloxicam were repeated for three days.

In a subset of mice, bone growth partially obscured the view through the cranial window over the course of the experimental

period. In these cases, the animal was anesthetized by isoflurane, the window removed to clear away any bone growth and other debris, and a new cranial window implanted⁸. The procedure was performed one week prior to imaging to allow the tissue to recover from potential damage during bone removal.

Intracerebral virus injections. Glass capillaries (OD 1.14 mm; ID 0.53 mm) were pulled and beveled at a 40-degree angle³⁶, and mounted in a NanoJect 3 (Drummond Scientific, USA). The pipette was front-loaded with the virus solution and 150 nL injected at a depth of 350–500 μ m below the dura, in 5 nL steps. After the last injection, the pipette was left in the tissue for five minutes before retraction and loading of a new pipette. Two to three different constructs were injected per animal, spaced at least 700 μ m apart. After the final injection, the exposed brain surface was cleaned with saline, and a cranial window implanted as described above.

Co-expression of Axon-jREX-GECO1 and soma-targeted GECIs. For co-expression of Axon-jREX-GECO1 and RiboL1-jGCaMP8, surgical procedures were conducted as described above. After attachment of the head post, a small craniotomy was made above the dLGN, and 150 nL of virus slowly injected in 5 nL steps over 5 min (injection coordinates relative to bregma were 2.1 mm posterior, 2.3 mm lateral, and 2.5 mm below the dura). A larger craniotomy was then made over V1, RiboL1-jGCaMP8s was injected and a cranial window implanted as described above.

Wide-field imaging. Wide-field imaging was used to monitor the expression levels of the Ca²⁺ sensors and quality of the cranial windows. The mice were head-fixed on a custom 3D-printed running wheel using optical posts that were mounted to the optical table, holding clamps (Standa) and modified ball-joints (Thorlabs GmbH) allowing for adjustments in AP elevation. Single images were acquired by a Canon EOS 4000D camera through a $\times 5$ Mitutoyo long working distance objective (0.14 NA) in an Olympus BX-2 microscope. The light source was a xenon arc Lambda XL lamp (Sutter Instruments) with 480/545 nm and 560/635 nm filters (#39002 and #39010, Chroma). All animals were imaged using two sets of parameters at each time-point, with exposure times of 600 and 2000 ms, and ISO of 100 and 400, respectively. The mice ran freely in darkness during imaging. In addition, wide-field videos were captured at 25 Hz during both spontaneous activity (in darkness) and with visual stimulation.

Two-photon imaging. For in vivo two-photon imaging we used a resonant-galvo Movable Objective Microscope (MOM, Sutter Instruments) with a MaiTai DeepSee laser (SpectraPhysics) set to a wavelength of 920 nm. The main objective used for screening was a $\times 10$ objective (TL-10 $\times 2P$, 0.5 NA, 7.77 mm working distance, Thorlabs), giving a field of view of approximately 1665 \times 1390 μ m. In mice with successful GCaMP imaging, we also imaged at lower depths (200–500 μ m) using a Nikon $\times 16$ objective (NA 0.8), giving a field of view of approximately 1050 \times 890 μ m, or an Olympus $\times 20$ objective (NA 1.0) giving a field of view of 840 \times 700 μ m. The laser was controlled by a pockel's cell (302 RM, Conoptics), and fluorescence was detected through Chroma bandpass filters (HQ535-50-2p and HQ610-75-2p, Chroma) by PMTs (H10770PA-40, Hamamatsu). Images were acquired at 30.9 Hz using MCS software (Sutter Instruments). Output power at the front aperture of the objective was measured prior to each imaging session with a FieldMate power meter (Coherent) and set to 45 mW, unless mentioned otherwise. The microscope was tilted to an angle of 6–12 degrees during imaging to match the surface of the brain, in addition to the 4–6 degree forward tilt made by the head-fixing apparatus.

Table 3 | List of antibodies used for post-mortem histology

Antibody	Supplier	Dilution used	RRID	Cat #
Chicken anti-GFP	Invitrogen	1:1000	AB_2534023	A10262
Rabbit anti-NeuN	Abcam	1:100	AB_2532109	Ab177487
Goat anti-TdTomato	Sicgen	1:2000	AB_2722750	AB8181
Rabbit anti-parvalbumin	Swant	1:2000	AB_2631173	PV27
Goat anti-Iba1	Invitrogen	1:500	AB_10982846	PA5-18039
Donkey anti-goat IgG, CF 568 conj.	Biotium	1:1000	AB_10854239	20106-1
Goat anti-chicken IgG, AF 488 conj.	Invitrogen	1:1000	AB_142924	A-11039
Goat anti-rabbit IgG, AF 647 conj.	Invitrogen	1:1000	AB_2535813	A-21245
Chicken anti-rabbit IgG, AF 488 conj.	Invitrogen	1:1000	AB_2535859	A-21441
Donkey anti-chicken IgY, CF 488 conj.	Sigma Aldrich	1:1000	AB_2721061	SAB4600031
Donkey anti-goat IgG, AF 647 conj.	Invitrogen	1:1000	AB_2535864	A-21447

Co-expression of GCaMP and cell-specific DREADDs. PV-Cre mice (Jackson Laboratories, strain #017320) were injected in the retro-orbital sinus with Soma-jGCaMP8s as described above. Two weeks later, 150nL of pAAV5-hSyn-DIO-hM4D(Gi)-mCherry (#44362, Addgene) was injected into the cortex, and a cranial window implanted.

Visual stimulus. Sinusoidal drifting gratings were generated using the open-source Python software PsychoPy³⁷, and synchronized with two-photon imaging through a parallel port and PCIe-6321 data acquisition board (National Instruments). We used drifting gratings of three orientations (0, 135, and 270 degrees) with a spatial frequency of four cycles per degree and temporal frequency of 2 Hz. Stimulus was shown for 3 seconds, interleaved with an 8 second gray screen period.

Two-photon imaging analysis. Motion-correction and automatic detection of regions of interest (ROIs) was performed using suite2p³⁸. The data were then manually curated and analyzed using custom Python scripts. To calculate the relative fluorescence $\Delta F/F_0$, traces were first corrected for neuropil using $F_c = (F - 0.7 * F_{neu} + 0.7 * F_{neu_median})$, where F is the raw fluorescence, F_{neu} is the neuropil signal defined by suite2p as the fluorescence in a circle around the ROI, and F_{neu_median} is the median of that signal. $\Delta F/F_0$ was then defined as $(F_c - F_0)/F_0$, where F_0 is the median of the neuropil-corrected trace F_c . The soma/neuropil correlation was defined as the Pearson Correlation Coefficient between the raw fluorescence trace F and the neuropil trace F_{neu} for each ROI. The soma/neuropil baseline ratio was determined as the ratio between the median of the raw fluorescence trace F and the median of the neuropil trace F_{neu} for each ROI over the entire recording time. The baseline fluorescence of an ROI was defined as the median of the raw fluorescence F . Stimulus-evoked event rates were calculated based on the activity during the 3-second stimulus presentation, and spontaneous event rates were calculated from the activity during the 8-second inter-trial interval for the same ROIs.

Soma-axon pair correlation. To determine the correlations between soma-axon pairs, we defined a threshold at $2 * \text{std}$ of the $\Delta F/F_0$ trace of the soma to identify spikes. When at least two subsequent frames exceeded the threshold, a window from 324 ms before to 1942 ms after the spike was defined. For each of these windows, the Pearson Correlation Coefficient was determined between the soma $\Delta F/F_0$ trace and the corresponding axon $\Delta F/F_0$ trace. For proof-of-principle purposes, we used RiboL1-jGCaMP8s signal from one representative soma and Axon-jRex-GECO signals from 7 representative boutons (5 with clear spatial separation from the soma and 2 in close proximity to the soma).

FOV fluorescence intensity analysis. We used average intensity projections of 500 frames, acquired six weeks after virus injection, to

measure the signal intensity across the FOV. The intensity as measured at three y coordinates evenly distributed across the FOV using ImageJ and normalized by dividing all values to the single highest pixel value within each measurement set. The data is down sampled from 512 to 330 measurement points, and the average values from the three individual measurements per mouse were used for data presentation.

ROI per field of view analysis. We used average intensity projections of 250 frames, acquired six weeks after virus injection, to measure the number of ROIs per FOV. One single FOV per mouse was used for the analysis, and the segmentation was performed by using CellPose³⁹. The images for the analysis were acquired using identical settings and a FOV size of $840 \times 700 \mu\text{m}$.

Wide-field imaging analysis. To measure changes in fluorescence over time in wide-field imaging videos, we used ImageJ (Fiji). Videos were spatially down-sampled, and regions of interest (ROIs) were selected in the center of the cranial window. Changes in relative fluorescence were calculated by $(F - F_0)/F_0$, where the baseline fluorescence (F_0) was defined as the mean fluorescence across all frames from “spontaneous” and “visual stimulus” runs in the entire cranial window. Calcium signal traces were obtained from the average fluorescence intensity in an $\sim 200 \mu\text{m}$ diameter circular area.

Histology. Six weeks after virus injection, all animals were deeply anesthetized by an intraperitoneal injection of Euthazol (pentobarbital sodium 100 mg/kg, Le Vet) and intracardially perfused with PBS followed by 4% paraformaldehyde in PBS. Brains were dissected out and postfixed for 24 h followed by cryoprotection in 30% sucrose in PBS for 48 h. $40 \mu\text{m}$ coronal sections were cut with a cryostat (Leica). All sections were stained free-floating on constant agitation. The sections were rinsed three times in PBS followed by blocking in 2% bovine serum in 0.3% Triton X-100 in PBS for 1 h before incubation with the primary antibody in blocking solution overnight (all antibodies used are listed in Table 3). After rinsing, sections were incubated with secondary antibodies in PBS for 1 h. Sections were then mounted on Superfrost Plus adhesion slides and dried for 2 h. After rinsing in dH_2O and additional drying for 1 h, sections were coverslipped with mounting medium (Ibidi). Tile scans were acquired with 20% overlap on an Andor Dragonfly spinning-disc microscope with a motorized platform and stitched using Fusion software (Bitplane). The Andor Dragonfly was built on a Nikon TiE inverted microscope equipped with a Nikon PlanApo $\times 10/0.45$ NA objective. High-magnification images were acquired on the same microscope using a Nikon CF Apo $\times 60/1.4$ NA objective.

To estimate the number of activated microglia per area, we used sections stained for Iba1, in addition to the neuronal marker NeuN and GFP (to verify the expression of the GECI). A region containing the

primary visual cortex was selected, and the number of Iba1-positive cells was manually counted using ImageJ.

Reporting summary

Further information on research design is available in the Nature Portfolio Reporting Summary linked to this article.

Data availability

All plasmids used have been uploaded to Addgene, and antibodies used are listed with their corresponding RRID in Table 3. Original raw data from imaging experiments will be available in a public repository with time, and are available upon request to the authors. Source data are provided with this paper.

Code availability

Custom code used for analysis is available at <https://github.com/frederikrogge/calcium-sensor-analysis>.

References

- Inoue, M. et al. Rational engineering of XCaMPs, a multicolor GEC1 suite for in vivo imaging of complex brain circuit dynamics. *Cell* **177**, 1346–1360.e24 (2019).
- Dana, H. et al. High-performance calcium sensors for imaging activity in neuronal populations and microcompartments. *Nat. Methods* **16**, 649–657 (2019).
- Zhang, Y. et al. Fast genetically encoded calcium indicators. **23**, 237–249 (2020).
- Madisen, L. et al. Transgenic mice for intersectional targeting of neural sensors and effectors with high specificity and performance. *Neuron* **85**, 942–958 (2015).
- Daigle, T. L. et al. A suite of transgenic driver and reporter mouse lines with enhanced brain-cell-type targeting and functionality. *Cell* **174**, 465–480 (2018).
- Wekselblatt, J. B., Flister, E. D., Piscopo, D. M. & Niell, C. M. Large-scale imaging of cortical dynamics during sensory perception and behavior. *J. Neurophysiol.* **115**, 2852–2866 (2016).
- Steinmetz, N. A. et al. Aberrant cortical activity in multiple GCaMP6-expressing transgenic mouse lines. *eNeuro* **4**, ENEURO.0207–17.2017 (2017).
- Goldey, G. J. et al. Removable cranial windows for long-term imaging in awake mice. *Nat. Protoc.* **9**, 2515–2538 (2014).
- Kim, J. Y., Grunke, S. D., Levites, Y., Golde, T. E. & Jankowsky, J. L. Intracerebroventricular viral injection of the neonatal mouse brain for persistent and widespread neuronal transduction. *J. Vis. Exp.* (2014) <https://doi.org/10.3791/51863>.
- Yang, Y. et al. Improved calcium sensor GCaMP-X overcomes the calcium channel perturbations induced by the calmodulin in GCaMP. *Nat. Commun.* **9**, 517 (2018).
- Foust, K. D. et al. Intravascular AAV9 preferentially targets neonatal neurons and adult astrocytes. *Nat. Biotechnol.* **27**, 59–65 (2009).
- Lampe, S. E. G., Kaspar, B. K. & Foust, K. D. Intravenous injections in neonatal mice. *J. Vis. Exp.* **11**, 52037, <https://doi.org/10.3791/52037> (2014).
- Hamodi, A. S., Sabino, A. M., Fitzgerald, N. D., Moschou, D. & Crair, M. C. Transverse sinus injections drive robust whole-brain expression of transgenes. *Elife* **9**, e53639 (2020).
- Chan, K. Y. et al. Engineered AAVs for efficient noninvasive gene delivery to the central and peripheral nervous systems. *Nat. Neurosci.* **20**, 1172–1179 (2017).
- Michelson, N. J., Vanni, M. P. & Murphy, T. H. Comparison between transgenic and AAV-PHP.eB-mediated expression of GCaMP6s using in vivo wide-field functional imaging of brain activity. *Neurophotonics* **6**, 1 (2019).
- Yardeni, T., Eckhaus, M., Morris, H. D., Huizing, M. & Hoogstraten-Miller, S. Retro-orbital injections in mice. *Lab Anim.* **40**, 155–160 (2011).
- Chen, Y. et al. Soma-targeted imaging of neural circuits by ribosome tethering. *Neuron* **107**, 454–469.e6 (2020).
- Shemesh, O. A. et al. Precision calcium imaging of dense neural populations via a cell-body-targeted calcium indicator. *Neuron* **107**, 470–486.e11 (2020).
- Hippenmeyer, S. et al. A developmental switch in the response of DRG neurons to ETS transcription factor signaling. *PLoS Biol.* **3**, e159 (2005).
- Broussard, G. J. et al. In vivo measurement of afferent activity with axon-specific calcium imaging. *Nat. Neurosci.* **21**, 1272–1280 (2018).
- Nelson, A. & Mooney, R. The basal forebrain and motor cortex provide convergent yet distinct movement-related inputs to the auditory cortex. *Neuron* **90**, 635–648 (2016).
- Allen, W. E. et al. Global representations of goal-directed behavior in distinct cell types of mouse neocortex. *Neuron* **94**, 891–907.e6 (2017).
- Jackson, K. L., Dayton, R. D., Deverman, B. E. & Klein, R. L. Better targeting, better efficiency for wide-scale neuronal transduction with the synapsin promoter and AAV-PHP.B. *Front. Mol. Neurosci.* **9**, 154 (2016).
- Ji, X. et al. Brain microvasculature has a common topology with local differences in geometry that match metabolic load. *Neuron* **109**, 1168–1187.e13 (2021).
- Kirst, C. et al. Mapping the fine-scale organization and plasticity of the brain vasculature. *Cell* **180**, 780–795.e25 (2020).
- Legaria, A. A. et al. Fiber photometry in striatum reflects primarily nonsomatic changes in calcium. *Nat. Neurosci.* **25**, 1124–1128 (2022).
- Molina, R. S. et al. Understanding the fluorescence change in red genetically encoded calcium ion indicators. *Biophys. J.* **116**, 1873–1886 (2019).
- Wu, J. et al. A long Stokes shift red fluorescent Ca²⁺ indicator protein for two-photon and ratiometric imaging. *Nat. Commun.* **5**, 55 (2014).
- Boyden, E. S., Zhang, F., Bamberg, E., Nagel, G. & Deisseroth, K. Millisecond-timescale, genetically targeted optical control of neural activity. *Nat. Neurosci.* **8**, 1263–1268 (2005).
- Amet, N., Lee, H. F. & Shen, W. C. Insertion of the designed helical linker led to increased expression of Tf-based fusion proteins. *Pharm. Res.* **26**, 523–528 (2009).
- Chen, T. W. et al. Ultrasensitive fluorescent proteins for imaging neuronal activity. *Nature* **499**, 295–300 (2013).
- Krashes, M. J. et al. Rapid, reversible activation of AgRP neurons drives feeding behavior in mice. *J. Clin. Invest.* **121**, 1424–1428 (2011).
- Challis, R. C. et al. Systemic AAV vectors for widespread and targeted gene delivery in rodents. *Nat. Protoc.* **14**, 379–414 (2019).
- Aurnhammer, C. et al. Universal real-time PCR for the detection and quantification of adeno-associated virus serotype 2-derived inverted terminal repeat sequences. *Hum. Gene Ther. Methods* **23**, 18–28 (2012).
- Smith, R. S., Roderick, T. H. & Sundberg, J. P. Microphthalmia and associated abnormalities in inbred black mice. *Lab. Anim. Sci.* **44**, 551–560 (1994).
- Canfield, J. G. Dry beveling micropipettes using a computer hard drive. *J. Neurosci. Methods* **158**, 19–21 (2006).
- Peirce, J. et al. PsychoPy2: experiments in behavior made easy. *Behav. Res. Methods* **51**, 195–203 (2019).
- Pachitariu, M. et al. Suite2p: beyond 10,000 neurons with standard two-photon microscopy. bioRxiv <https://www.biorxiv.org/content/10.1101/061507v2> (2016).

39. Stringer, C., Wang, T., Michaelos, M. & Pachitariu, M. Cellpose: a generalist algorithm for cellular segmentation. *Nat. Methods* **18**, 100–106 (2021).

Acknowledgements

We thank Dr. Ane Charlotte Christensen for assistance with the establishment of the RO injection technique, and for feedback on the manuscript. We also thank the late Paul Johannes Helm for assistance with assembling the two-photon microscope and for many enjoyable discussions about microscopy, physics, and biology. Finally, we thank the Instrumentation Lab at the Department of Bioscience. Imaging of histological sections was performed at the NorMIC microscopy platform at the Department of Bioscience, University of Oslo.

Author contributions

S.G., I.N., G.H.V., K.K.L., and M.F. designed the study. S.G. and G.H.V. performed plasmid design and assembly, and virus production, with assistance from V.B., I.N., and K.K.L. performed surgeries and in vivo imaging. S.G. and I.N. performed immunohistochemistry and post-mortem imaging. F.S.R., S.G., I.N., and K.K.L. analyzed data. S.G., I.N., and K.K.L. wrote the manuscript with inputs from all co-authors. All authors have read the final version of the manuscript.

Competing interests

The authors declare no competing interests.

Additional information

Supplementary information The online version contains supplementary material available at <https://doi.org/10.1038/s41467-023-36324-3>.

Correspondence and requests for materials should be addressed to Kristian Kinden Lensjø.

Peer review information *Nature Communications* thanks the anonymous reviewers for their contribution to the peer review of this work. Peer reviewer reports are available.

Reprints and permissions information is available at <http://www.nature.com/reprints>

Publisher's note Springer Nature remains neutral with regard to jurisdictional claims in published maps and institutional affiliations.

Open Access This article is licensed under a Creative Commons Attribution 4.0 International License, which permits use, sharing, adaptation, distribution and reproduction in any medium or format, as long as you give appropriate credit to the original author(s) and the source, provide a link to the Creative Commons license, and indicate if changes were made. The images or other third party material in this article are included in the article's Creative Commons license, unless indicated otherwise in a credit line to the material. If material is not included in the article's Creative Commons license and your intended use is not permitted by statutory regulation or exceeds the permitted use, you will need to obtain permission directly from the copyright holder. To view a copy of this license, visit <http://creativecommons.org/licenses/by/4.0/>.

© The Author(s) 2023

